8-26-2022

Switched Kinematic and Force Control for Lower-Limb Motorized Exoskeletons and Functional Electrical Stimulation

Chen-Hao Chang
Syracuse University, jtes5313@gmail.com

Abstract

Millions of people experience movement deficits from neurological conditions (NCs) that impair their walking ability and leg function. Exercise-based rehabilitation procedures have shown the potential to facilitate neurological reorganization and functional recovery. Lower-limb powered exoskeletons and motorized ergometers have been combined with functional electrical stimulation (FES) to provide repetitive movement, partially reduce the burden of therapists, improve range of motion, and induce therapeutic benefits. FES evokes artificial muscles contractions and can improve muscle mass and strength, and bone density in people with NCs. Stationary cycling is recommended for individuals who cannot perform load-bearing activities or have increased risks of falling. Cycling has been demonstrated to impart physiological and cardiovascular benefits. Motorized FES-cycling combines an electric motor and electrical stimulation of lower-limb muscles to facilitate coordinated, long-duration exercise, while mitigating the inherent muscle fatigue due to FES. Lower-limb exoskeletons coupled with FES, also called neuroprostheses or hybrid exoskeletons, can facilitate continuous, repetitive motion to improve gait function and build muscle capacity. The human-robot interaction during rehabilitative cycling and walking yield a mix of discrete effects (i.e., foot impact, input switching to engage lower-limb muscles and electric motors, etc.) and continuous nonlinear, uncertain, time-varying dynamics. Switching control is necessary to allocate the control inputs to lower-limb muscle groups and electric motors involved during assisted cycling and walking. Kinematic tracking has been the primary control objective for devices that combine FES and electric motors. However, there are force interactions between the machine and the human during cycling and walking that motivate the design of torque-based controllers (i.e., exploit torque or force feedback) to shape the leg dynamics through controlling joint kinematics and kinetics. Technical challenges exist to develop closed-loop feedback control strategies that integrate kinematic and force feedback in the presence of switching and discontinuous effects. The motivation in this dissertation is to design, analyze and implement switching controllers for assisted cycling and walking leveraging kinematic and force feedback

while guaranteeing the stability of the human-robot closed-loop system.

In Chapter 1, the motivation to design closed-loop controllers for motorized FES-cycling and powered exoskeletons is described. A survey of closed-loop kinematic and force feedback control methods is also introduced related to the tracking objectives presented in the subsequent chapters of the dissertation.

In Chapter 2, the dynamics models for walking and assisted cycling are described. First, a bipedal walking system model with switched dynamics is introduced to control a powered lower-limb exoskeleton. Then, a stationary FES-cycling model with nonlinear dynamics and switched control inputs is introduced based on published literature. The muscle stimulation pattern is defined based on the kinematic effectiveness of the rider, which depends on the crank angle. The experimental setup for lower-limb exoskeleton and FES-cycling are described.

In Chapter 3, a hierarchical control strategy is developed to interface a cable-driven lower-limb exoskeleton. A two-layer control system is developed to adjust cable tensions and apply torque about the knee joint using a pair of electric motors that provide knee flexion and extension. The control design is segregated into a joint-level control loop and a low-level loop using feedback of the angular positions of the electric motors to mitigate cable slacking. A Lyapunov-based stability analysis is developed to ensure exponential tracking for both control objectives. Moreover, an average dwell time analysis computes an upper bound on the number of motor switches to preserve exponential tracking. Preliminary experimental results in an able-bodied individual are depicted. The developed control strategy is extended and applied to the control of both knee and hip joints in Chapter 4 for treadmill walking.

In Chapter 4, a cable-driven lower-limb exoskeleton is integrated with FES for treadmill walking at a constant speed. A nonlinear robust controller is used to activate the quadriceps and hamstrings muscle groups via FES to achieve kinematic tracking about the knee joint. Moreover, electric motors adjust the knee joint stiffness throughout the gait cycle using an integral torque

feedback controller. A Lyapunov-based stability analysis is developed to ensure exponential tracking of the kinematic and torque closed-loop error systems, while guaranteeing that the control input signals remain bounded. The developed controllers were tested in real-time walking experiments on a treadmill in three able-bodied individuals at two gait speeds. The experimental results demonstrate the feasibility of coupling a cable-driven exoskeleton with FES for treadmill walking using a switching-based control strategy and exploiting both kinematic and force feedback.

In Chapter 5, input-output data is exploited using a finite-time algorithm to estimate the target desired torque leveraging an estimate of the active torque produced by muscles via FES. The convergence rate of the finite-time algorithm can be adjusted by tuning selectable parameters. To achieve cadence and torque tracking for FES-cycling, nonlinear robust tracking controllers are designed for muscles and motor. A Lyapunov-based stability analysis is developed to ensure exponential tracking of the closed-loop cadence error system and global uniformly ultimate bounded (GUUB) torque tracking. A discrete-time Lyapunov-based stability analysis leveraging a recent tool for finite-time systems is developed to ensure convergence and guarantee that the finite-time algorithm is Hölder continuous. The developed tracking controllers for the muscles and electric motor and finite-time algorithm to compute the desired torque are implemented in real-time during cycling experiments in seven able-bodied individuals. Multiple cycling trials are implemented with different gain parameters of the finite-time torque algorithm to compare tracking performance for all participants.

Chapter 6 highlights the contributions of the developed control methods and provides recommendations for future research extensions.

SWITCHED KINEMATIC AND FORCE CONTROL FOR LOWER-LIMB MOTORIZED EXOSKELETONS AND FUNCTIONAL ELECTRICAL STIMULATION

by

Chen-Hao Chang

B.S., National Cheng Kung University, 2014

M.S., University of Florida, 2018

Dissertation

Submitted in partial fulfillment of the requirements for the degree of

Doctor of Philosophy in

Mechanical and Aerospace Engineering

Syracuse University

August 2022

Contents

List of Tables

List of Figures

Chapter 1

Introduction

1.1 Background

After a traumatic brain injury, spinal cord injury (SCI), or stroke, people experience movement deficits, cardiovascular diseases, negative psychological effects, and lack of independence. Rehabilitation machines, exoskeletons, and powered orthoses seek to assist or replace limb functions to improve the quality of life of people with neurological conditions. Automatic and semi-automatic machines such as powered exoskeletons and motorized exercise cycles have been combined with functional electrical stimulation (FES) to regain function, provide repetitive training, partially reduce the burden of therapists, improve range of motion, and induce therapeutic and cardiovascular benefits [1], [2]. FES evokes artificial muscle contractions to achieve arm and leg movements. The implementation of FES closed-loop feedback controllers have been demonstrated for upper-limb rehabilitation [3], [4], locomotion [5]–[8], and lower-limb cycling [9]–[13]. Lower-limb rehabilitation machines aim to produce coordinated leg movements by activating multiple lower-limb muscles along with the assistance of electric motors, which naturally prolong the exercise duration by adding an extra control authority (i.e., electric motors aid to de-

lay the onset of muscle fatigue by preventing over-stimulation). Challenges to achieve smooth control via FES include accelerated muscle fatigue and the highly nonlinear muscle activation rate for a given stimulation intensity input [14]. Therefore, motivation exists to develop robust and adaptive human-robot closed-loop controllers that achieve natural and intuitive movement, while providing rigorous proofs of stability of the coupled system.

A hybrid approach integrating robotic exoskeletons and FES provides the benefits of actively stimulating paralyzed muscles and exploits the robot's torque reliability to yield repetitive motion. Hybrid exoskeletons provide postural support, coordinate motion across multiple joints, and apply bursts of electrical stimulation. Hybrid exoskeletons can contribute to delay the onset of muscle fatigue by reducing the muscle stimulation duty cycle and improving endurance. Hybrid exoskeletons have incorporated direct joint actuation and implemented closed-loop controllers for the actuators and FES [15], [16]. Hybrid orthoses have been designed to lock and unlock leg joints as a function of the gait cycle to provide upright stability and leg assistance using postural controllers [7]. A hybrid neuroprosthesis (HNP) evaluated a finite state machine controller to coordinate stimulation and exoskeleton inputs for stepping [17]. A hybrid system integrating an exoskeleton to actuate hip and knee joints, and implanted neural stimulation has been developed to increase gait speed in individuals with SCI [18]. Cooperative control between motor and muscle loops has been developed to minimize the motor torque contribution and maximize the muscle-generated joint torques via surface stimulation [15]. Synergy-based controllers address the problem of actuator redundancy in simulation to control muscles via FES and electric motors [19] and account for the muscle activation dynamics and the inherent electromechanical delay of muscles. Technical innovations are needed to advance the control design and analysis of hybrid exoskeletons to yield more natural and compliant interactions for people with varying levels of volition. These can aid increasing gait speed and endurance since they remain limited with existing hybrid devices [20].

Soft or cable-driven exoskeletons have the potential to be used for function restoration during gait

rehabilitation when coupled with FES. Differently from exoskeletons with direct joint motor actuation, soft exoskeletons use wearable garments and Bowden cables to enable human transparent movements for walking and running [21]–[26]. Cable-driven transmission mechanisms offload actuators away from the human to reduce the weight imposed on the body, and such mechanisms have been implemented for lower-limb [27], [28] and upper-limb [29], [30] assistance. Cable-driven exoskeletons are also practical systems to prototype and test gait control designs with a relatively low complexity and ease of configuration [31]. Lighter exoskeletons can provide less resistance to muscle effort and could potentially reduce the metabolic costs of walking using hybrid exoskeletons compared to more rigid exoskeletons [32]. Soft wearable exoskeletons and ankle emulators have reduced the metabolic energy consumption during walking by optimizing control parameters in able-bodied individuals and stroke survivors [33]–[35]. Soft exoskeletons have implemented a human-in-the-loop paradigm [34], [36] demonstrating improvements in walking speed and distance for post-stroke individuals. Integrating the system-level benefits of cable-driven exoskeletons and muscle-driven benefits of FES can provide customized walking behaviors. However, challenges remain to design and evaluate feasible and intuitive control strategies for cable-driven exoskeletons and FES during assisted walking, while developing rigorous control analysis for the multi-joint hybrid system.

A fundamental research question for the development of hybrid exoskeletons is how to allocate or segregate the control design for the powered actuators and muscles [15], [16], [37]. Kinematic tracking has been the primary control objective for rehabilitation devices and machines that combine FES and powered actuation, where the desired trajectories can be tracked by muscles, electric motors (i.e., the machine or robot) or both during walking and cycling [10], [37], [38]. Recently, torque tracking objectives have been developed for motorized FES-cycling using admittance-based or impedance-based strategies with a Lyapunov-based analysis [39]–[41]. Cable-driven exoskeletons allow for the design of force feedback controllers, by including force transducers, as a strategy to adjust the cable tension and influence joint kinematics and kinetics. In particular, muscular and joint stiffness are essential for leg coordination and regulation of pos-

ture [42], [43]. Stiffness control is motivated for human-machine interaction for its ability to absorb shock, robustness to perturbations, efficiency to release and store energy, and safety [44]–[46]. Stiffness control has been widely used in industrial manufacturing machines, grasping for robotic hands [47], upper-limb exoskeletons [48], ankle actuators [49], and surgical manipulators [50]. Stiffness controllers traditionally have used impedance-based models to generate interaction torques based on changes in the joint kinematics. Gait training was performed using an admittance controller in a robot that converts desired assistance to joint trajectories and stiffness profiles [51]. A hybrid FES-exoskeleton cooperative strategy exploited a torque field with stiffness and damping for the motor control, while kinematic controllers were designed for the muscles [52]. A motivation is to exploit the ability of the cable-driven exoskeleton to adjust the joint stiffness and design FES controllers for muscles during walking.

A distributed approach can be developed to implement kinematic and force controllers during walking experiments using layers. The high-level control layer includes the designed tracking controllers to follow the desired kinematic or force trajectories [53], [54]. The low-layer allocates control among actuators and generates the inputs that are applied to the lower-limb muscles and electric motors that actuate the cables in the powered exoskeleton. A systematic and rigorous low-level control design is needed to adjust the tension in the cable-pulley systems. Since cables cannot transmit compression forces, at least two cables are required to control a 1-DOF joint to provide an agonist-antagonist movement [55] (i.e., bi-directional joint motion). Despite the advantages of cable-driven mechanisms, two major challenges arise to ensure adequate control [56]: (1) cables can experience a slack behavior if the tension is not accurately controlled, thus undesirable backlash occurs in the torque transmission; (2) co-activation of agonist-antagonist cables can lead to lack of coordination due to counteracting torques applied about a joint. Hence, it is essential to develop effective control strategies to ensure coordinated motion and torque transfer in a multi-joint cable-driven system.

Powered cable-driven exoskeletons aim to achieve precise joint tracking by activating a pair of

electric motors to ensure bi-directional motion. This type of bi-directional actuation requires switching between two electric motors to alternate between flexion and extension motions during walking. This kind of input switching is ubiquitous to achieve leg coordination, yet there is a lack of rigorous control design and stability analysis to examine the switching effects in the performance of existing cable-driven powered exoskeletons for walking [28], [31], [53]. However, input switching can destabilize otherwise stable subsystems [57]. Hence, motor input switching poses a challenge to ensure stability of the closed-loop exoskeleton system. Different strategies have been developed to address various kinds of switching effects. A dwell time analysis ensures a switched system achieves exponential stability under slow switching [57]. However, the challenge for the bi-directional joint control using cable-driven systems is that the switching instances are not known a priori (i.e., the timing at which switching occurs is unknown). Thus, a dwell time analysis is likely restrictive and unfeasible to coordinate motor switching. Instead, an average dwell time analysis [57] can be introduced to guarantee the stability of the switching system by developing a condition on the maximum allowable number of switches (i.e., control allocation switching) within a given time interval. To our knowledge, existing cable-driven exoskeletons [27], [28] have not exploited a switched systems approach to design and analyze controllers that activate multiple actuators for walking.

Despite the numerous benefits of gait rehabilitation, FES-cycling is recommended for people with upper-limb pathologies and impaired sensory feedback who are excluded from gait training or other high cardiovascular exercises. In motorized FES-cycling, surface electrical stimulation is applied to multiple muscle groups to evoke active torque complemented by the assistance of an electric motor [9]. Cadence and power tracking are two main control objectives for FES-cycling, which have motivated the design and evaluation of controllers leveraging different techniques. Robust controllers have been designed and implemented to track desired cadence trajectories with and without motorized assistance [9], [58]–[60]. Adaptive-based control methods involving switched dynamics have been recently introduced to compensate for model uncertainties and improve tracking performance using iterative learning [13], repetitive learning [10], and

concurrent learning [61] approaches. Power tracking controllers were designed to track predetermined desired torque trajectories using impedance and admittance techniques [41], [62], [63] and a model-based feedback approach [64]. However, existing power tracking controllers usually implement predetermined desired torque trajectories and thus are prone to experience degraded performance due to the time-varying muscle dynamics and fatigue. Limited torque tracking performance may require manual adjustments of the desired torque demand, which is not practical in clinical settings. Thus, technical challenges remain to develop control methods that can adjust the desired torque trajectory in real-time to improve power tracking, while capturing the muscle force-producing ability and guaranteeing stability.

A potential strategy to improve power tracking in FES-cycling is to adjust the desired torque target based on collected input-output data. For example, powermeters are usually integrated in lower-limb cycles to measure the applied torque about the crank. However, the torque measurements provided by powermeters include the collection of passive and active torque contributions by the rider. Therefore, recent studies on FES-cycling have calculated estimates of the active torque generated by muscles to segregate their torque contributions about the crank [41]. Impedance and admittance controllers for FES-cycling have implemented an indirect torque approach in which changes in the rider's torque influence the cadence trajectory or vice versa (i.e., changes in cadence impact the torque trajectory) [41], [62], [63]. However, it remains unclear how to exploit estimates of the active muscle torque to adjust the desired torque trajectory in real-time independently and without affecting the desired cycle's cadence. In addition, the approach to adjust the torque demand needs to guarantee stability of the closed-loop torque error system and have fast convergence (e.g., finite-time convergence) to capture the rider's time-varying ability to generate active torque, which is influenced by muscle fatigue.

Finite-time stability is a well-studied concept in control systems that guarantees convergence to an equilibrium in finite time and provides robustness with respect to disturbances. Thus, control performance can be improved by leveraging finite-time stability tools to obtain a faster rate

of convergence compared to traditional asymptotic results. Stability results for continuous autonomous systems, non-autonomous (i.e., time-varying systems), switched, and hybrid systems have been reported in [65]–[68]. Finite-time stability results have been extended for adaptive parameter estimation [69], discontinuous (using Filippov solutions) and impulsive systems [70], [71]. A finite-time method has been integrated with extremum seeking to maximize or minimize a cost function and achieve real-time optimization with a fast convergence rate [72], [73]. Recently, a discrete finite-time framework has leveraged input-output data to learn uncertain dynamics and guarantee robustness and nonlinear stability [74]. However, it is an open problem to explore the feasibility of finite-time control tools to improve torque tracking performance and ensure fast convergence in FES-cycling systems.

1.2 Outline of the Dissertation

In Chapter 2, the dynamics models of the robotic lower-limb exoskeleton with FES inputs and the cycle-rider stationary cycling system are introduced. The bipedal walking model for exoskeleton control is developed using a switched systems approach. The cycling model includes the switching effects of activating multiple muscle groups based on a state-dependent stimulation pattern that exploits the kinematic effectiveness of the rider. The experimental setup and procedures are also introduced in Chapter 2.

In Chapter 3, the control design to achieve knee joint extension and flexion using a cable-driven exoskeleton is segregated into two layers. First, the joint layer (high-level) computes the control input needed to track the desired kinematic joint trajectory, which is achieved through a robust sliding-mode controller. Second, the motor layer (low-level) includes a pair of electric motors to provide bi-directional motion about the knee joint. One motor, called the lead motor, implements the control input commanded by the joint layer to achieve the desired joint kinematics. The second motor, called the follower motor, tracks the angle of the lead motor also using a robust

sliding-mode controller. The goal for the follower motor controller is to minimize cable slacking and improve response when switching occurs. To achieve leg extension and flexion, the electric motors switch their roles between lead and follower motor. A Lyapunov-based stability analysis is used to guarantee high-level exponential joint kinematic tracking. For the low-level layer, additional stability analyses guarantee exponential tracking for the flexion and extension motors, when each is activated as the follower motor. Finally, an average dwell time analysis provides a condition on the maximum allowable number of motor switches to preserve exponential convergence when allocating the control between the pair of motors. This low-level control design has been further applied to pairs of electric motors for both knee and hip joints to achieve bi-directional motion in Chapter 4.

In Chapter 4, kinematic and torque tracking controllers are designed to activate the electric motors of a lower-limb cable-driven exoskeleton and muscles via FES to achieve treadmill walking at a constant speed. The hybrid exoskeleton and human are modeled as a four-link bipedal walking system with state-dependent switched dynamics to describe the gait phase transitions from stance phase to swing phase, and vice versa. The leg dynamics is modeled as a switched system to characterize the pendulum dynamics within the swing phase and the inverted pendulum dynamics within the stance phase, and their ongoing transitions during walking. The quadriceps and hamstrings muscle groups are electrically stimulated using a nonlinear robust kinematic feedback controller to guide the knee joints through their desired joint angles, while the electric motors adjust the cable tension to achieve a desired torque using a stable stiffness model. The electric motors provide torque assistance about the hip joints to track the desired hip joint angles. The bipedal walking dynamics include low-level switching to determine the active muscles and electric motors to achieve flexion and extension motion for the knee and hip joints. A Lyapunov-based approach is developed to ensure exponential tracking of the kinematic and torque closed-loop systems.

In Chapter 5, cadence and torque controllers are designed for power tracking using a motor-

ized FES-cycling system. The cycle-rider system is modeled as a nonlinear, time-varying, state-dependent switched dynamical system. To capture the time-varying muscle capacity to evoke active torque, a finite-time torque control algorithm is developed to adjust the desired torque in real-time by leveraging estimates of the active torque produced by muscles. The finite-time torque controller leverages input-output data and is designed in discrete-time to adjust the peak torque demand per crank cycle, and thus converge in finite-time. This torque strategy departs from existing cycling studies that implement predetermined desired torque trajectories that may require manual tuning as the rider fatigues. A robust sliding-mode controller using an integral torque signal is designed to apply FES to the hamstrings, quadriceps, and gluteus muscle groups to track the desired torque trajectory. Similarly, a robust sliding-mode controller is designed for the electric motor to achieve the desired cadence tracking objective. A Lyapunov-based stability analysis is developed to ensure exponential cadence tracking and obtain a global uniformly ultimate bounded (GUUB) result for torque tracking. A discrete-time Lyapunov-based analysis is used to ensure the finite-time torque controller that generates the desired trajectory is Hölder continuous.

Chapter 6 concludes the dissertation. A summary of the dissertation is provided along with a discussion on potential extensions and future research directions based on the results developed in previous chapters.

Chapter 2

Dynamics Models and Experimental Setup

In this chapter, the bipedal walking model used to control the robotic lower-limb exoskeleton with FES is presented using a switched systems approach [62]. The cycle-rider nonlinear dynamics model with switched dynamics is presented [9], [58]. The experimental setup for lower-limb exoskeleton and FES-cycling are described.

2.1 Lower-limb Exoskeleton Dynamics Model

2.1.1 Dynamics Model Derivation

A four-link bipedal walking system is derived in this section as illustrated in Figure 2.1. The following assumptions are used in the derivation.

Assumption 1. *The walking system is restricted to movement in the sagittal plane.*

Assumption 2. *The model of the foot is neglected (i.e., point-foot contact with the ground is assumed), and the ground contact is assumed to be rigid.*

Assumption 3. *There is no slipping between the point-foot and the ground.*

Assumption 4. *The trunk dynamics is neglected and assumed to be rigid in the vertical direction. A safety harness connected to an overhead support system is used to stabilize the trunk.*

Assumption 5. *The impact dynamics model and double-support phase are not considered for treadmill walking. The double-support phase occurs instantaneously and the standing leg switches from one side to the other.*

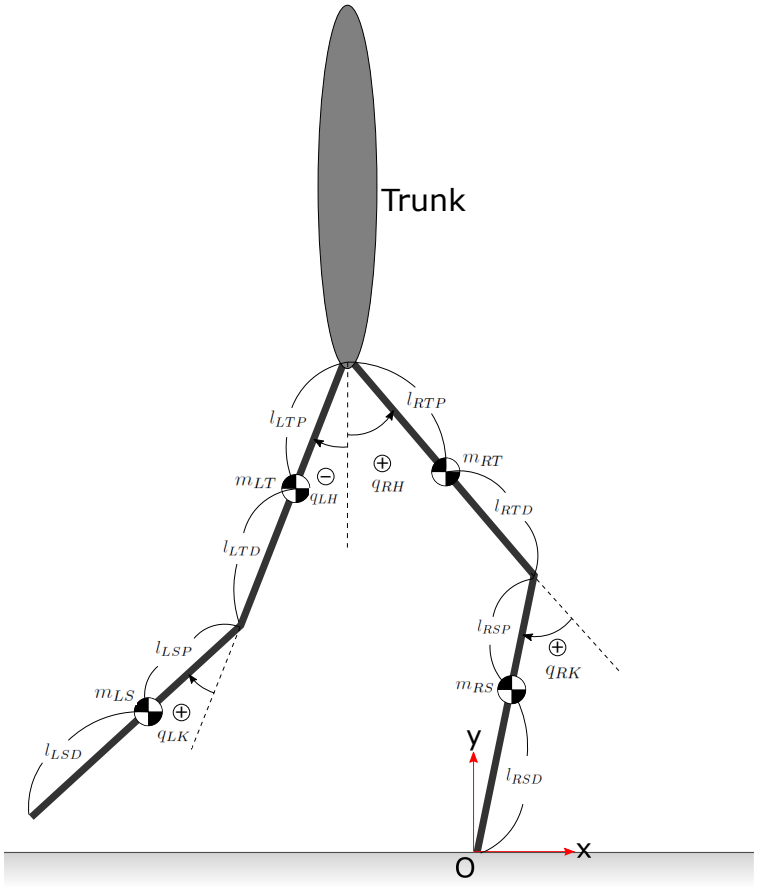

Figure 2.1: The figure represents the case when the standing leg is the right leg. Inertial frame is attached to the point-foot. The trunk dynamics are neglected and the trunk is assumed to be in a vertical position due to the safety harness and overhead support. The joint angles are denoted by $q_{RK}, q_{LK}, q_{RH}, q_{LH}$ (i.e., right (R), left (L), knee joint (K), and hip joint (H), respectively). The CoM for each link is denoted as $m_{RS}, m_{LS}, m_{RT}, m_{LT}$, where the subscripts S, T represent shank and thigh. The unknown link lengths to the CoM are denoted by $l_{RSP}, l_{RSD}, l_{LSP}, l_{LSD}, l_{RTP}, l_{RTD}, l_{LTP}, l_{LTD}$, where the subscripts P, D represent proximal (toward body core) and distal (out of body core) direction.

The inertial frame is attached to the point-foot that is in contact with the ground. Each link can

be treated as a point-mass. The unknown distance between each link's end to its center of mass (CoM), and unknown point-mass are illustrated in Figure 2.1. The measurable joint angles and angular velocities are also illustrated in Figure 2.1. Following standard Lagrangian mechanics, the Lagrangian can be defined as

$$L(q, \dot{q}) = K(q, \dot{q}) - V(q), \tag{2.1}$$

where $q : \mathbb{R}_{\geq t_0} \to \mathbb{R}^4$ denotes joint angles, $\dot{q} : \mathbb{R}_{\geq t_0} \to \mathbb{R}^4$ denotes the joint angular velocities, K denotes the kinematic energy, and V denotes the potential energy. The dynamic equation of the walking exoskeleton system can be calculated as

$$\frac{d}{dt}\frac{\partial L}{\partial \dot{q}} - \frac{\partial L}{\partial q} = \tau, \tag{2.2}$$

where τ represents the actuator torques.

2.1.2 Exoskeleton Dynamics Model

The hybrid exoskeleton and a human can be modeled as a four-link bipedal walking system in the sagittal plane with a switching Euler-Lagrange model as [62]

$$M_\rho(q)\ddot{q} + C_\rho(q, \dot{q})\dot{q} + G_\rho(q) + P_\rho(q, \dot{q}) + d_\rho(t) = \tau_{\mathcal{E}}(q, \dot{q}, t) + \tau_{\mathcal{M}}(q, \dot{q}, t), \tag{2.3}$$

where the subscript $\rho \in \mathcal{R} \triangleq \{1, 2\}$ denotes the index of the switching dynamics using the stance leg as the reference, such that $\rho = 1$ denotes the right leg as the stance leg and $\rho = 2$ denotes the left leg as the stance leg, as illustrated in Figure 2.2. The joint angle vector is defined as $q \triangleq [q_{rk}, q_{lk}, q_{rh}, q_{lh}]^T : \mathbb{R}_{\geq t_0} \to \mathbb{R}^4$ denoting the measurable joint angles (i.e., right (r), left (l), knee joint (k), and hip joint (h), respectively), $\dot{q} : \mathbb{R}_{\geq t_0} \to \mathbb{R}^4$ and $\ddot{q} : \mathbb{R}_{\geq t_0} \to \mathbb{R}^4$ denote the measurable joint angular velocities and unmeasurable joint angular accelerations, respectively,

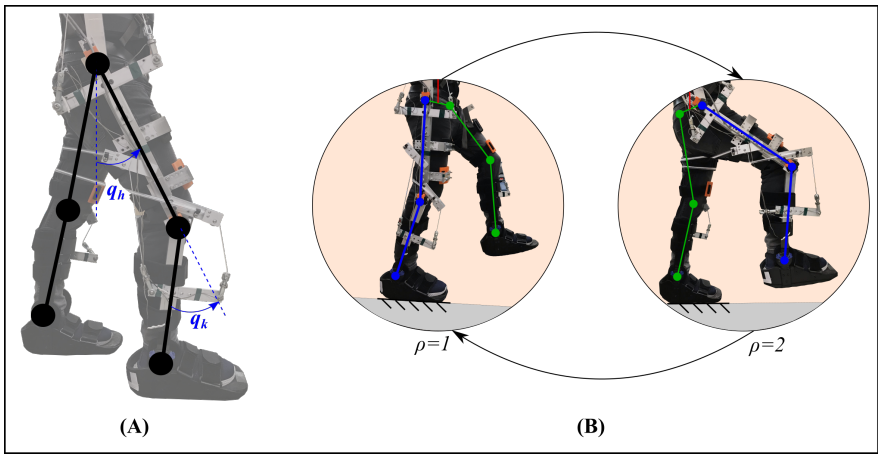

Figure 2.2: Schematic of the human-exoskeleton system with switching dynamics. **(A)** The knee joint angle q_k and hip joint angle q_h of the right leg are depicted in an initial standing position. **(B)** The switching dynamics are illustrated using the stance leg as reference (i.e., support leg). The subsystem $\rho = 1$ denotes when the right leg is in the stance phase and the left leg is in the swing phase. The subsystem $\rho = 2$ denotes when the left leg is in the stance phase and the right leg is the swing phase.

and $t_0 \in \mathbb{R}_{\geq 0}$ is the initial time; $M_\rho : \mathbb{R}^4 \to \mathbb{R}^{4\times 4}_{>0}$ denotes the combined human-exoskeleton inertia; $C_\rho : \mathbb{R}^4 \times \mathbb{R}^4 \to \mathbb{R}^{4\times 4}$ and $G_\rho : \mathbb{R}^4 \to \mathbb{R}^4$ denote the Centripetal-Coriolis and gravitational effects, respectively; $P_\rho : \mathbb{R}^4 \times \mathbb{R}^4 \to \mathbb{R}^4$ denotes the damping and viscoelastic effects; and $d_\rho : \mathbb{R}_{\geq t_0} \to \mathbb{R}^4$ denotes lumped disturbances applied to the system by the legs (e.g., involuntary forces and muscle spastic contractions), ground reaction effects, and any other unmodeled effects present in the system.

The torque inputs in (2.3) include $\tau_{\mathcal{E}} : \mathbb{R}^4 \times \mathbb{R}^4 \times \mathbb{R}_{\geq t_0} \to \mathbb{R}^4$, which denotes the torque applied by electric motors, and $\tau_{\mathcal{M}} : \mathbb{R}^4 \times \mathbb{R}^4 \times \mathbb{R}_{\geq t_0} \to \mathbb{R}^4$, which denotes the active torque produced by active muscle contractions via FES. Hence, the hybrid exoskeleton integrates electric motors and FES applied on the muscles to actuate the hip and knee joints as illustrated in Figure 2.3. The cable-driven mechanism provides tension to flexor (fl) and extensor (ex) cables using electric motors. Similarly, FES is applied to the hamstrings (ham) and quadriceps (quad) muscle groups to achieve knee flexion and extension, respectively. Electric motors provide torque about both knee and hip joints (Figure 2.3.A). FES evokes muscle contractions to generate torque about the knee joint since the quadriceps and hamstrings are assumed to produce torque only about the

knee joint (i.e., negligible hip coactivation). (Figure 2.3.B). The activation of hip flexors and extensors is challenging using surface FES [16], hence these muscles are not stimulated and do not contribute to generate torque about the hip joint.

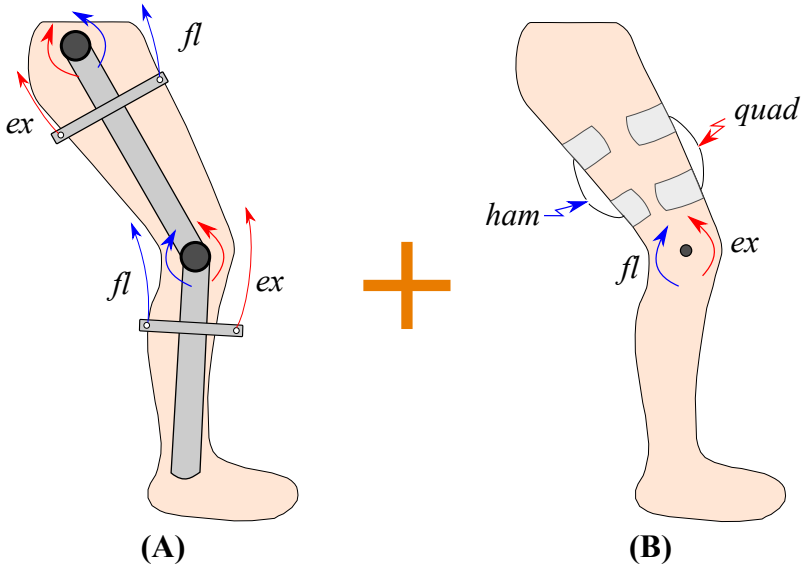

Figure 2.3: Schematic of the hybrid exoskeleton actuation for walking. **(A)** The actuation of the cable-driven exoskeleton is illustrated, where a couple of flexor and extensor cables on each joint are tensioned to provide torque about the joints. **(B)** The FES applied to the quadriceps (quad) and hamstrings (ham) muscle groups to generate torque about the knee joint is depicted.

Assumption 6. *Muscles that span multiple joints such as the quadriceps and hamstrings muscle groups produce torque about the knee joint (negligible hip coactivation). Hence, the muscle biarticular effects [75] are neglected.*

The torque produced by motors and muscles can be defined as

$$\tau_{\mathcal{E}}(q,\dot{q},t) \triangleq \sum_{e=1}^{8} B_e(q,\dot{q})\sigma_e(t)u_e(t), \tag{2.4}$$

$$\tau_{\mathcal{M}}(q,\dot{q},t) \triangleq \sum_{m=1}^{4} B_m(q,\dot{q},t)\sigma_m(t)u_m(t), \tag{2.5}$$

where the subscript $e \in \mathcal{E} = \{1,2,...,8\}$ denotes the motor index, and $m \in \mathcal{M} = \{1,2,3,4\}$ denotes the muscle group index as illustrated in Table 2.1. The unknown individual motor control

effectiveness is denoted as $B_e : \mathbb{R}^4 \times \mathbb{R}^4 \to \mathbb{R}^{4\times4}_{>0}$, and the individual motor current inputs are denoted as $u_e : \mathbb{R}_{\geq t_0} \to \mathbb{R}^4$, $\forall e \in \mathcal{E}$. The unknown individual muscle control effectiveness is denoted by $B_m : \mathbb{R}^4 \times \mathbb{R}^4 \times \mathbb{R}_{\geq t_0} \to \mathbb{R}^{4\times4}_{>0}$ and the individual muscle stimulation inputs are denoted by $u_m : \mathbb{R}_{\geq t_0} \to \mathbb{R}^4$, $\forall m \in \mathcal{M}$. The switching signals are defined as the piecewise constant functions $\sigma_e \in \{0, 1\}$ and $\sigma_m \in \{0, 1\}, \forall e \in \mathcal{E}, m \in \mathcal{M}$.

Table 2.1: Flexion and extension motor indices for right and left hip and knee joints (top). Quadriceps and hamstrings muscles indices for right and left leg (bottom).

	Right Knee	Left Knee	Right Hip	Left Hip
Extension Motor	1	3	6	8
Flexion Motor	2	4	5	7

	Right Leg	Left Leg
Quadriceps	1	3
Hamstrings	2	4

The following properties are exploited in Chapter 3 and Chapter 4.

Property 1. *The inertia matrix $M_\rho(q)$ is positive definite and symmetric, and satisfies the inequalities $c_m \|\xi\|^2 \leq \xi^T M_\rho(q)\xi \leq c_M \|\xi\|^2$, $\forall \xi \in \mathbb{R}^4$, where c_m and c_M are known positive constants, $\forall \rho \in \mathcal{R}$ [76].*

Property 2. *The inverse of the inertia matrix $M_\rho(q)$ is bounded as $\frac{1}{c_M} I \leq M_\rho^{-1}(q) \leq \frac{1}{c_m} I$, $\forall \rho \in \mathcal{R}$, where I is the identity matrix [76].*

Property 3. *$\|C_\rho(q, \dot{q})\| \leq c_c \|\dot{q}\|$, $\forall \rho \in \mathcal{R}$, where c_c is a known positive constant [76].*

Property 4. *$\|G_\rho(q)\| \leq c_g$, $\forall \rho \in \mathcal{R}$, where c_g is a known positive constant [76].*

Property 5. *$\|P_\rho(q, \dot{q})\| \leq c_{p1} + c_{p2} \|\dot{q}\|$, $\forall \rho \in \mathcal{R}$, where c_{p1} and c_{p2} are known positive constants [77]–[79].*

Property 6. *The skew-symmetry $\frac{1}{2}\dot{M} - C = 0$ [76].*

Property 7. *$\underline{B}_e \|\xi\|^2 \leq \xi^T B_e \xi \leq \overline{B}_e \|\xi\|^2$, $\forall \xi \in \mathbb{R}^4$, where $\underline{B}_e$ and $\overline{B}_e$ are known positive constants.*

Property 8. $\underline{B}_m \|\xi\|^2 \leq \xi^T B_m \xi \leq \overline{B}_m \|\xi\|^2$, $\forall \xi \in \mathbb{R}^4$, *where* $\underline{B}_m$ *and* $\overline{B}_m$ *are known positive constants.*

Assumption 7. $\|d_\rho(t)\| \leq c_d$, $\forall \rho \in \mathcal{R}$, *where* c_d *is a known positive constant.*

2.2 Cycle-Rider Dynamics Model with Input Switching

The single degree-of-freedom stationary cycle-rider system is modeled with the following dynamics [58]

$$M(q)\ddot{q} + C(q,\dot{q})\dot{q} + G(q) + P(q,\dot{q}) + d(t) = \tau_e(q,\dot{q},t) + \tau_m(q,\dot{q},t), \tag{2.6}$$

where $q : \mathbb{R}_{\geq t_0} \to \mathcal{Q}, \dot{q} : \mathbb{R}_{\geq t_0} \to \mathbb{R}$, and $\ddot{q} : \mathbb{R}_{\geq t_0} \to \mathbb{R}$ are the measurable crank angle, measurable crank angular velocity, and unmeasurable angular acceleration, $\mathcal{Q} \subseteq \mathbb{R}$ denotes the set of crank angles, and $t_0 \in \mathbb{R}_{\geq 0}$ is the initial time; $M : \mathcal{Q} \to \mathbb{R}_{>0}$ denotes the combined cycle-rider inertia; $C : \mathcal{Q} \times \mathbb{R} \to \mathbb{R}$ and $G : \mathcal{Q} \to \mathbb{R}$ denote the Centripetal-Coriolis and gravitational effects, respectively; $P : \mathcal{Q} \times \mathbb{R} \to \mathbb{R}$ denotes the effect of passive viscoelastic and damping forces in the rider's joints; and $d : \mathbb{R}_{\geq t_0} \to \mathbb{R}$ denote the lumped disturbances applied to the system and any other unmodeled effects. The torque applied by the electric motor and produced by FES-induced muscle contractions are denoted by $\tau_e : \mathcal{Q} \times \mathbb{R} \times \mathbb{R}_{\geq t_0} \to \mathbb{R}$ and $\tau_m : \mathcal{Q} \times \mathbb{R} \times \mathbb{R}_{\geq t_0} \to \mathbb{R}$, respectively. FES is applied to the quadriceps, hamstrings and gluteal muscle groups in a pattern that facilitates effective torque transmission about the crank [80]. The torque produced by muscles and the lumped switched muscle control effectiveness are defined as

$$\tau_m(q,\dot{q},t) \triangleq B_\sigma(q,\dot{q},t) u_m(q,\dot{q},t), \tag{2.7}$$

$$B_\sigma(q,\dot{q},t) \triangleq \sum_{m \in \mathcal{M}} B_m(q,\dot{q},t)\sigma_m(q), \tag{2.8}$$

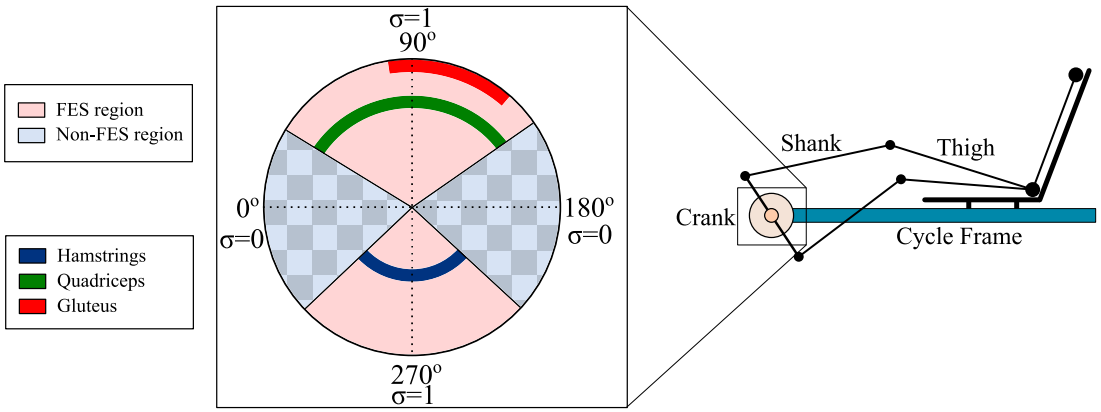

Figure 2.4: Schematic of the muscle stimulation patterns based on the crank angle to yield forward pedaling. The custom stimulation regions for each muscle group are calculated based on the effectiveness to transfer torque about the crank as in [9]. The crank cycle is segregated into FES and non-FES regions. Within the FES regions, muscles are stimulated to achieve the desired torque tracking objective. Within the non-FES regions, FES is not applied due to the low effectiveness to produce active torque. The electric motor is activated during the entire crank cycle to achieve the cadence tracking objective.

respectively, where the FES control input each muscle is denoted by $u_m : \mathcal{Q}\times\mathbb{R}\times\mathbb{R}_{\geq t_0} \to \mathbb{R}$. The subscript $\sigma \in \mathcal{S}$, where $\mathcal{S}$ is a finite set, indicates the index of B_σ and switches according to the crank angle. The individual muscle control effectiveness $B_m : \mathcal{Q} \times \mathbb{R} \times \mathbb{R}_{\geq t_0} \to \mathbb{R}_{>0}$ is defined as in [58], $\forall m \in \mathcal{M}$, where the set $\mathcal{M}$ includes all the stimulated muscle groups. The state-dependent switching signal for each muscle group is denoted as $\sigma_m : \mathcal{Q} \to \{0, 1\}, \forall m \in \mathcal{M}$. Figure 2.4 illustrates an example of the muscle stimulation patterns based on the crank angle.

Cycles are outfitted with powermeters that measure the net torque contributions about the crank. Hence, direct measurements of the active torque contributions by muscles are not readily available. Thus, an estimate of the active torque produced by muscles is obtained similarly to [41] for the subsequent control design. The measurable torque $\tau : \mathbb{R}_{\geq t_0} \to \mathbb{R}$ obtained from the powermeter contains active torque and passive torque from the cycling system. Therefore, the estimation of the active torque $\hat{\tau}_m : \mathcal{Q} \times \mathbb{R} \times \mathbb{R}_{\geq t_0} \to \mathbb{R}$ is defined as follows

$$\hat{\tau}_m(q, \dot{q}, t) = \tau(t) - \tau_{passive}(q, \dot{q}), \tag{2.9}$$

where $\tau_{passive} : \mathcal{Q} \times \mathbb{R} \rightarrow \mathbb{R}$ is the baseline measurement of the passive torque (i.e., the torque required to drive the cycle-rider system without applying FES) recorded in a pretrial cycling test at a constant cadence. The active torque τ_m in (2.7) is defined as

$$\tau_m(q, \dot{q}, t) = \hat{\tau}_m(q, \dot{q}, t) + \epsilon(t), \tag{2.10}$$

where $\epsilon \in \mathbb{R}_{>0}$ is an upper bound of the active torque estimation error.

The torque applied by the electric motor about the crank is defined as

$$\tau_e(q, \dot{q}, t) \triangleq B_e u_e(q, \dot{q}, t), \tag{2.11}$$

where $B_e \in \mathbb{R}_{>0}$ is the control effectiveness of the motor, and $u_e : \mathcal{Q} \times \mathbb{R} \times \mathbb{R}_{\geq t_0} \rightarrow \mathbb{R}$ is the control input for the motor.

The following properties are exploited in Chapter 5.

Property 9. *The inertia matrix $M(q)$ is positive definite and symmetric, and satisfies the inequalities $c_m \leq M(q) \leq c_M$, where c_m and c_M are known positive constants [76].*

Property 10. $|C(q, \dot{q})| \leq c_c|\dot{q}|$, *where c_c is a known positive constant [76].*

Property 11. $|G(q)| \leq c_g$, *where c_g is a known positive constant [76].*

Property 12. $|P(q, \dot{q})| \leq c_{p1} + c_{p2}|\dot{q}|$, *where c_{p1} and c_{p2} are known positive constants [9], [77]–[79].*

Property 13. *The skew-symmetry $\frac{1}{2}\dot{M} - C = 0$ [76].*

Property 14. *The lumped muscle switching control effectiveness is bounded as $\underline{B}_m \leq B_\sigma \leq \overline{B}_m, \forall \sigma \in \mathcal{S}$, where $\underline{B}_m$ and $\overline{B}_m$ are known positive constants [9].*

Property 15. *The control effectiveness of motor is bounded as $\underline{B}_e \leq B_e \leq \overline{B}_e, \forall \sigma \in \mathcal{S}$, where $\underline{B}_e$ and $\overline{B}_e$ are known positive constants [9].*

Assumption 8. $|d(t)| \leq c_d$, *where* c_d *is a known positive constant.*

2.3 Experimental Setup

2.3.1 Lower-limb Exoskeleton Testbed

Treadmill walking experiments are provided to demonstrate the performance of the designed controllers in Chapter 3 and Chapter 4. The control inputs are commanded as stimulation intensities (i.e., pulse width control) to activate the quadriceps and hamstrings muscle groups and as currents to the electric motors that actuate the powered cable-driven exoskeleton.

Testing were performed using a customized exoskeleton designed for fitting different body sizes and maintaining alignment with the user's joints. Figure 2.5 illustrates the exoskeleton testbed. The actuator unit includes brushless 24 VDC electric motors (Maxon) to adjust the torque applied by the cable-driven mechanisms. Optical encoders (US Digital) were mounted at each joint to measure the joint angle and load-cells (OMEGA) were installed in series with the cables to measure cable tension. The controllers were implemented on a desktop computer (Windows 10 OS) running a real-time target (QUARC 2.6, Quanser) via MATLAB/Simulink 2018a (MathWorks Inc) with a sample rate of 1 kHz. The Quanser QPIDe DAQ board was used to read the encoders and cable tensions, and control the servo motor drivers (Maxon) operating in current-controlled mode. The Quanser Q8 USB board was used to read the encoders mounted on motors. A current-controlled stimulator (RehaStim, Hasomed GmbH) delivered biphasic, symmetric, rectangular pulses to the participant's quadriceps and hamstring muscle groups. Self-adhesive PALS® electrodes (3" by 5")[1] were placed on each muscle group in both legs. The stimulation current amplitude and stimulation frequency were fixed at 80 mA and 60 Hz, respectively. A treadmill (Nordic Track) equipped with an encoder (US Digital) to measure the belt's angular displacement was

[1] Surface electrodes for the study were provided compliments of Axelgaard Manufacturing Co., Ltd.

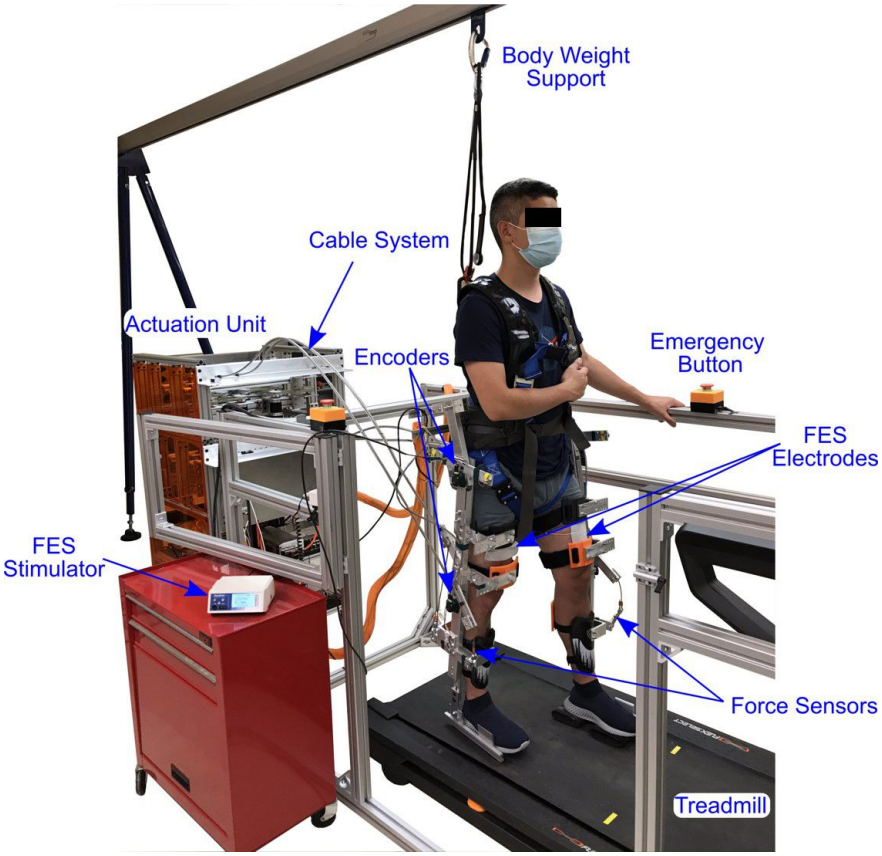

Figure 2.5: The exoskeleton testbed used for treadmill walking. The exoskeleton uses cables to apply torque at each joint using electrical motors installed in the actuation unit. Surface FES is applied on the quadriceps and hamstrings muscle groups. Additional components of the walking system are labeled in the image.

used for walking at constant speeds. The speed of the treadmill was closed-loop controlled using a sliding-mode controller and implemented in a motor driver in current-control mode (Advanced Motion Controls)[2]. As safety measures, the participant had access to an emergency stop button and software stop conditions were implemented to limit the amount of motor currents to comply with the hardware limits and prevent large current transients from being applied to the participant, and muscle stimulation intensities to prevent uncomfortable stimulation intensities. Mechanical stops were designed to avoid moving the legs through unsafe joint angles, and the participants wear a safety harness connected to a portable track system to prevent falling.

[2]The servo drive was provided in part by the sponsorship of Advanced Motion Controls.

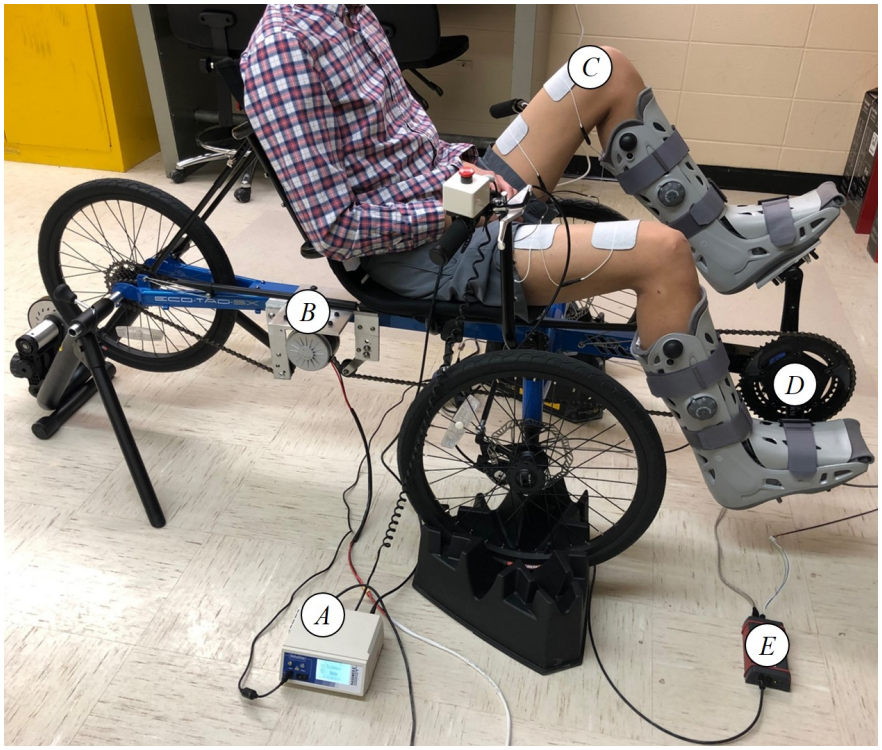

Figure 2.6: Motorized FES-cycling testbed. A) Current-controlled muscle stimulator. B) Brushed DC motor. C) Surface Electrodes. D) Power meter and encoder. E) Torque Analysis Box.

2.3.2 FES-Cycling Testbed

Cycling experiments are provided to demonstrate the performance of the designed power tracking controllers in Chapter 5. The control inputs are commanded as stimulation intensities (i.e., pulse width control) to activate the quadriceps, gluteus, and hamstrings muscle groups and as currents to the electric motor.

Testing was performed using a recumbent cycle (Sun Seeker ECO-TAD SX) mounted on an indoor trainer and adapted with orthotic boots as shown in Figure 2.6. A brushed 24 VDC electric motor was mounted to drive the chain. An optical encoder (H1, US Digital) was mounted at the crank to measure the crank position and a SRM Science Road Wireless Power Meter with a custom Torque Analysis Box measured and broadcasted the torque data. An arduino Mega is used to convert the torque measurements sent by the Torque Analysis Box to a digital signal that can be used as feedback for the torque controller. The controllers were implemented on a

desktop computer (Windows 10 OS) running a real-time target (QUARC 2.6, Quanser) via MATLAB/Simulink 2018a (MathWorks Inc) with a sample rate of 1 kHz. The Quanser QPIDe DAQ board was used to read the encoder signal and the digital torque signal from the Arduino, and to control the motor driver (Advanced Motion Controls)[3] operating in current-controlled mode. A current-controlled stimulator (RehaStim, Hasomed GmbH) delivered biphasic, symmetric, rectangular pulses to the participant's quadriceps, gluteus, and hamstrings muscle groups. Self-adhesive PALS® electrodes (3" by 5")[4] were placed on each muscle group in both legs. The stimulation current amplitude and stimulation frequency were fixed at 80 mA and 60 Hz, respectively, for all muscles. As safety measures, the participant had access to an emergency stop button and software stop conditions were implemented to limit the amount of motor currents to comply with the hardware limits, and muscle stimulation intensities to prevent uncomfortable stimulation intensities.

[3]The servo drive was provided in part by the sponsorship of Advanced Motion Controls.

[4]Surface electrodes for the study were provided compliments of Axelgaard Manufacturing Co., Ltd.

Chapter 3

A Switched Systems Approach for Closed-loop Control of a Lower-Limb Cable-Driven Exoskeleton

In this chapter and in the work in [81], a two-layer control system is developed to adjust cable tensions and apply torque about the knee joint using a cable-driven exoskeleton using a pair of electric motors. The joint layer (high-level) computes the control input needed to track the desired kinematic joint trajectory. The motor layer (low-level) includes a pair of electric motors to provide bi-directional motion about the knee joint. One motor, called the lead motor, implements the control input commanded by the joint layer to achieve the desired joint kinematics. The second motor, called the follower motor, tracks the angle of the lead motor to mitigate slackness when switching direction. Thus, the follower motor aims to minimize cable slacking and improve response when switching occurs. The electric motors switch their roles between lead and follow motor to achieve leg extension and flexion. Robust sliding-mode controllers are designed to track the desired knee joint kinematic trajectory and desired kinematic trajectories for the electric motors. Lyapunov-based stability analysis is developed to ensure exponential tracking for

both control objectives (i.e., high-level and low-level control), and an average dwell time analysis computes an upper bound on the number of motor switches to preserve exponential tracking. An experimental result with an able-bodied individual is presented to illustrate the tracking performance and the switching effects.

3.1 Cable-driven Actuator System

The lower-limb exoskeleton provides torque about the knee joint and is actuated by electric motors using customized cable-driven mechanisms (i.e., forces are transmitted via Bowden cables). A pair of electric motors achieves knee joint extension (ex) and flexion (fl). The two motors are assigned the following roles:

1. The first motor is called the *lead* motor, which controls the knee joint kinematics to achieve the desired motion (i.e., flexion or extension).

2. The second motor is called the *follower* motor, which follows the lead motor's angle to mitigate cable slackness and prevent undesired counteracting forces with the lead motor.

3.1.1 Human-Exoskeleton Dynamics Model

The single DoF knee-joint dynamics with exoskeleton control input (i.e., a reduced model from (2.3) without FES inputs) is defined as

$$M(q)\ddot{q} + C(q,\dot{q})\dot{q} + G(q) + P(q,\dot{q}) + d(t) = \tau_e(q,\dot{q},t), \tag{3.1}$$

where $M(q), C(q,\dot{q}), G(q), P(q,\dot{q}), d(t) \in \mathbb{R}$ are defined in Section 2. In this chapter, the dynamics model in 3.1 includes the inertial, centripetal-Coriolis, gravitational, damping and viscoelastic

effects, and disturbances corresponding to the knee-joint shank dynamics. The torque produced by the electric motors about the knee joint is denoted as $\tau_e \in \mathbb{R}$ and the lumped, switched control effectiveness are denoted by $B_\sigma : \mathbb{R} \times \mathbb{R} \to \mathbb{R}$, and are defined as

$$\tau_e(q, \dot{q}, t) \triangleq B_\sigma(q, \dot{q})u(t), \tag{3.2}$$

$$B_\sigma(q, \dot{q}) \triangleq \sum_{n \in \mathcal{N}} B_n \sigma_n(t), \tag{3.3}$$

where $u : \mathbb{R}_{t_{\geq 0}} \to \mathbb{R}$ is the high-level knee joint kinematic tracking controller (also called knee joint controller), the subscript $n \in \{ex, fl\}$ denotes the motor index, and $\mathcal{N}$ is the motor set. The unknown individual motor control effectiveness is denoted as $B_n \in \mathbb{R}_{>0}, \forall n \in \mathcal{N}$. The subscript $\sigma \in \mathcal{S}$, such that $\mathcal{S}$ is a finite set, indicates the index of B_σ, which includes the possible motor combinations. A piecewise constant switching signal for each motor $\sigma_n \in \{0, 1\}, \forall n$ is defined as

$$\sigma_{ex}(u) \triangleq \begin{cases} 0 & \text{if sgn}(u) \geq 0 \\ 1 & \text{if sgn}(u) < 0 \end{cases}, \tag{3.4}$$

$$\sigma_{fl}(u) \triangleq \begin{cases} 1 & \text{if sgn}(u) > 0 \\ 0 & \text{if sgn}(u) \leq 0 \end{cases}, \tag{3.5}$$

where $\text{sgn}(\cdot) : \mathbb{R} \to \{-1, 0, 1\}$ is the signum function. The switching signals depend on the knee joint control input u, where a positive and negative sign refers to knee flexion and extension, respectively. Therefore, the switching signals in (3.4) and (3.5) achieve the following: when $\sigma_n = 1$, for $n = \{ex\}$, the extension motor becomes the lead motor and receives the magnitude of the knee joint control input u. Concurrently, $\sigma_n = 0$, for $n = \{fl\}$, the flexion motor becomes the follower motor and receives the low-level follower control input (called follower controller) $u_n : \mathbb{R}_{\geq t_0} \to \mathbb{R}$, for $n = \{fl\}$. Alternatively, when $\sigma_n = 0$, for $n = \{ex\}$, the extension motor becomes the follower motor and receives the follower control input $u_n : \mathbb{R}_{\geq t_0} \to \mathbb{R}$, for $n = \{ex\}$. Meanwhile, $\sigma_n = 1$, for $n = \{fl\}$, the flexion motor becomes the lead motor and receives the

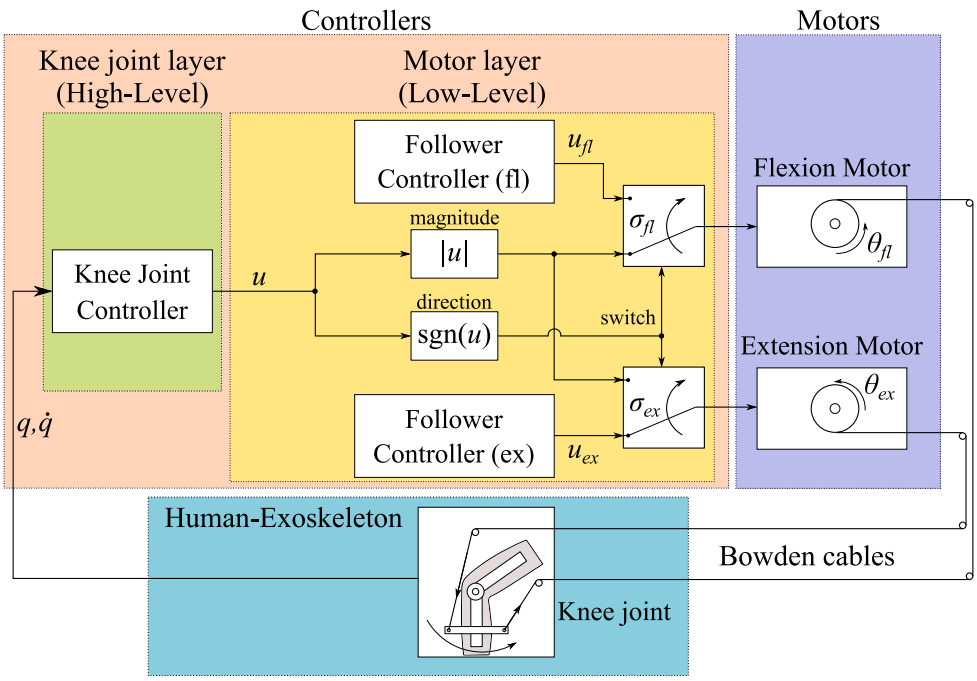

Figure 3.1: Schematic to depict the two-layer control system illustrated for knee flexion. The high-level knee joint controller sends a flexion control input ($u > 0$) to the motor layer. The switching signal is triggered as $\sigma_{fl} = 1$ to pass the magnitude of the knee control input ($|u|$) to the flexion motor. The extension motor becomes the follower motor ($\sigma_{ex} = 0$) and is tasked to follow the angle of the flexion motor (lead motor) using the low-level follower controller (u_{ex}). For knee extension, the high-level knee joint controller computes the extension input ($u < 0$); thus, the extension motor becomes the lead motor and the flexion motor becomes the follower motor.

magnitude of the knee joint control input u. A schematic of the two-layer control system is presented in Figure 3.1, where the knee joint control input is denoted by u, and the follower control inputs for the extension and flexion motors are denoted by u_{ex}, u_{fl}, respectively. Moreover, based on the switching signals in (3.4) and (3.5), the following property is established and exploited in the subsequent control design and stability analysis.

Remark 1. A mapping between the knee joint angle and each motor angular position is needed. This mapping is feasible since there exists a relationship between the measurable knee joint angle q and the flexion and extension motor angular positions denoted by $\theta_{fl}, \theta_{ex} \in \mathbb{R}$, respectively. Given that the cable-driven mechanisms provide sufficient tension, the joint angle q and the angular position of each motor $\theta_n : \mathbb{R}_{\geq t_0} \to \mathbb{R}$, for $n \in \{ex, fl\}$ are coupled and dependent.

The knee joint angle q is a strictly increasing function of the extension and flexion motor angles θ_{ex}, θ_{fl}, respectively (i.e., the relationships between θ_{ex}, θ_{fl} and q are bijective). Hence, the function $\phi_n(\theta_n) = q$, for $n \in \{ex, fl\}$ is analytic and its inverse exists globally. Experimental data illustrating this function and its best linear fit are shown in Figure 3.2.

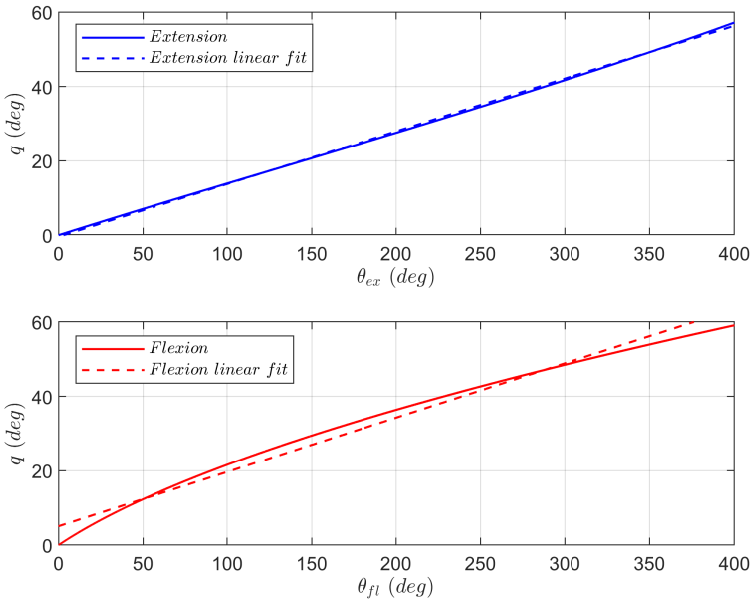

Figure 3.2: Experimental data depicting the knee joint angle q with respect to the motor angles θ_n, for $n \in \{ex, fl\}$ of the extension motor (solid blue line) and flexion motor (solid red line). The dashed lines are the linear fit for the extension (blue) and flexion (red) motors with goodness of fit $R^2 = 0.9969$ and $R^2 = 0.9809$, respectively.

Hence, the linear function $\phi_n : \mathbb{R} \to \mathbb{R}$ is defined as

$$\phi_n(\theta_n) = v_n\theta_n + w_n = q, \forall n \in \mathcal{N}, \tag{3.6}$$

where $v_n, w_n \in \mathbb{R}$ are known constants.

3.1.2 Electric Follower Motor Dynamics Model

The flexion and extension motor systems each include an electric motor, a gearbox and a cable pulley. The follower motor system dynamics can be modeled as follows [76]

$$J_n\ddot{\theta}_n + D_n\dot{\theta}_n + d_n(t) = B_n u_n(t), \tag{3.7}$$

where $\theta_n, \dot{\theta}_n, \ddot{\theta}_n : \mathbb{R}_{\geq t_0} \to \mathbb{R}$ denote the measurable follower motor's angular position and velocity, and unmeasurable angular acceleration, for $n \in \{ex, fl\}$. The inertia constant is denoted as $J_n \in \mathbb{R}_{>0}$, the damping constant is denoted as $D_n \in \mathbb{R}$, and disturbances and any other unmodeled terms such as friction are denoted as $d_n \in \mathbb{R}$. The follower control input is denoted by $u_n : \mathbb{R}_{\geq t_0} \to \mathbb{R}$, where positive and negative signs refer to pulling and releasing cable tension, respectively. The following properties are exploited in the subsequent control design and stability analysis.

Property 16. $c_j \leq J_n \leq c_J, \forall n \in \mathcal{N}$, *where* $c_j, c_J \in \mathbb{R}_{>0}$ *are known positive constants. [76]*

Property 17. $|D_n| \leq c_{De}, \forall n \in \mathcal{N}$, *where* $c_{De} \in \mathbb{R}_{>0}$ *is a known constant. [76]*

Assumption 9. $|d_n| \leq c_{de}, \forall n \in \mathcal{N}$, *where* $c_{de} \in \mathbb{R}_{>0}$ *is a known constant.*

3.2 Control Development

The control objectives are twofold. First, the high-level knee joint controller is developed using a robust sliding-mode controller for the lead motor to track desired the knee joint angle. Second, the low-level follower controller is developed using a robust sliding-mode controller to track the lead motor angle.

3.2.1 High-Level Knee Joint Tracking Control

The measurable joint position tracking error $\xi : \mathbb{R}_{\geq t_0} \to \mathbb{R}$ and filtered tracking error $\eta : \mathbb{R}_{\geq t_0} \to \mathbb{R}$ are defined as

$$\xi(t) \triangleq q_d(t) - q(t), \tag{3.8}$$

$$\eta(t) \triangleq \dot{\xi}(t) + \alpha\xi(t), \tag{3.9}$$

where $\alpha \in \mathbb{R}_{>0}$ is a a selectable constant control gain, and $q_d(t), \dot{q}_d(t), \ddot{q}_d(t) : \mathbb{R}_{\geq t_0} \to \mathbb{R}$ are bounded kinematic desired trajectories. The open-loop error system is obtained by taking the time derivative of (3.9), pre-multiplying by M, substituting for (3.8), and then performing some algebraic manipulation as

$$M\dot{\eta} = \chi - C\eta - B_\sigma u - \xi, \tag{3.10}$$

where the auxiliary signal $\chi : \mathbb{R}_{\geq t_0} \to \mathbb{R}$ is defined as

$$\chi \triangleq M\left(\ddot{q}_d + \alpha\dot{\xi}\right) + C\left(\dot{q}_d + \alpha\xi\right) + G + P + d + \xi. \tag{3.11}$$

By using Properties 1-5, Assumption 7, (3.8), and (3.9), the auxiliary signal in (3.11) can be upper bounded as

$$|\chi| \leq \rho_1 + \rho_2\|z_1\| + \rho_3\|z_1\|^2, \tag{3.12}$$

where $\rho_1, \rho_2, \rho_3 \in \mathbb{R}_{>0}$ are known constants, and $z_1 : \mathbb{R}_{\geq t_0} \to \mathbb{R}^{2\times 1}$ is defined as

$$z_1 \triangleq \begin{bmatrix} \xi & \eta \end{bmatrix}^T. \tag{3.13}$$

Given the open-loop error system in (3.10), the knee joint controller is designed as

$$u = k_1\eta + \left(k_2 + k_3\|z_1\| + k_4\|z_1\|^2\right)\operatorname{sgn}(\eta), \tag{3.14}$$

where $k_1, k_2, k_3, k_4 \in \mathbb{R}_{>0}$ are selectable, positive gain constants. The close-loop error system is obtained by substituting (3.14) into (3.10) as

$$M\dot{\eta} = \chi - C\eta - \xi - B_\sigma \left(k_1\eta + \left(k_2 + k_3 \left\|z_1\right\| + k_4 \left\|z_1\right\|^2\right) \operatorname{sgn}(\eta)\right). \tag{3.15}$$

3.2.2 Low-Level Follower Motor Control

To mitigate cable slackness and counteracting forces, the low-level follower controller tracks the angle of the lead motor (i.e., to improve the system's response when the leader and follower switch roles). Hence, the measurable motor position tracking error $e : \mathbb{R}_{\geq t_0} \to \mathbb{R}$ and filtered tracking error $r : \mathbb{R}_{\geq t_0} \to \mathbb{R}$ are defined as

$$e(t) \triangleq \theta_{fl}(t) - \theta_{ex}(t), \tag{3.16}$$

$$r(t) \triangleq \dot{e}(t) + \beta e(t), \tag{3.17}$$

where $\beta \in \mathbb{R}_{>0}$ is a selectable, constant control gain and $\theta_{fl}, \theta_{ex} \in \mathbb{R}$ denote the previously defined angular positions of the flexion and extension motors, respectively. The follower motor control design is segregated for the extension and flexion motors as follows.

Extension motor (ex)

The follower controller for the extension motor is designed to track the flexion motor angle θ_{fl}. Taking the time derivative of (3.17), pre-multiplying by J_{ex}, substituting for (3.1), (3.2), (3.6) for $n = \{fl\}$, (3.7) for $n = \{ex\}$, (3.16), and then performing some algebraic manipulation yields

$$J_{ex}\dot{r} = \chi_{ex} - B_{ex}u_{ex} - e, \tag{3.18}$$

where the auxiliary signal $\chi_{ex} : \mathbb{R}_{\geq t_0} \to \mathbb{R}$ is defined as

$$\chi_{ex} = J_{ex}\left[\beta\dot{e} + \frac{1}{v_{fl}}M^{-1}\Big(- C\dot{q} - G - P - d + B_\sigma u\Big)\right] + D_{ex}\dot{\theta}_{ex} + d_{ex} + e. \tag{3.19}$$

By using Properties 1-5, Property 7, Properties 16-17, Assumptions 7 and 9, (3.8), (3.9), (3.13), (3.14), (3.16), (3.17), the auxiliary signal in (3.19) can be upper bounded as

$$|\chi_{ex}| \leq c_1 + c_2\|z_e\| + c_3\|z_e\|^2, \tag{3.20}$$

where $c_1, c_2, c_3 \in \mathbb{R}_{>0}$ are known constants, and $z_e : \mathbb{R}_{\geq t_0} \to \mathbb{R}^{4\times 1}$ is defined as

$$z_e \triangleq \begin{bmatrix} \xi & \eta & e & r \end{bmatrix}^T. \tag{3.21}$$

Given the open-loop error system in (3.18), the follower controller for the extension motor is designed as

$$u_{ex} = k_5 r + \left(k_6 + k_7\|z_e\| + k_8\|z_e\|^2\right)\text{sgn}(r), \tag{3.22}$$

where $k_5, k_6, k_7, k_8 \in \mathbb{R}_{>0}$ are selectable, positive gain constants. The close-loop error system for the extension motor is obtained by substituting (3.22) into (3.18) as

$$J_{ex}\dot{r} = \chi_{ex} - e - B_{ex}\left(k_5 r + \left(k_6 + k_7\|z_e\| + k_8\|z_e\|^2\right)\text{sgn}(r)\right). \tag{3.23}$$

Flexion motor (fl)

The follower controller for the flexion motor is to track the extension motor angle θ_{ex}. Taking the time derivative of (3.17), pre-multiplying by J_{fl}, substituting for (3.1), (3.2), (3.6) for $n = \{ex\}$, (3.7) for $n = \{fl\}$, (3.16), and then performing algebraic manipulation yields

$$J_{fl}\dot{r} = \chi_{fl} + B_{fl}u_{fl} - e, \tag{3.24}$$

where the auxiliary signal $\chi_{fl} : \mathbb{R}_{\geq t_0} \to \mathbb{R}$ is defined as

$$\chi_{fl} = -J_{fl}\left[\beta\dot{e} + \frac{1}{v_{ex}}M^{-1}\Big(- C\dot{q} - G - P - d + B_{\sigma}u\Big)\right] - D_{fl}\dot{\theta}_{fl} - d_{fl} + e. \tag{3.25}$$

By using Properties 1-5, Property 7, Properties 16-17, Assumptions 7 and 9, (3.8), (3.9), (3.13), (3.14), (3.16), (3.17), the auxiliary signal in (3.25) can be upper bounded as

$$|\chi_{fl}| \leq c_4 + c_5\|z_e\| + c_6\|z_e\|^2, \tag{3.26}$$

where $c_4, c_5, c_6 \in \mathbb{R}_{>0}$ are known constants, and z_e is defined as in (3.21). Given the open-loop error system in (3.24), the follower controller for the flexion motor is designed as

$$u_{fl} = -k_9 r - \left(k_{10} + k_{11}\|z_e\| + k_{12}\|z_e\|^2\right)\text{sgn}(r), \tag{3.27}$$

where $k_9, k_{10}, k_{11}, k_{12} \in \mathbb{R}_{>0}$ are selectable, positive gain constants. The close-loop error system for the flexion motor is obtained by substituting (3.27) into (3.24) as

$$J_{fl}\dot{r} = \chi_{fl} - e + B_{fl}\left(-k_9 r - \left(k_{10} + k_{11}\|z_e\| + k_{12}\|z_e\|^2\right)\text{sgn}(r)\right). \tag{3.28}$$

3.3 Stability Analysis

The stability of the high-level knee joint and low-level follower controllers are examined through the following theorems. Theorem 1 shows that exponential tracking is achieved for the knee kinematic tracking objective. Theorem 2 and 3 show that exponential tracking is achieved with the follower low-level motor controllers applied to the extension and flexion motors, respectively.

Theorem 4 develops an average dwell time analysis to provide an upper bound on the number of motor switching instances (i.e., finite number of switching events occur) and guarantee exponential tracking.

Theorem 1. *Given the closed-loop error system in (3.15), the knee joint controller in (3.14) ensures global exponential tracking in the sense that*

$$\|z_1(t)\| \leq \sqrt{\frac{b_1}{a_1}}\|z_1(t_0)\| \exp\left(-\frac{\delta}{2}(t-t_0)\right), \tag{3.29}$$

$\forall t \in (t_0, \infty)$*, where* $\delta = \frac{1}{b_1} min\{\alpha, \underline{B}k_1\}$*, provided the following sufficient gain conditions are satisfied*

$$k_2 \geq \frac{\rho_1}{\underline{B}}, k_3 \geq \frac{\rho_2}{\underline{B}}, k_4 \geq \frac{\rho_3}{\underline{B}}. \tag{3.30}$$

Proof. Let $V : \mathbb{R} \times \mathbb{R} \times \mathbb{R}_{\geq t_0} \to \mathbb{R}$ be a positive-definite, continuously differentiable function defined as

$$V = \frac{1}{2}\xi^2 + \frac{1}{2}M\eta^2, \tag{3.31}$$

which satisfies the following inequalities

$$a_1 \|z_1\|^2 \leq V(z_1, t) \leq b_1 \|z_1\|^2, \tag{3.32}$$

where $a_1 \triangleq \min\left(\frac{1}{2}, \frac{1}{2}c_m\right), b_1 \triangleq \max\left(\frac{1}{2}, \frac{1}{2}c_M\right)$, and z_1 is defined in (3.13). Let $z_1(t)$ be a Filippov solution to the differential inclusion $\dot{z}_1 \in K[h_1](z_1)$, where $K[\cdot]$ is defined as in [82] and h_1 is defined by using (3.9) and (3.15) as $h_1 \triangleq \begin{bmatrix} \dot{\xi} & M\dot{\eta} \end{bmatrix}$. The control input in (3.2) and (3.14) has the discontinuous motor effectiveness and signum function; hence, the time derivative of (3.31) exists almost everywhere (a.e.), i.e., for almost all t. Based on [83, Lemma 1], the time derivative of (3.31), $\dot{V}(z_1(t), t) \overset{a.e.}{\in} \dot{\tilde{V}}(z_1(t), t)$, where $\dot{\tilde{V}}$ is the generalized time derivative of (3.31) along the Filippov trajectories of $\dot{z}_1 = h_1(z_1)$ and is defined as in [83] as $\dot{\tilde{V}} \triangleq \bigcap_{\varsigma \in \partial V} \varsigma^T K \begin{bmatrix} \dot{\xi} & \dot{\eta} & 1 \end{bmatrix}^T (\xi, \eta, t)$. Since $V(z_1, t)$ is continuously differentiable in z_1, $\partial V =$

$\{\nabla V\}$, thus $\dot{\tilde{V}} \overset{a.e.}{\subset} \begin{bmatrix} \xi & M\eta & \frac{1}{2}\dot{M}\eta^2 \end{bmatrix} K \begin{bmatrix} \dot{\xi} & M\dot{\eta} & 1 \end{bmatrix}^T$. After substituting for (3.9) and (3.15), and canceling common terms, the generalized time derivative of (3.31) can be expressed as

$$\dot{\tilde{V}} \overset{a.e.}{\subset} -\alpha\xi^2 + \frac{1}{2}\dot{M}\eta^2 + \eta\left[\chi - C\eta - K[B_\sigma]\left(k_1\eta + \left(k_2 + k_3\left\|z_1\right\| + k_4\left\|z_1\right\|^2\right)K\left[\text{sgn}\left(\eta\right)\right]\right)\right], \tag{3.33}$$

where $K[\text{sgn}(\cdot)] = SGN(\cdot)$ such that $SGN(\cdot) = 1$ if $(\cdot) > 0$; $[-1, 1]$ if $(\cdot) = 0$; -1 if $(\cdot) < 0$, and $K[B_\sigma] \subset [\underline{B}, \bar{B}]$. Substituting for (3.12), and applying Properties 6-7, the expression in (3.33) can be upper bounded as

$$\dot{\tilde{V}} \overset{a.e.}{\leq} -\alpha\xi^2 - \underline{B}k_1\eta^2 + (\rho_1 - \underline{B}k_2)\left|\eta\right| + (\rho_2 - \underline{B}k_3)\left|\eta\right|\left\|z_1\right\| + (\rho_3 - \underline{B}k_4)\left|\eta\right|\left\|z_1\right\|^2. \tag{3.34}$$

Provided the sufficient gain conditions in (3.30), the previous inequality can be further upper bounded as

$$\dot{\tilde{V}} \overset{a.e.}{\leq} -\alpha\xi^2 - \underline{B}k_1\eta^2 \overset{a.e.}{\leq} -\delta_1\left\|z_1\right\|^2. \tag{3.35}$$

where $\delta_1 = \min\{\alpha, \underline{B}k_1\}$. Leveraging (3.32) and (3.35), the exponential tracking result in (3.29) can be obtained. Using (3.31) and (3.35), $V \in \mathcal{L}_\infty$, hence $\xi, \eta \in \mathcal{L}_\infty$, thus $z_1 \in \mathcal{L}_\infty$. From (3.14), $u \in \mathcal{L}_\infty$. Since $\xi, \eta \in \mathcal{L}_\infty$, then $\dot{\xi} \in \mathcal{L}_\infty$ from (3.9), and hence, $q, \dot{q} \in \mathcal{L}_\infty$. ■

Theorem 2. *Given the closed-loop error system in (3.23), the follower controller for the extension motor in (3.22) ensures exponential tracking in the sense that*

$$\left\|z_2(t)\right\| \leq \sqrt{\frac{b_{ex}}{a_{ex}}}\left\|z_2(t_\omega)\right\|\exp\left(-\frac{\lambda_{ex}}{2}(t - t_\omega)\right), \tag{3.36}$$

$\forall t \in (t_0, \infty), \forall\omega$, *where* $t_\omega \in \mathcal{W}$, *such that* $\mathcal{W}$ *is a finite set, indicates the time at which the follower controller is activated for the extension motor at the* ω^{th} *time, and* $\lambda_{ex} = \frac{1}{b_{ex}}min\{\beta, \underline{B}k_5\}$,

provided the following sufficient gain conditions are satisfied

$$k_6 \geq \frac{c_1}{\underline{B}}, k_7 \geq \frac{c_2}{\underline{B}}, k_8 \geq \frac{c_3}{\underline{B}}. \tag{3.37}$$

Proof. Let $V_{ex} : \mathbb{R} \times \mathbb{R} \times \mathbb{R}_{\geq t_0} \to \mathbb{R}$ be a positive definite, continuously differentiable function defined as

$$V_{ex} = \frac{1}{2}e^2 + \frac{1}{2}J_{ex}r^2, \tag{3.38}$$

which satisfies the following inequalities

$$a_{ex} \left\| z_2 \right\|^2 \leq V_{ex}(z_2, t) \leq b_{ex} \left\| z_2 \right\|^2, \tag{3.39}$$

where $z_2 : \mathbb{R}_{\geq t_0} \to \mathbb{R}^{2\times 1}$ is defined as

$$z_2 \triangleq [e \; r]^T, \tag{3.40}$$

and $a_{ex} \triangleq \min\left(\frac{1}{2}, \frac{1}{2}c_j\right), b_{ex} \triangleq \max\left(\frac{1}{2}, \frac{1}{2}c_J\right)$. Let $z_2(t)$ be a Filippov solution to the differential inclusion $\dot{z}_2 \in K[h_2](z_2)$, where h_2 is defined by using (3.17) and (3.23) as $h_2 \triangleq [\; \dot{e} \quad J_{ex}\dot{r} \;]$. The low-level control input in (3.22) has the discontinuous signum function; hence the time derivative of (3.38) exists almost everywhere (a.e.), i.e., for almost all t. Using similar arguments as in the proof of Theorem 1, after substituting for (3.17) and (3.23), and canceling common terms, the generalized time derivative of (3.38) can be expressed as

$$\dot{\tilde{V}}_{ex} \overset{a.e.}{\subset} -\beta e^2 + r\chi_{ex} - B_{ex}r\left[k_5 r + \left(k_6 + k_7 \left\| z_e \right\| + k_8 \left\| z_e \right\|^2\right) K\left[\text{sgn}(r)\right]\right]. \tag{3.41}$$

Substituting for (3.20) and applying Property 7, the expression in (3.41) can be upper bounded as

$$\dot{\tilde{V}}_{ex} \overset{a.e.}{\leq} -\beta e^2 - \underline{B}k_5 r^2 + (c_1 - \underline{B}k_6)\left|r\right| + (c_2 - \underline{B}k_7)\left|r\right|\left\|z_e\right\| + (c_3 - \underline{B}k_8)\left|r\right|\left\|z_e\right\|^2. \tag{3.42}$$

Provided the sufficient gain conditions in (3.37), the previous inequality can be further upper

bounded as

$$\dot{\tilde{V}}_{ex} \overset{a.e.}{\leq} -\beta e^2 - \underline{B} k_5 r^2 \overset{a.e.}{\leq} -\delta_2 \|z_2\|^2. \tag{3.43}$$

where $\delta_2 = \min\{\beta, \underline{B}k_5\}$. Leveraging (3.39) and (3.43), the exponential tracking result in (3.36) can be obtained. Using (3.38) and (3.43), $V_{ex} \in \mathcal{L}_\infty$, hence $e, r \in \mathcal{L}_\infty$, thus $z_2 \in \mathcal{L}_\infty$. Since $\xi, \eta \in \mathcal{L}_\infty$ in (3.8) and (3.9) proven in Theorem 1, hence $z_e \in \mathcal{L}_\infty$. From (3.22), $u_{ex} \in \mathcal{L}_\infty$. Since $e, r \in \mathcal{L}_\infty$, then $\dot{e} \in \mathcal{L}_\infty$ from (3.17), and hence, $\theta_{fl}, \theta_{ex} \in \mathcal{L}_\infty$ (i.e., $q \in \mathcal{L}_\infty$). ■

Theorem 3. *Given the closed-loop error system in (3.28), the follower controller for the flexion motor in (3.27) ensures exponential tracking in the sense that*

$$\|z_2(t)\| \leq \sqrt{\frac{b_{fl}}{a_{fl}}} \|z_2(t_\upsilon)\| \exp\left(-\frac{\lambda_{fl}}{2}(t - t_\upsilon)\right), \tag{3.44}$$

$\forall t \in (t_0, \infty), \forall \upsilon$, *where* $t_\upsilon \in \mathcal{V}$, *such that* $\mathcal{V}$ *is a finite set, indicates the time at which the follower controller is activated for the flexion motor at the* υ^{th} *time, and* $\lambda_{fl} = \frac{1}{b_{fl}} min\{\beta, \underline{B}k_9\}$, *provided the following sufficient gain conditions are satisfied*

$$k_{10} \geq \frac{c_4}{\underline{B}}, k_{11} \geq \frac{c_5}{\underline{B}}, k_{12} \geq \frac{c_6}{\underline{B}}. \tag{3.45}$$

Proof. Let $V_{fl} : \mathbb{R} \times \mathbb{R} \times \mathbb{R}_{\geq t_0} \to \mathbb{R}$ be a positive definite, continuously differentiable function defined as

$$V_{fl} = \frac{1}{2}e^2 + \frac{1}{2}J_{fl}r^2, \tag{3.46}$$

which satisfies the following inequalities

$$a_{fl} \|z_2\|^2 \leq V_{fl}(z_2, t) \leq b_{fl} \|z_2\|^2, \tag{3.47}$$

where z_2 is defined in (3.40), $a_{fl} \triangleq \min\left(\frac{1}{2}, \frac{1}{2}c_j\right), b_{fl} \triangleq \max\left(\frac{1}{2}, \frac{1}{2}c_J\right)$. Let $z_2(t)$ be a Filippov solution to the differential inclusion $\dot{z}_2 \in K[h_3](z_2)$, where h_3 is defined by using (3.17) and (3.28) as $h_3 \triangleq [\ \dot{e} \quad J_{fl}\dot{r}\ ]$. The low-level control input in (3.27) has the discontinuous signum

function; hence, the time derivative of (3.46) exists almost everywhere (a.e.), i.e., for almost all t. Using similar arguments as in the proof of Theorem 2, after substituting for (3.17) and (3.28), and canceling common terms, the generalized time derivative of (3.46) can be expressed as

$$\dot{\tilde{V}}_{fl} \overset{a.e.}{\subset} -\beta e^2 + r\chi_{fl} - B_{fl} r \left[k_9 r + \left(k_{10} + k_{11} \|z_e\| + k_{12} \|z_e\|^2\right) K \left[\text{sgn}(r)\right]\right]. \tag{3.48}$$

Substituting for (3.26) and applying Property 7, the expression in (3.48) can be upper bounded as

$$\dot{\tilde{V}}_{fl} \overset{a.e.}{\leq} -\beta e^2 - \underline{B} k_9 r^2 + (c_4 - \underline{B} k_{10}) |r| + (c_5 - \underline{B} k_{11}) |r| \|z_e\| + (c_6 - \underline{B} k_{12}) |r| \|z_e\|^2. \tag{3.49}$$

Provided the sufficient gain conditions in (3.45), the previous inequality can be further upper bounded as

$$\dot{\tilde{V}}_{fl} \overset{a.e.}{\leq} -\beta e^2 - \underline{B} k_9 r^2 \overset{a.e.}{\leq} -\delta_3 \|z\|^2, \tag{3.50}$$

where $\delta_3 = \min\{\beta, \underline{B} k_9$. Leveraging (3.47) and (3.50), the exponential tracking result in (3.44) can be obtained. Using (3.46) and (3.50), $V_{fl} \in \mathcal{L}_\infty$, hence $e, r \in \mathcal{L}_\infty$, thus $z_2 \in \mathcal{L}_\infty$. Since $\xi, \eta \in \mathcal{L}_\infty$ in (3.8) and (3.9) proven in Theorem 1, hence $z_e \in \mathcal{L}_\infty$. From (3.27), $u_{fl} \in \mathcal{L}_\infty$. Since $e, r \in \mathcal{L}_\infty$, then $\dot{e} \in \mathcal{L}_\infty$ from (3.17), and hence, $\theta_{fl}, \theta_{ex} \in \mathcal{L}_\infty$ (i.e., $q \in \mathcal{L}_\infty$). ■

Theorem 4. *A system of two electric motors has an average dwell time τ_a if there exist positive numbers $N_0 \in \mathbb{Z}^+$ and $\tau_a \in \mathbb{R}_{>0}$ such that*

$$N_n(T, t) \leq N_0 + \frac{T - t}{\tau_a}, \forall n \in \{ex, fl\}, \tag{3.51}$$

where $t \in [0, T]$, $T \in \mathbb{R}_{>0}$, and N_n is the maximum allowable number of instances at which each motor switches to become the follower motor. The switching system with two motors ensures exponential tracking with average dwell time

$$\tau_a > \frac{\ln(\mu)}{\lambda}. \tag{3.52}$$

Proof. Since $\mathcal{N}$ is a finite set, $a_2, b_2, \lambda \in \mathbb{R}$ can be chosen, independently of n, such that the inequalities (3.39), (3.47), (3.43), and (3.50) hold to yield

$$a_2 \left\| z_2 \right\|^2 \leq V_n(z_2, t) \leq b_2 \left\| z_2 \right\|^2, \forall n \in \mathcal{N}, \tag{3.53}$$

$$\dot{\tilde{V}}_n \overset{a.e.}{\leq} -\lambda \tilde{V}_n, \forall n \in \mathcal{N}, \tag{3.54}$$

where $a_2 = \min\left(a_{ex}, a_{fl}\right), b_2 = \max\left(b_{ex}, b_{fl}\right), \lambda = \min\left(\lambda_{ex}, \lambda_{fl}\right)$. Let $t_i \in \{t_1, t_2, \ldots, t_{N_n(T,0)}\} \subseteq \mathcal{W} \cup \mathcal{V}$ denotes the switching times at which the motors switch within the time interval $[0, T]$, and one of the motors is switched at t_i to become the follower motor within $[t_i, t_{i+1})$. Figure 3.3 illustrates the switching times t_i, the flexion and extension motor inputs, and the number of switching instances N_{ex} and N_{fl}. Performing some algebraic manipulation in (3.53) yields

$$V_{n(t_{i+1})}\left(z_2(t_{i+1})\right) \leq \mu V_{n(t_i)}\left(z_2(t_{i+1})\right), \tag{3.55}$$

where $\mu = \frac{b_2}{a_2}$. Based on the solution to the inequality in (3.54), a non-increasing piecewise differentiable function can be defined as

$$W(t) = e^{\lambda t} V_{n(t)}\left(z_2(t)\right). \tag{3.56}$$

Defining t_{i+1}^- as the instantaneous time before t_{i+1}, and evaluating the inequality in (3.55) at t_{i+1}^- to upperbound (3.56) yields

$$W(t_{i+1}^-) = e^{\lambda t_{i+1}^-} V_{n(t_{i+1}^-)}\left(z_2(t_{i+1}^-)\right) \tag{3.57}$$

$$\leq e^{\lambda t_{i+1}^-} \mu V_{n(t_{i+1}^-)}\left(z_2(t_{i+1}^-)\right) = \mu W(t_{i+1}^-) \tag{3.58}$$

$$\leq \mu W(t_i). \tag{3.59}$$

The inequality in (3.59) defines a relationship for W within the interval $[t_i, t_{i+1}^-]$. Applying this

relationship recursively between $[0, T^-]$ yields the following inequalities

$$W(T^-) \leq W(t^-_{N_n(T,0)}) \leq \mu^{N_n(T,0)-1} W(0). \tag{3.60}$$

Substituting (3.56) into (3.60) yields

$$e^{\lambda T} V_{n(T^-)}\left(z_2(T)\right) \leq \mu^{N_n(T,0)-1} V_{n(0)}\left(z_2(0)\right). \tag{3.61}$$

Suppose that the system has the average dwell time property in (3.51), hence (3.61) can be written as

$$V_{n(T^-)}\left(z_2(T)\right) \leq \exp\left[-\lambda T + \left(N_0 + \frac{T}{\tau_a} - 1\right)\ln(\mu)\right] V_{n(0)}\left(z_2(0)\right). \tag{3.62}$$

The previous inequality can be further upper bounded as

$$V_{n(T^-)}\left(z_2(T)\right) \leq c_A \exp\left[\left(\frac{\ln(\mu)}{\tau_a} - \lambda\right) T\right] V_{n(0)}\left(z_2(0)\right), \tag{3.63}$$

where $c_A = \exp\left[(N_0 - 1)\ln(\mu)\right]$ is a known constant. If τ_a satisfies the bound in (3.52), then $V_{n(T^-)}\left(z_2(T)\right)$ converges to zero exponentially, as developed similarly in [57]. ■

3.4 Experiment Results

An experiment with one able-bodied individual (male aged 29 years) is conducted to illustrate the performance of the developed controllers in (3.14), (3.22) and (3.27) for the control of the knee joint. Written informed consent was obtained prior to the beginning of the experiment. The participant was not informed of the desired knee joint kinematic trajectories and was asked to avoid providing voluntary input. The experimental setup is described in Section 2.3.1 with one leg in standing position and is illustrated in Figure 3.4. The desired knee angle trajectory was defined within a range of motion between 10 to 70 degrees with a period of 4 seconds. The control gains

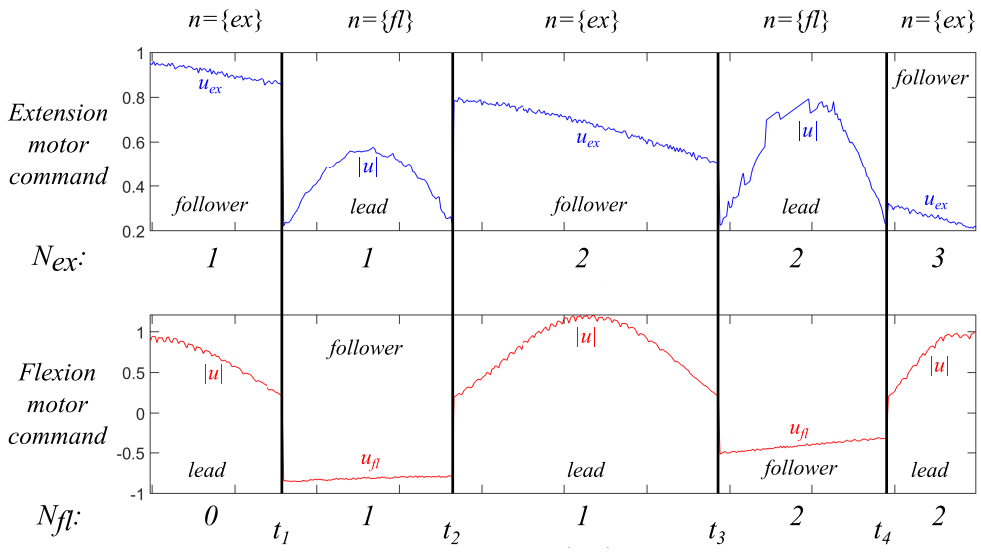

Figure 3.3: Schematic depicting the switching times t_i, flexion and extension motor inputs, and number of switching instances N_{ex}, N_{fl}. A switching instance occurs when the motors switch to become the follower motor. That is, the number of switching instances N_{ex}, N_{fl} increase each time the motors become follower motors.

introduced in (3.14), (3.22) and (3.27) were selected as follows: $\alpha = 10, \beta = 30, k_1 = 1.2, k_2 = 0.2, k_3 = 7 \times 10^{-3}, k_4 = 1 \times 10^{-4}, k_5 = 0.01, k_6 = 0.2, k_7 = 5 \times 10^{-4}, k_8 = 1 \times 10^{-5}, k_9 = 0.01, k_{10} = 0.2, k_{11} = 5 \times 10^{-4}, k_{12} = 1 \times 10^{-5}$. The experiment was implemented for a duration of $T = 80$ seconds. Figure 3.5 depicts the knee joint tracking performance (top) and the high-level knee control input u (bottom). Figure 3.6 presents the motor follower angle performance (top), the applied follower motor inputs (middle), and the number of switching instances over each cycle (bottom). During the experiment, 174 switching instances were counted for both extension and flexion motors, thus $N_{ex}(80, 0) = N_{fl}(80, 0) = 174$ in (3.51).

3.5 Discussion

The experimental results demonstrate the feasibility of the developed high-level knee joint tracking controller in (3.14) and low-level motors kinematic tracking controllers in (3.22) and (3.27).

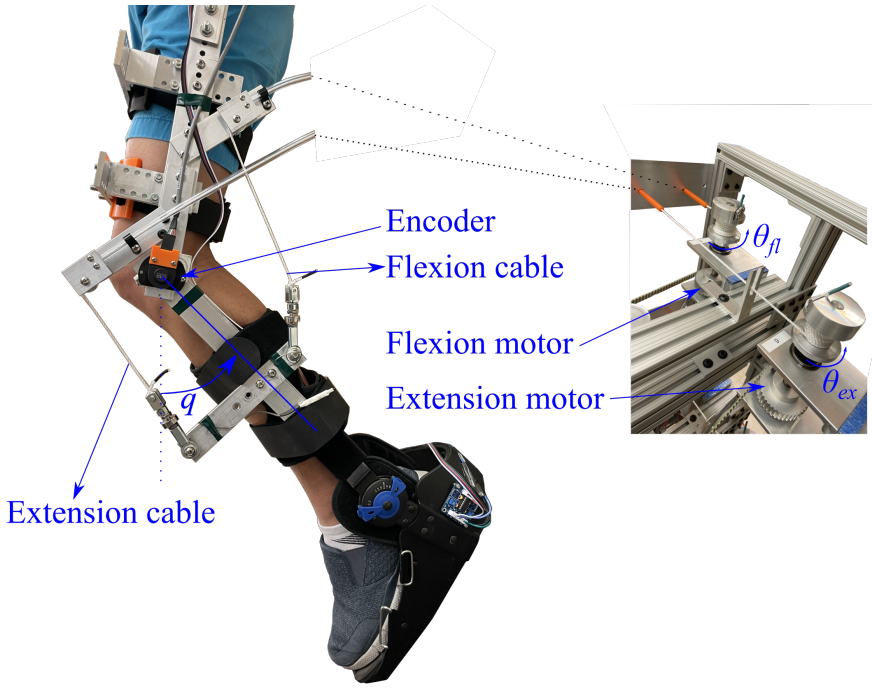

Figure 3.4: The cable-driven exoskeleton uses electric motors to actuate flexion and extension cables to apply torque at the knee joint.

As depicted in Figure 3.5, the developed high-level knee joint controller has an average tracking error of -3.9 ± 3.7 deg during the experiment. In the standing position, the kinematic tracking error during knee flexion is larger than during knee extension, which resulted in higher control input (i.e., to compensate for gravity).

The developed low-level controllers for the pair of motors yield an average kinematic tracking error of -5.3 ± 63 deg. The developed control algorithm distributed the high-level and low-level control inputs for different motors in Figure 3.6 (middle). The number of switching instances for both motors over each knee movement cycle are illustrated in Figure 3.6 (bottom).

The obtained experimental result shows the feasibility of the developed high-level knee joint and low-level motor controllers. The control design presented in this chapter demonstrates the switching control design for a single joint. This fundamental control design is leveraged to control the knee and hip joints bilaterally during treadmill walking as implemented in Chapter 4.

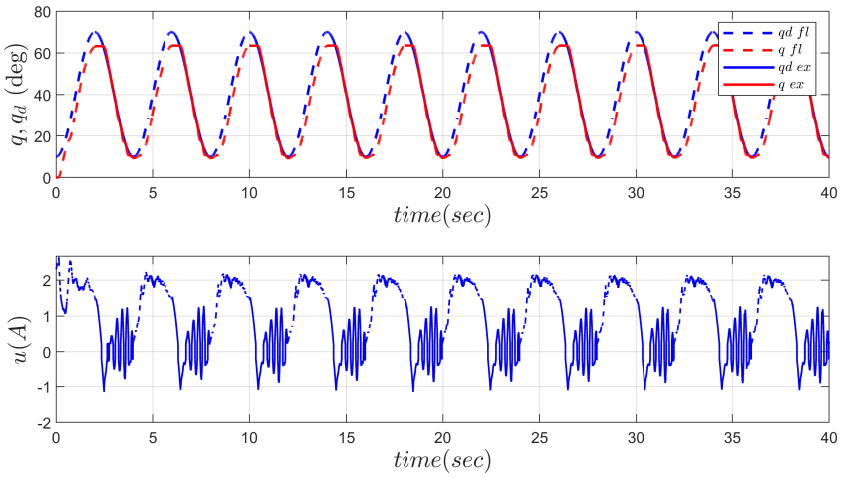

Figure 3.5: Knee joint desired trajectory q_d and actual knee joint angle q (top). Knee flexion (fl) is depicted with dashed lines and knee extension (ex) is depicted with solid lines. The high-level joint tracking control input u (bottom).

3.6 Concluding Remarks

A two-layer control system was developed for a cable-driven exoskeleton to apply torque at the knee joint. A robust sliding-mode controller was designed to track a desired knee kinematic trajectory. A switched systems strategy was developed to activate a pair of electric motors using sliding-mode controllers to achieve bi-directional control. The motivation of the control methods was to achieve the desired joint kinematics and track a motor angle objective to mitigate potential cable slackness and improve response in the system. A Lyapunov-based stability analysis is developed to ensure exponential tracking for joint tracking error and for the low-level motor tracking objective. An average dwell time condition is developed to compute a maximum allowable switching number to guarantee exponential tracking for the switching motors.

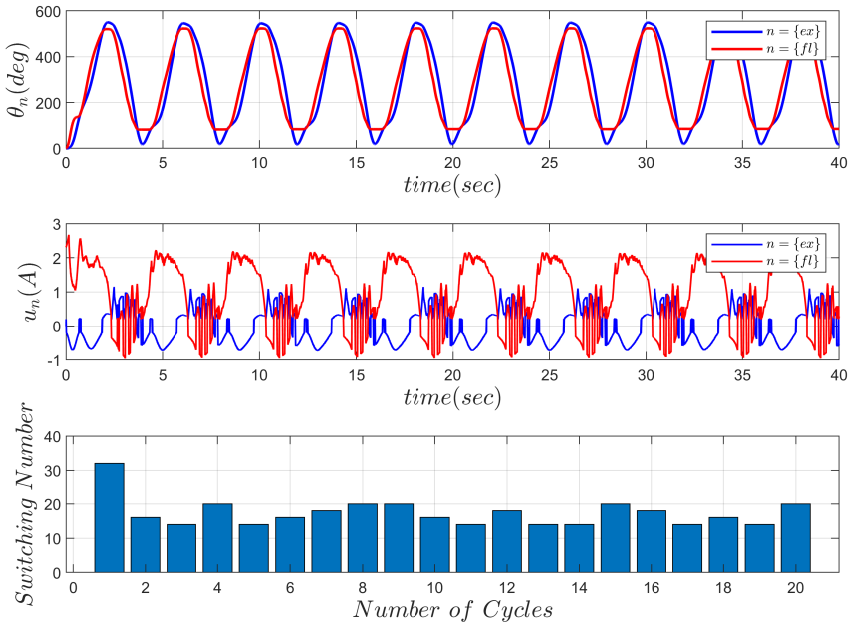

Figure 3.6: Motor tracking performance illustrating the motor flexion angle θ_{fl} (red) and motor extension angle θ_{ex} (blue) (top). The low-level motor follower control input for flexor u_{fl} (red) and extensor u_{ex} (blue) (middle). The number of switching instances for both extension and flexion motors over each cycle (bottom).

Chapter 4

Closed-loop Torque and Kinematic Control of a Hybrid Lower-limb Exoskeleton for Treadmill Walking

In this chapter and in the work in [62], kinematic and torque tracking controllers are designed to activate the electric motors of a cable-driven lower-limb exoskeleton and muscles via FES for treadmill walking at a constant speed. The hybrid exoskeleton and human system are modeled as in Chapter 2 in which the leg dynamics are modeled as a switched system to characterize the gait phase transitions during walking. A nonlinear robust controller is used to activate the quadriceps and hamstrings muscle groups via FES to achieve kinematic tracking about the knee joint. Electric motors adjust the knee joint stiffness throughout the gait cycle using an integral torque feedback controller. A robust sliding-mode controller is developed to achieve hip joint kinematic tracking using electric motors. The low-level motor controllers developed in Chapter 3 are used to switch between the pair of motors to achieve flexion and extension motion for the hip and knee joints. A Lyapunov-based stability analysis is developed to ensure exponential tracking of the kinematic and torque closed-loop error systems, while guaranteeing that the control input signals

remain bounded. The developed controllers were tested in real-time walking experiments on a treadmill in three able-bodied individuals at two gait speeds.

4.1 Control Development

The control design is segregated for the stance and swing phases of walking. To absorb the foot impact and guarantee trunk support during early stance, the stiffness in the knee joint is increased and knee extensor activity is modulated [84], which ultimately contributes to enable body propulsion and initiate swing. On the other hand, during the swing phase, leg stiffness is reduced to increase compliance and allow smooth knee joint kinematics and prepare for heel strike (i.e., contact with the ground). Hence, the knee joint stiffness contributes for shaping the leg dynamics along with the hip joint that assist body propulsion and preserve the rhythmic walking motion [42], [85]. Inspired by such joint behaviors, a multiple control objective is developed to adjust the joint stiffness and kinematics on both phases, while ensuring a stable rhythmic walking motion.

Two control objectives are developed as depicted in Figure 4.1. The first objective is to design kinematic controllers (κ) to track knee and hip joint trajectories. A pair of electric motors achieve the kinematic tracking objective for the hip joints, whereas FES applied to the quadriceps and hamstrings achieve kinematic tracking for the knee joints. The second objective is to design a knee joint stiffness controller (s) throughout the gait cycle using the electric motors that actuate the knee joints. Since the electric motors and FES cooperate to achieve both control objectives, the control effectiveness matrices can be segregated for the kinematic and stiffness control objectives as depicted in Figure 4.1.C, where the lumped effectiveness B_κ and B_s are defined for the kinematic and stiffness control loops, respectively. The control design for each objective is developed in the subsequent subsections. A robust control technique is applied to track the desired angle trajectories and a torque controller is designed to track the desired knee stiffness on both gait phases.

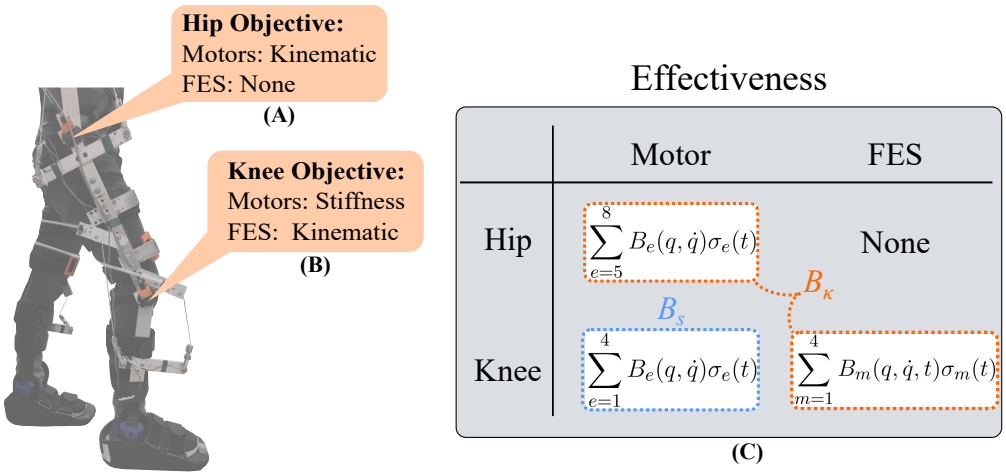

Figure 4.1: Schematic of the kinematic (κ) and stiffness (s) control tracking objectives. **(A)** The hip joint is actuated only by the electric motors to achieve kinematic tracking (i.e., no FES is applied). **(B)** The knee joint is controlled to achieve both control objectives: electric motors track the stiffness objective and the muscles track the kinematic objective. **(C)** The table shows the control effectiveness matrices associated with the kinematic and stiffness control objective, B_κ and B_s, respectively.

The following properties are exploited in the subsequent control design and stability analysis.

Property 18. *The lumped kinematic switching control effectiveness is a diagonal matrix and is bounded as* $\underline{B}_\kappa \|\xi\|^2 \leq \xi^T B_\kappa \xi \leq \overline{B}_\kappa \|\xi\|^2, \forall \xi \in \mathbb{R}^4$, *where* $\underline{B}_\kappa$ *and* $\overline{B}_\kappa$ *are known positive constants.*

Property 19. *The lumped stiffness switching control effectiveness is a diagonal matrix and is bounded as* $\underline{B}_s \|\zeta\|^2 \leq \zeta^T B_s \zeta \leq \overline{B}_s \|\zeta\|^2, \forall \zeta \in \mathbb{R}^2$, *where* $\underline{B}_s$ *and* $\overline{B}_s$ *are known positive constants.*

4.1.1 Kinematic Control

The human-exoskeleton dynamics with motor and muscle torque inputs in (2.3) can be expressed in terms of the kinematic control objective as

$$M_\rho(q)\ddot{q} + C_\rho(q,\dot{q})\dot{q} + G_\rho(q) + P_\rho(q,\dot{q}) + d_\rho(t) = \underbrace{B_\kappa(q,\dot{q},t)u_\kappa(t)}_{\tau_\kappa} + \tau_s, \tag{4.1}$$

$\forall \rho \in \mathcal{R}$, where $\tau_\kappa, \tau_s \in \mathbb{R}^4$ are the torque inputs generated by the kinematic and stiffness controllers, $u_\kappa : \mathbb{R}_{\geq t_0} \to \mathbb{R}^4$ is the kinematic control input, and the lumped kinematic control effectiveness $B_\kappa \in \mathbb{R}^{4\times 4}_{>0}$ is a positive definite diagonal matrix, defined as

$$B_\kappa \triangleq \sum_{e=5}^{8} B_e(q, \dot{q})\sigma_e(t) + \sum_{m=1}^{4} B_m(q, \dot{q}, t)\sigma_m(t), \tag{4.2}$$

where the hip motors dedicated for kinematic tracking are represented by the motor index $e = \{5, 6, 7, 8\}$ as described in Table 2.1.

The measurable angular position tracking error $e_\kappa : \mathbb{R}_{\geq t_0} \to \mathbb{R}^4$ and filtered tracking error $r_\kappa : \mathbb{R}_{\geq t_0} \to \mathbb{R}^4$ are defined as

$$e_\kappa(t) \triangleq q_d(t) - q(t), \tag{4.3}$$

$$r_\kappa(t) \triangleq \dot{e}_\kappa(t) + \alpha e_\kappa(t), \tag{4.4}$$

where $\alpha \in \mathbb{R}$ is a selectable positive control gain and $q_d(t), \dot{q}_d(t), \ddot{q}_d : \mathbb{R}_{\geq t_0} \to \mathbb{R}^4$ are bounded desired joint trajectories. Taking the time derivative of (4.4), substituting for (4.1) and (4.3), and then performing algebraic manipulation yields

$$\dot{r}_\kappa = \chi_\rho - e_\kappa + M_\rho^{-1}\left(-B_\kappa u_\kappa - \tau_s\right), \tag{4.5}$$

where the auxiliary signal $\chi_\rho : \mathbb{R}_{\geq t_0} \to \mathbb{R}^4$ is defined as

$$\chi_\rho = \ddot{q}_d + \alpha \dot{e}_\kappa + e_\kappa + M_\rho^{-1}\left(C_\rho \dot{q} + G_\rho + P_\rho + d_\rho\right). \tag{4.6}$$

By using Properties 2-5, Assumption 7, (4.3), and (4.4), the auxiliary signal in (4.6) can be upper bounded as

$$\|\chi_\rho\| \leq c_1 + c_2 \|z_\kappa\| + c_3 \|z_\kappa\|^2, \forall \rho \in \mathcal{R}, \tag{4.7}$$

where $c_1, c_2, c_3 \in \mathbb{R}_{>0}$ are positive constants and $z_\kappa \triangleq \begin{bmatrix} e_\kappa^T & r_\kappa^T \end{bmatrix}^T : \mathbb{R}_{\geq t_0} \to \mathbb{R}^8$. Given the open-loop error system in (4.5), the control input $u_\kappa \in \mathbb{R}^4$ can be designed as

$$u_\kappa = k_1 r_\kappa + (k_2 + k_3 \|z_\kappa\| + k_4 \|z_\kappa\|^2 + k_5 \|u_s\|)\text{sgn}(r_\kappa), \tag{4.8}$$

where $k_1, k_2, k_3, k_4, k_5 \in \mathbb{R}_{>0}$ are selectable positive gains, and u_s is a subsequently designed stiffness control input. The kinematic control input in (4.8) includes a feedback term and robust control terms to reject the disturbance, and compensate for the state-dependent uncertain terms in (4.6), and compensate for the stiffness input cross-term. The closed-loop error system can be obtained by substituting (4.8) into the open-loop error system (4.5) as

$$\dot{r}_\kappa = \chi_\rho - M_\rho^{-1}\tau_s - e_\kappa - M_\rho^{-1}B_\kappa\Big(k_1 r_\kappa + (k_2 + k_3 \|z_\kappa\| + k_4 \|z_\kappa\|^2 + k_5 \|u_s\|)\text{sgn}(r_\kappa)\Big). \tag{4.9}$$

Remark 2. To implement (4.8), u_s is initialized at zero (i.e., $[0, 0]^T$), such that $\|u_s\|$ is bounded at $t = t_0$.

4.1.2 Stiffness Control

The stiffness control objective is to track a desired torque for the knee joints. Hence, the knee-shank dynamics in (2.3) can expressed as

$$M_{\rho k}(q_k)\ddot{q}_k + C_{\rho k}(q_k, \dot{q}_k)\dot{q}_k + G_{\rho k}(q_k) + P_{\rho k}(q_k, \dot{q}_k) + d_{\rho k}(t) = \tau_{\kappa k}(t) + \underbrace{B_s(q, \dot{q})u_s(t)}_{\tau_{sk}}, \tag{4.10}$$

where the subscript k refers to the knee-joint dynamics, $q_k, \dot{q}_k \in \mathbb{R}^2$ are the knee joint angles and velocities, respectively. The terms $M_{\rho k} \in \mathbb{R}^{2\times 2}_{>0}$, $C_{\rho k} \in \mathbb{R}^{2\times 2}$, and $G_{\rho k} \in \mathbb{R}^2$ denote the inertia, centripetal-Coriolis, and gravitational effects, respectively; $P_{\rho k} \in \mathbb{R}^2$, $\tau_{\kappa k} \in \mathbb{R}^2$ denote damping and viscoelastic effects, and torque applied about the knee joint by the kinematic con-

troller, respectively; $d_{\rho k} \in \mathbb{R}^2$ denotes unmodeled terms and disturbances acting about the knee joints (e.g., interaction forces induced by the hip joints). The stiffness control input is denoted by $u_s : \mathbb{R}_{\geq t_0} \to \mathbb{R}^2$ and the lumped stiffness control effectiveness $B_s \in \mathbb{R}^{2\times 2}_{>0}$ is a positive definite diagonal matrix, defined as

$$B_s \triangleq \sum_{e=1}^{4} B_e(q, \dot{q})\sigma_e(t), \tag{4.11}$$

where the effectiveness dimension has been reduced from 4×4 to 2×2 since the stiffness control objective is developed only for the knee joints. Hence, the torque due to the stiffness controller τ_s about the hip joints is zero (i.e., $\tau_s = [\tau_{sk}^T, 0, 0]^T$). The knee joint torque inputs generated by the kinematic and stiffness controllers are denoted as $\tau_{\kappa k}, \tau_{sk} \in \mathbb{R}^2$, respectively.

To generate the desired torque, a stiffness model is designed as

$$\tau_d(t) = K(t)\left(q_{dk} - q_k\right), \tag{4.12}$$

where $K(t) : \mathbb{R}_{\geq t_0} \to \mathbb{R}^{2\times 2}_{>0}$ is a selectable positive definite diagonal matrix representing virtual knee-joint springs, and $\tau_d \in \mathbb{R}^2$ denotes the generated desired knee torque trajectories. The desired spring matrix is designed using Fourier series with periodic, continuous and differentiable properties, such that $\overline{K}\left\|\zeta\right\|^2 \leq \zeta^T K(t)\zeta \leq \underline{K}\left\|\zeta\right\|^2, \forall \zeta \in \mathbb{R}^2$, where $\overline{K}$ and $\underline{K}$ are known positive constants denoting the upper and lower bounds of K, respectively.

An integral-like torque tracking error $e_s : \mathbb{R}_{\geq t_0} \to \mathbb{R}^2$ is defined as

$$e_s(t) \triangleq \int_{t_0}^{t} \left(\tau_d\left(\varphi\right) - \tau_k\left(\varphi\right)\right) d\varphi, \tag{4.13}$$

where $\tau_k \triangleq \tau_{\kappa k} + \tau_{sk}$ is the measurable torque applied about the knee joints. Taking the derivative of (4.13), setting the initial conditions to zero, and substituting the measurable torque inputs from the right-hand side in (4.10) and (4.12) yields

$$\dot{e}_s(t) = K(t)e_{\kappa k} - \tau_{\kappa k} - B_s u_s, \tag{4.14}$$

where $e_{\kappa k}, \dot{e}_{\kappa k} \in \mathbb{R}^2$ are the knee joint position and velocity tracking errors defined as $e_{\kappa k} \triangleq q_{dk} - q_k$, $\dot{e}_{\kappa k} \triangleq \dot{q}_{dk} - \dot{q}_k$. The stiffness control input $u_s \in \mathbb{R}^2$ is designed as

$$u_s(t) = k_6 e_s + (k_7 e_{\kappa k} + k_8 \|u_{\kappa k}\|)\text{sgn}(e_s), \tag{4.15}$$

where $k_6, k_7, k_8 \in \mathbb{R}_{>0}$ are selectable positive control gains and $u_{\kappa k} \in \mathbb{R}^2$ is the knee joint kinematic controller input. The closed-loop stiffness error system is obtained by substituting (4.15) into (4.14) to yield

$$\dot{e}_s = K(t)e_{\kappa k} - \tau_{\kappa k} - B_s\Big(k_6 e_s + (k_7 e_{\kappa k} + k_8 \|u_{\kappa k}\|)\text{sgn}(e_s)\Big). \tag{4.16}$$

4.1.3 Actuator Control Inputs

The kinematic and stiffness control tracking objectives combine muscle and motor inputs. Hence, the relationship between the implementable control inputs u_e and u_m and the designed u_κ and u_s can be defined as

$$u_e = k_e \left(D_e u_\kappa + D_s u_s\right), \tag{4.17}$$

$$u_m = k_m D_m u_\kappa, \tag{4.18}$$

where $D_e = diag\left(\begin{bmatrix} 0 & 0 & 1 & 1 \end{bmatrix}\right)$, $D_s = \begin{bmatrix} 1 & 0 & 0 & 0 \\ 0 & 1 & 0 & 0 \end{bmatrix}^T$, and $D_m = diag\left(\begin{bmatrix} 1 & 1 & 0 & 0 \end{bmatrix}\right)$ are control allocation matrices, $diag$ denotes diagonal matrices, and $k_e, k_m \in \mathbb{R}_{>0}, \forall m \in \mathcal{M}, \forall e \in \mathcal{E}$ are selectable positive control gains for the electric motors and muscle groups, respectively.

4.2 Stability Analysis

The stability of the kinematic and stiffness controllers that activate the electric motors and muscles can be examined independently through the following two theorems. Theorem 5 shows that given the closed-loop kinematic error system in (4.9), the joint kinematic controller in (4.8) achieves exponential tracking. Theorem 6 shows that given the closed-loop stiffness error system in (4.16), the torque controller in (4.15) achieves exponential tracking. All the control inputs and error signals are shown to be bounded.

Theorem 5. *Given the closed-loop error system in (4.9), the controller in (4.8) ensures exponential tracking in the sense that*

$$\|z_\kappa\| \leq \sqrt{\frac{\lambda_{\bar{\kappa}}}{\lambda_{\underline{\kappa}}}} \|z_\kappa(t_0)\| \exp\left(-\frac{\psi_\kappa}{2}(t-t_0)\right), \tag{4.19}$$

provided the following sufficient gain conditions are satisfied

$$k_2 \geq \frac{c_1 c_M}{\underline{B}_\kappa}, k_3 \geq \frac{c_2 c_M}{\underline{B}_\kappa}, k_4 \geq \frac{c_3 c_M}{\underline{B}_\kappa}, k_5 \geq \frac{c_M \overline{B}_s}{c_m \underline{B}_\kappa}. \tag{4.20}$$

Proof. Let $V_\kappa : \mathbb{R}^4 \times \mathbb{R}^4 \times \mathbb{R}_{\geq t_0} \to \mathbb{R}$ be a nonnegative, continuously differentiable function defined as

$$V_\kappa = \frac{1}{2} e_\kappa^T e_\kappa + \frac{1}{2} r_\kappa^T r_\kappa, \tag{4.21}$$

which satisfies the following inequalities

$$\lambda_{\underline{\kappa}} \|z_\kappa\|^2 \leq V_\kappa(z_\kappa, t) \leq \lambda_{\bar{\kappa}} \|z_\kappa\|^2, \tag{4.22}$$

where $\lambda_{\underline{\kappa}}, \lambda_{\bar{\kappa}} \in \mathbb{R}_{>0}$ are known positive bounding constants. The control input in (4.8) has the discontinuous signum function (i.e., sliding-mode), and the torque inputs in (2.4)-(2.5) have input switching effects; hence, the system's trajectories cannot be solved in a classical sense. Let $z_\kappa(t)$ be a Filippov solution to the differential inclusion $\dot{z}_\kappa \in \mathcal{K}[h_\kappa](z_\kappa)$, where $\mathcal{K}[\cdot]$ is defined as [82]

and h_κ is defined using (4.4) and (4.9) as $h_\kappa \triangleq \begin{bmatrix} h_1 & h_2 \end{bmatrix}$, where $h_1 \triangleq r_\kappa - \alpha e_\kappa$ and $h_2 \triangleq \chi_\rho - M_\rho^{-1}\tau_s - e_\kappa - M_\rho^{-1}\mathcal{K}[B_\kappa]\Big(k_1 r_\kappa + \big(k_2 + k_3 \|z_\kappa\| + k_4 \|z_\kappa\|^2 + k_5 \|u_s\|\big)\,\mathcal{K}[\text{sgn}(r_\kappa)]\Big)$. Hence, the time derivative of (4.21) exists almost everywhere (a.e.), i.e., for almost all time. Based on [83, Lemma 1], the time derivative of (4.21), $\dot{V}_\kappa(z_\kappa(t),t) \overset{a.e.}{\in} \dot{\tilde{V}}_\kappa(z_\kappa(t),t)$, where $\dot{\tilde{V}}_\kappa$ is the generalized time derivative of (4.21) along the Filippov trajectories of $\dot{z}_\kappa = h_\kappa(z_\kappa)$ and is defined as in [83] as $\dot{\tilde{V}}_\kappa \triangleq \bigcap_{\xi \in \partial V_\kappa} \xi^T K \begin{bmatrix} \dot{e}_\kappa & \dot{r}_\kappa & 1 \end{bmatrix}^T (e_\kappa, r_\kappa, t)$. Since $V_\kappa(z_\kappa,t)$ is continuously differentiable in z_κ, $\partial V_\kappa = \{\nabla V_\kappa\}$, thus $\dot{\tilde{V}}_\kappa \overset{\text{a.e.}}{\subset} \begin{bmatrix} e_\kappa & r_\kappa \end{bmatrix} K \begin{bmatrix} \dot{e}_\kappa & \dot{r}_\kappa \end{bmatrix}^T$. Therefore, after taking the time derivative, the generalized time derivative of (4.21) can be expressed as $\dot{\tilde{V}}_\kappa \overset{a.e.}{\subset} e_\kappa^T \dot{e}_\kappa + r_\kappa^T \dot{r}_\kappa$. After substituting (4.3), (4.4), and (4.9), the generalized time derivative of (4.21) can be expressed as

$$\begin{aligned}\dot{\tilde{V}}_\kappa \overset{a.e.}{\subset}\ & -e_\kappa^T \alpha e_\kappa + r_\kappa^T \chi_\rho - r_\kappa^T M_\rho^{-1}\tau_s \\ & - r_\kappa^T M_\rho^{-1}\mathcal{K}[B_\kappa]\Big(k_1 r_\kappa + \Big(k_2 + k_3 \|z_\kappa\| + k_4 \|z_\kappa\|^2 + k_5 \|u_s\|\Big)\mathcal{K}[\text{sgn}(r_\kappa)]\Big). \quad (4.23)\end{aligned}$$

The generalized time derivative of (4.21) can be upper bounded using Property 18 as

$$\begin{aligned}\dot{\tilde{V}}_\kappa \overset{a.e.}{\leq}\ & -\alpha \|e_\kappa\|^2 - \frac{\underline{B}_\kappa}{c_M} k_1 \|r_\kappa\|^2 + \left(c_1 - k_2 \frac{\underline{B}_\kappa}{c_M}\right)\|r_\kappa\| + \left(c_2 - k_3 \frac{\underline{B}_\kappa}{c_M}\right)\|r_\kappa\|\,\|z_\kappa\| \\ & + \left(c_3 - k_4 \frac{\underline{B}_\kappa}{c_M}\right)\|r_\kappa\|\,\|z_\kappa\|^2 + \left(\frac{\overline{B}_s}{c_m} - k_5 \frac{\underline{B}_\kappa}{c_M}\right)\|r_\kappa\|\,\|u_s\|. \quad (4.24)\end{aligned}$$

Provided the gain conditions in (4.20) are satisfied, the inequality in (4.24) can be further upper bounded as

$$\dot{\tilde{V}}_\kappa \overset{a.e.}{\leq} -W(z_\kappa), \quad (4.25)$$

where $W \triangleq \alpha \|e_\kappa\|^2 + \frac{\underline{B}_\kappa}{c_M} k_1 \|r_\kappa\|^2$ is a positive definite function; hence, (4.25) satisfies the conditions in [57] to guarantee that (4.21) is a common Lyapunov function across subsystems $\rho = \{1, 2\}$ (i.e., stance and swing phases of walking). The upper bound in (4.22) can be substi-

tuted into the previous expression to yield

$$\dot{\tilde{V}}_{\kappa} \overset{a.e.}{\leq} -\psi_{\kappa}\tilde{V}_{\kappa}, \tag{4.26}$$

where $\psi_{\kappa} \triangleq \frac{1}{\lambda_{\bar{\kappa}}} \min\left(\alpha, \frac{B_{\kappa}}{c_M} k_1\right)$. Leveraging (4.22) and (4.26), the result in (4.19) can be obtained. Using (4.21) and (4.26), $V_{\kappa} \in \mathcal{L}_{\infty}$, hence, $e_{\kappa}, r_{\kappa} \in \mathcal{L}_{\infty}$, which implies that $z_{\kappa} \in \mathcal{L}_{\infty}$, and thus $q, \dot{q} \in \mathcal{L}_{\infty}$. ■

Theorem 6. *Given the closed-loop error system in (4.16), the controller in (4.15) ensures exponential tracking in the sense that*

$$\|e_s\| \leq \|e_s(t_0)\| \exp\left(-\frac{\psi_s}{2}(t - t_0)\right), \tag{4.27}$$

provided the following sufficient gain conditions are satisfied

$$k_7 \geq \frac{\overline{K}}{\underline{B}_s}, k_8 \geq \frac{\overline{B}_{\kappa}}{\underline{B}_s}. \tag{4.28}$$

Proof. Let $V_s : \mathbb{R}^2 \times \mathbb{R}_{\geq t_0} \to \mathbb{R}$ be a nonnegative, continuously differentiable function defined as

$$V_s = \frac{1}{2} e_s^T e_s. \tag{4.29}$$

Let $e_s(t)$ be a Filippov solution to the differential inclusion $\dot{e}_s \in \mathcal{K}[h](z_q)$, where $\mathcal{K}[\cdot]$ is defined as [82] and $h \triangleq h_3$ is defined by using (4.16) as $h_3 \triangleq K(t)e_{\kappa k} - \tau_{\kappa k} - \mathcal{K}[B_s](k_6 e_s + (k_7 e_{\kappa k} + k_8 \|u_{\kappa k}\|)\mathcal{K}[\text{sgn}(e_s)])$. The control input in (4.15) includes the discontinuous signum function and the closed-loop error system in (4.16) has the lumped switched stiffness control effectiveness. Hence, the time derivative of (4.29) exists almost everywhere (a.e.), i.e., for almost all time. After substituting for (4.16) and using similar arguments as in the proof of Theorem 5,

the generalized time derivative of (4.29) can be expressed as

$$\dot{\tilde{V}}_s \overset{a.e.}{\subset} e_s^T \Big(K(t) e_{\kappa k} - \tau_{\kappa k} - \mathcal{K}[B_s](k_6 e_s + (k_7 e_{\kappa k} + k_8 \left\| u_{\kappa k} \right\|)\mathcal{K}[\text{sgn}(e_s)]) \Big). \tag{4.30}$$

An upper bound for the previous expression can be obtained by using Property 19 and substituting the upper bound of $K(t)$ to yield

$$\dot{\tilde{V}}_s \overset{a.e.}{\leq} -\underline{B}_s k_6 \left\| e_s \right\|^2 + \left\| e_s \right\| \left\| e_{\kappa k} \right\| \left(\overline{K} - k_7 \underline{B}_s \right) + \left\| e_s \right\| \left\| u_{\kappa k} \right\| \left(\overline{B}_\kappa - k_8 \underline{B}_s \right). \tag{4.31}$$

Provided the gain conditions in (4.28) are satisfied, the inequality in (4.31) can be further upper bounded as

$$\dot{\tilde{V}}_s \overset{a.e.}{\leq} -\psi_s \tilde{V}_s, \tag{4.32}$$

where $\psi_s \triangleq \underline{B}_s k_6$. Using (4.29) and (4.32), $V_s \in \mathcal{L}_\infty$, hence, $e_s \in \mathcal{L}_\infty$. Given the fact that $e_\kappa \in \mathcal{L}_\infty$ from Theorem 5, which implies that $\tau_d \in \mathcal{L}_\infty$ in (4.12), then, $\tau_k \in \mathcal{L}_\infty$ in (4.13). Based on $\tau_k \triangleq \tau_{\kappa k} + \tau_{sk}$, leveraging Remark 2, and substituting (4.8) in $\tau_{\kappa k}$, it can be concluded that $u_s \in \mathcal{L}_\infty$. Thus, from (4.8) $u_\kappa \in \mathcal{L}_\infty$, which further implies that $u_m, u_e \in \mathcal{L}_\infty$ from (4.17) and (4.18). ■

4.3 Experiment Results

Experiments are provided to demonstrate the performance of the kinematic and stiffness controllers developed in (4.8) and (4.15) to control the knee and hip joints. Three able-bodied individuals (two males aged 29 years and one female aged 29 years) participated in the exoskeleton protocol at Syracuse University. Written informed consent was obtained from each participant, as approved by the Institutional Review Board at Syracuse University. The participants were instructed to avoid voluntarily contributing to the treadmill walking task. To mitigate the influence of the ankle joint for propulsion, an orthotic boot is used to mechanically lock the ankle and pro-

vide foot cushion. The individuals could not see the walking performance plots during the experiments. The experimental setup is described in Section 2.3.1.

A walking pretrial was performed wearing the exoskeleton in passive mode (i.e., the exoskeleton did not provide assistance to the participant) to record walking data for each participant to generate the smooth desired kinematic trajectories $q_d, \dot{q}_d$. The joint torque τ_k were computed in real-time based on the force measurement from the load cells multiplied by the computed moment arm, which is a function of joint angles. The treadmill walking experiments have a duration of 3 minutes.

The desired stiffness values $K(t) \triangleq diag\left(\begin{bmatrix} K_R & K_L \end{bmatrix}\right)$ were designed using Fourier series as $K_R(t) = K_L(t+1) = \frac{1}{2}a_0 + \sum_{n=1}^{30} b_n \sin(n\pi t)$, where $a_0 = K_1 + K_2, b_n = \left(\frac{1}{n\pi}\right)\left(K_2 - K_1 + K_1(-1)^n - k_2(-1)^n\right)$ with $K_1 = 10, K_2 = 4$. The control gains were tuned to achieve satisfactory tracking performance during preliminary testing following the guidelines described in the Appendix. The control gains introduced in (4.8) and (4.15) were selected as follows: $k_1 = 0.4, k_2 = 0.35, k_3 = 0.002, k_4 = 0.0001, k_5 = 0.05, \alpha = 20, k_6 = 0.05, k_7 = 6.5, k_8 = 0.05$. The selectable positive control gains in (4.17) and (4.18) are $k_e = 0.8$ and $k_m \in [8, 12]$.

Table 4.1 summarizes the root-mean-squared (RMS) and average of the kinematic and stiffness tracking errors for all subjects with the two tested gait speeds. The experimental results were analyzed after the sixth gait cycle from the point at which the treadmill reached the desired steady-state gait speed. During the first five gait cycles the participants began stepping on the treadmill to smoothly reach the steady state constant walking speed. The kinematic tracking performance for two participants at different gait speeds is illustrated in Figures 4.2-4.3, where the desired joint trajectories are depicted in blue and the actual joint angles are in depicted in red. The kinematic joint trajectories corresponding to each gait cycle during a complete treadmill walking experiment are depicted as a function of gait cycle percentage in Figure 4.4.

The control inputs are presented in Figure 4.5; the quadriceps and hamstrings muscle stimula-

Table 4.1: Tracking results for each participant at high (0.8 mph) and low (0.5 mph) treadmill walking speeds*: RMS kinematic tracking error (moving window in seconds to complete a gait cycle)[1], average of kinematic tracking error $\overline{e_\kappa}$, and average of stiffness tracking error $\overline{e_s}$ [2].

Subject-Speed	**Leg**	**RMS Kinematic Error (deg)**		$\overline{e_\kappa}$ **(deg)**		$\overline{e_s}$ **(Nms)**
		Knee	**Hip**	**Knee**	**Hip**	**Knee**
S1-High	R	2.6 ± 1.8	2.1 ± 1.2	-0.1 ± 1.3	-0.5 ± 0.8	37.9 ± 6.0
	L	5.4 ± 3.2	2.3 ± 1.5	-5.2 ± 1.9	-1.3 ± 0.7	37.3 ± 4.7
S1-Low	R	3.5 ± 2.0	1.1 ± 1.0	-3.1 ± 1.9	-0.4 ± 1.2	40.5 ± 21.4
	L	3.7 ± 2.0	2.4 ± 2.0	-3.6 ± 1.3	-2.2 ± 1.5	67.7 ± 27.4
S2-High	R	3.0 ± 2.2	1.4 ± 1.0	0.0 ± 2.6	1.1 ± 0.8	57.3 ± 21.2
	L	2.6 ± 1.8	1.2 ± 0.9	-1.4 ± 1.8	-0.9 ± 0.7	90.9 ± 31.0
S2-Low	R	5.0 ± 3.2	2.4 ± 1.5	3.9 ± 4.9	-0.1 ± 2.5	23.6 ± 9.7
	L	8.5 ± 4.0	2.4 ± 1.5	8.5 ± 1.9	0.9 ± 1.2	-40.4 ± 12.7
S3-High	R	1.5 ± 0.9	4.7 ± 0.9	-1.0 ± 1.2	-4.7 ± 1.9	16.9 ± 6.0
	L	3.8 ± 2.1	3.8 ± 1.9	3.7 ± 3.5	-3.7 ± 3.4	14.1 ± 4.9
S3-Low	R	8.2 ± 1.5	3.9 ± 1.5	-8.3 ± 1.4	-4.0 ± 1.9	30.0 ± 11.4
	L	2.5 ± 1.8	4.4 ± 3.3	-1.7 ± 2.7	-4.1 ± 3.9	39.6 ± 15.6
Mean(S1-S3)		4.2	2.7	-0.7	-1.7	34.6
STD[3](S1-S3)		2.2	1.5	2.2	1.7	14.3

* Reported as mean $\pm$ standard deviation (STD).
[1] Moving window is selected for each participant based on his/her step length. For the three participants, the moving window is selected within the range of 1.7-2.3 seconds for high speed walking and 2.7-3.6 seconds for low speed walking.
[2] Averages evaluated over the gait cycle. The gait cycle starts with heel strike in the right leg.
[3] Reports the mean over the standard deviations.

tion inputs u_m for both legs are displayed at the top, whereas the electric motor input commands u_e are depicted at the bottom. The muscle input switching is observed through the activation of hams and quads to achieve flexion and extension, respectively. Similarly, the motor commands are switching between the upper layer command u_m and the lower layer control commands u_{fl} and u_{ex} designed in Chapter 3.

The stiffness tracking errors for the left and right knee joints are presented in Figure 4.6. The stiffness errors in Figure 4.6 are quantified using a moving time interval window of 1.99 seconds, which is selected based on the walking speed and step length of the participant. Both integral stiffness error signals remain bounded during the experiment. Figure 4.7 depicts the computed foot trajectories in the sagittal plane for the two gait speeds, which further illustrates the influence of the developed controllers and gait speed on the participant's walking pattern.

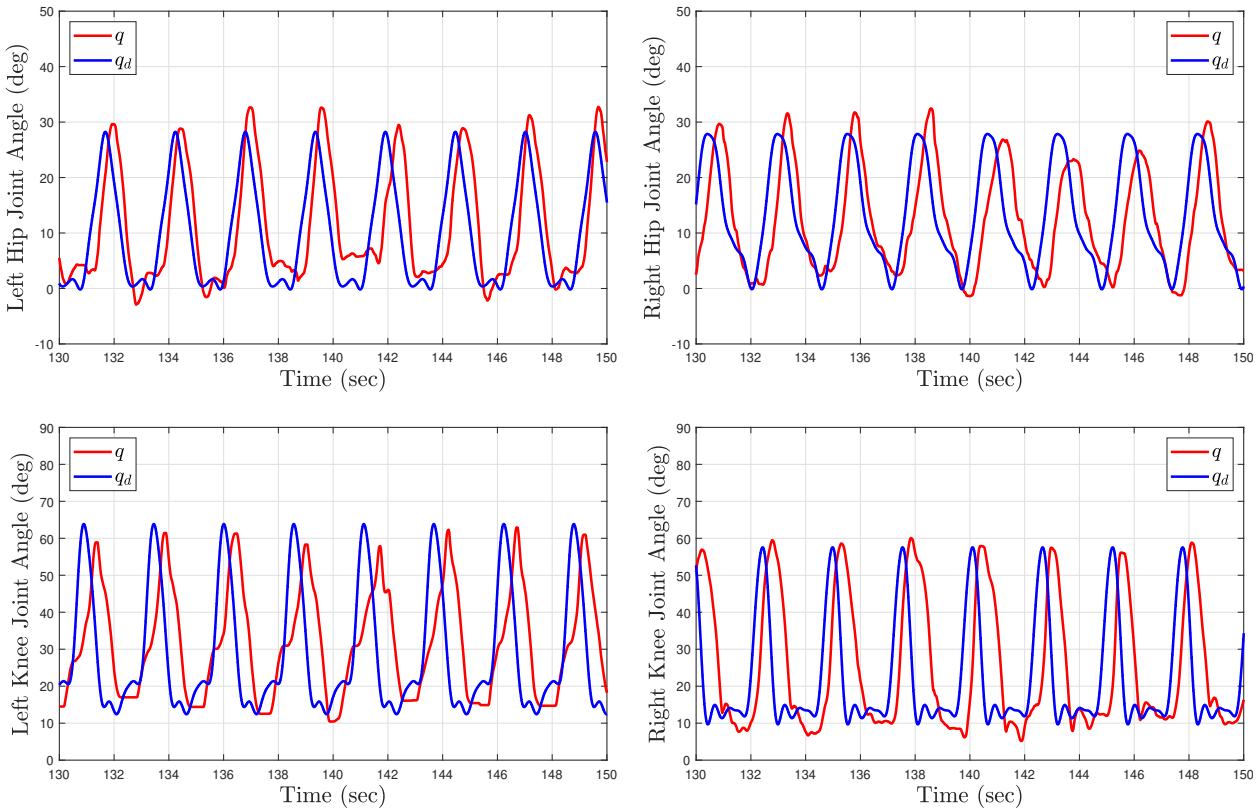

Figure 4.2: Kinematic tracking performance for Subject 2 (S2) after two minutes of treadmill walking at high speed (0.8 mph). The top plots depict the left and right hip joint kinematics. The bottom plots depict the left and right knee joint kinematics. The blue curves illustrate the desired kinematic trajectories and the red curves show the actual joint angles.

4.4 Discussion

The experimental results demonstrate the feasibility of the controllers developed in (4.8) and (4.15) to activate lower-limbs muscles via FES and provide torque assistance about the knee and hip joints. The designed controllers exploited kinematic and torque feedback to achieve treadmill walking at a constant speed. By adjusting the tuning of the stiffness controller the exoskeleton provides higher or lower leg compliance, which directly influences the joint kinematics. In addition, adjusting the tuning of the muscle kinematic controllers can customize the stimulation intensities applied to the quadriceps and hamstrings muscle groups. Therefore, coupling kinematic and stiffness controllers for FES and electric motors can influence each individual's gait kinematics and foot trajectories across different walking speeds as illustrated in Figure 4.4 and Fig-

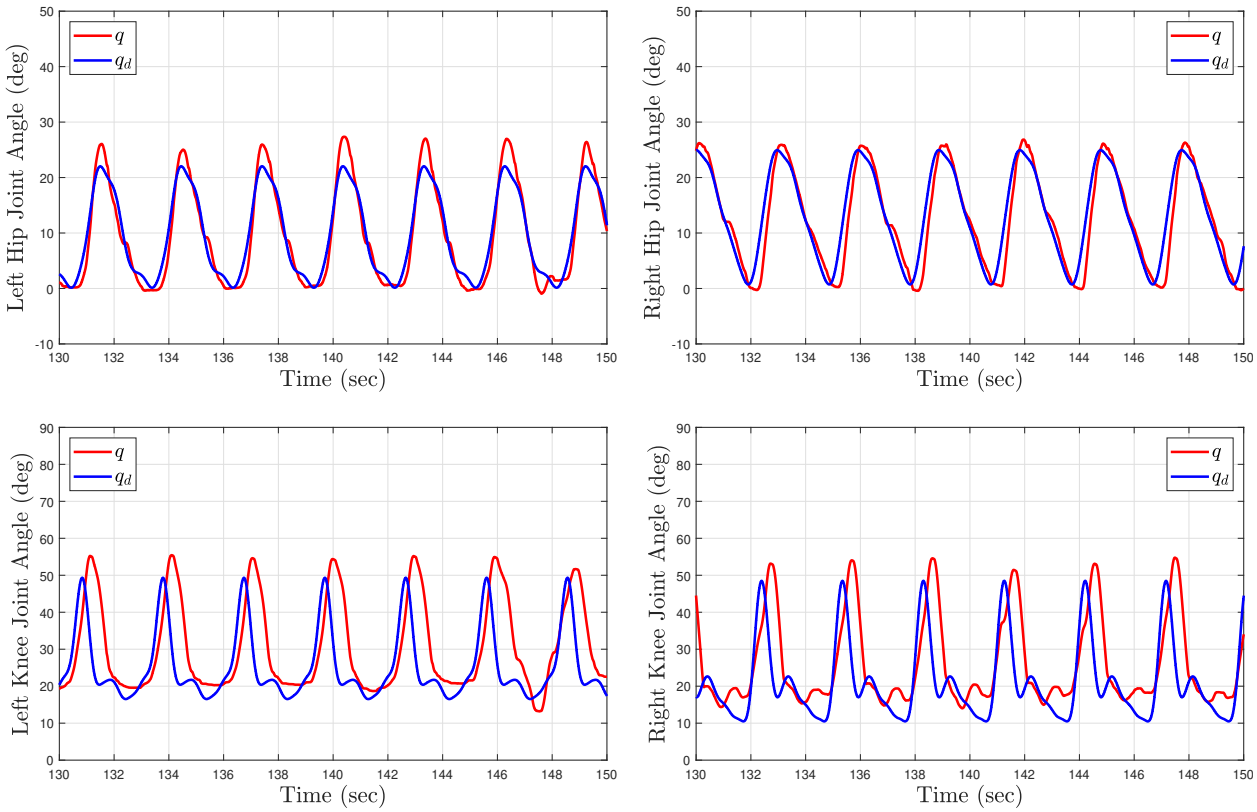

Figure 4.3: Kinematic tracking performance for Subject 1 (S1) after two minutes of treadmill walking at low speed (0.5 mph). The top plots depict the left and right hip joint kinematics. The bottom plots depict the left and right knee joint kinematics. The blue curves illustrate the desired kinematic trajectories and the red curves show the actual joint angles.

ure 4.7. As depicted in Figure 4.4, the developed controllers achieved repeatable and consistent kinematic joint trajectories as a function of the gait cycle for participant S1. Moreover, consistent joint kinematic patterns were obtained across all participants for both walking speeds, which are described with a group average of the joint angle standard deviations: ± 5.85 degrees for the right knee, ± 5.03 degrees for the right hip, ± 8.57 degrees for the left knee, and ± 5.88 degrees for the left hip. Similarly, Figure 4.7 denotes the foot trajectories in the sagittal plane, which are computed based on joint kinematics. The foot path is another indirect metric of gait consistency, which could be further used to quantify human performance or design alternate control methods. The integration of FES and cable-driven exoskeletons holds the potential to customize the human interaction to restore or improve function in individuals with movement disorders by achieving repetitive and coordinated walking.

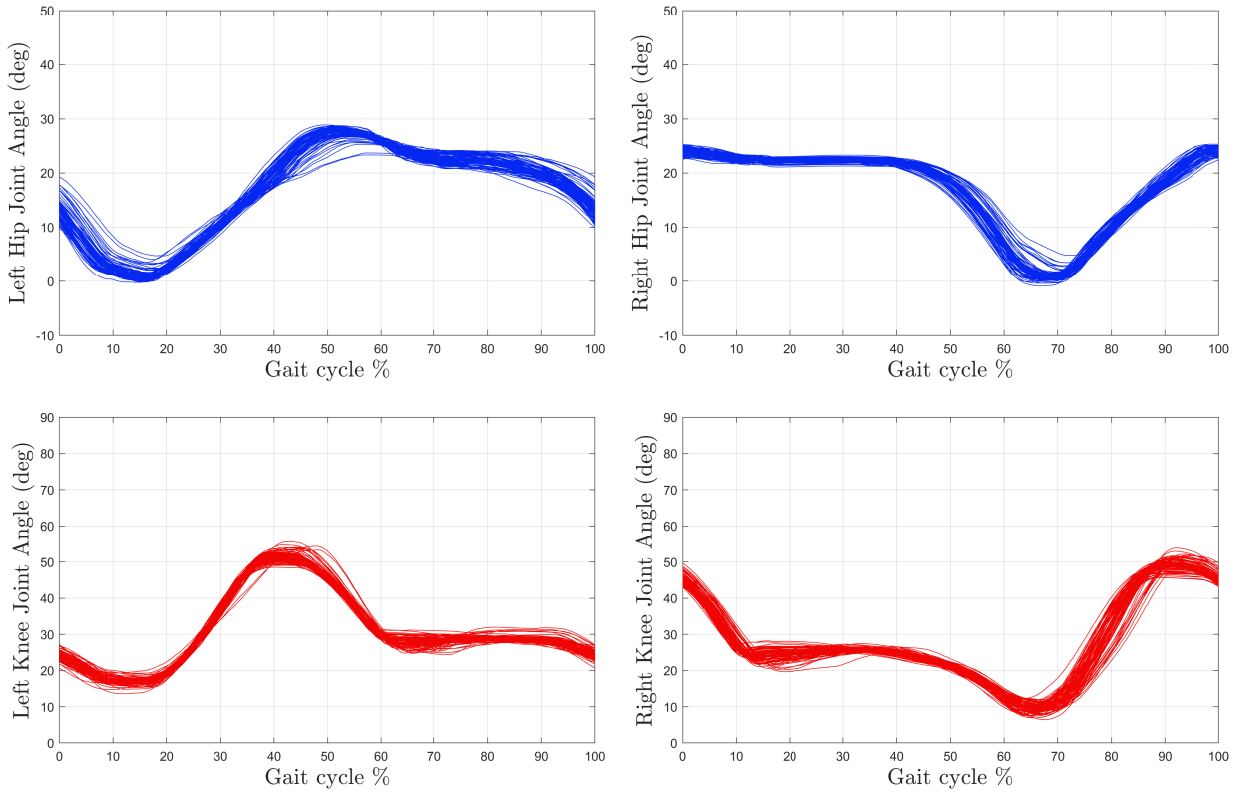

Figure 4.4: The kinematic joint trajectories corresponding to each gait cycle during the treadmill walking experiment at high speed (0.8 mph) for Subject 1 (S1).

The results in this study align qualitatively with previously published results for exoskeletons that include FES to activate lower-limb muscles. However, the differences in the control designs and experimental test beds pose challenges to directly compare the obtained results in this study with previous studies on hybrid exoskeletons. In [16], [37] a hybrid neuroprosthesis (i.e., a powered exoskeleton with surface FES) was tested in one able-bodied individual and one participant with SCI. The performance of the designed muscle and motor controllers was demonstrated during overground walking assisted by a walker. In [15], a cooperative control approach was used to iteratively compute the muscle stimulations during walking assisted by an exoskeleton in individuals with SCI. Despite the advances in hybrid approaches to enable assisted walking in individuals with paralysis for function restoration, technical innovations are still needed to achieve speeds and distances for walking in the community [20].

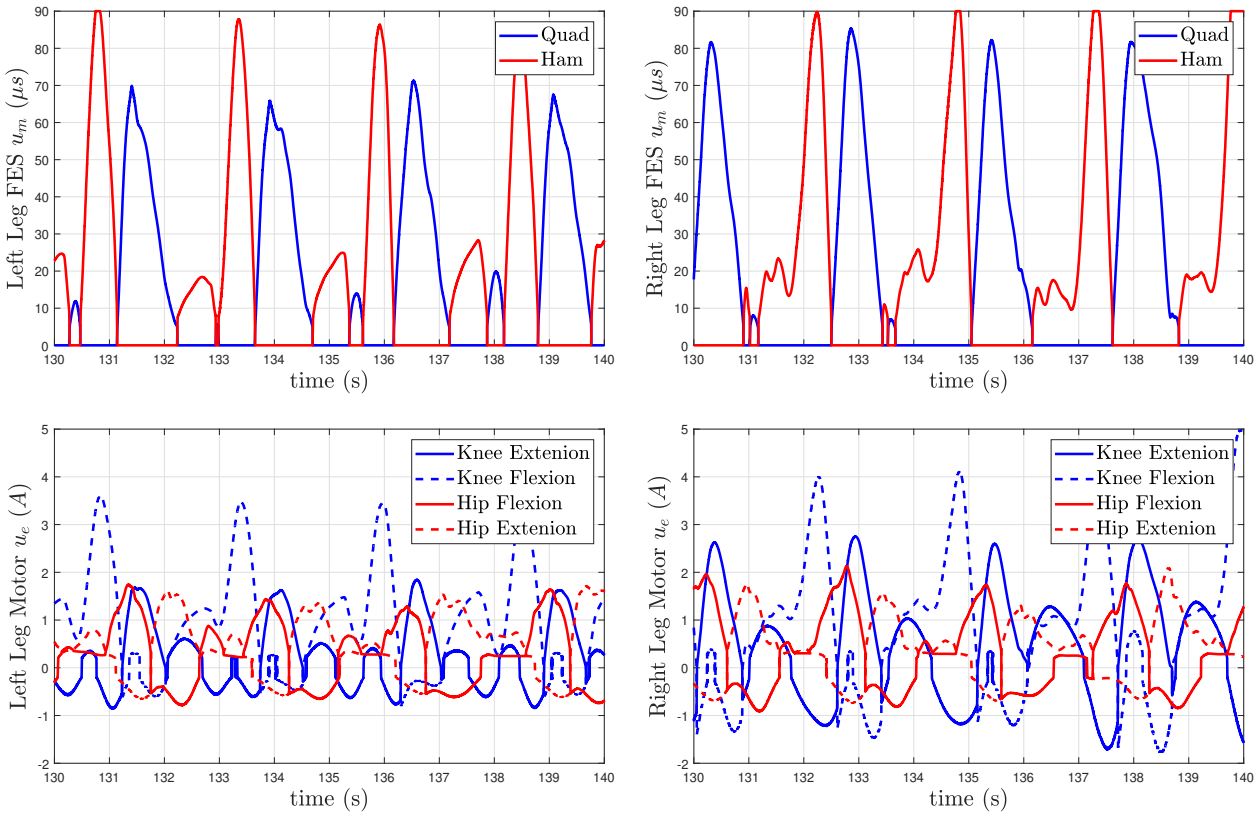

Figure 4.5: Distribution of the muscle and motor control inputs for Subject 2 (S2) during the high speed walking trial (0.8 mph). The top plots depict the pulse widths generated by u_m and applied to the quadriceps and hamstrings muscle groups for the left and right legs after two minutes of treadmill walking. The bottom plots show the motor currents generated by u_e and applied to the motors that actuate the knee and hip joints of the left and right legs.

The joint tracking performance is influenced by the implementation of the controllers and the unique characteristic of each individual. The hip joint kinematic tracking objective was achieved by the electric motors. Improved hip kinematic performance was obtained compared to the knee joint kinematic tracking as depicted in Figure 4.3 for S2 and reported in Table 4.1 across both treadmill walking speeds. Alternatively, the knee joint kinematic tracking objective was achieved by the activation of muscles via FES. Despite achieving the desired range of motion, the knee joint tracking performance was negatively influenced by the muscle activation input delay across all participants (as discussed in more detail in the subsequent paragraph). The electric motors controlled the stiffness objective in the knee joint to adjust the cable tensions and provide a smooth interaction for the shank throughout the gait cycle. An alternate approach could be for the mus-

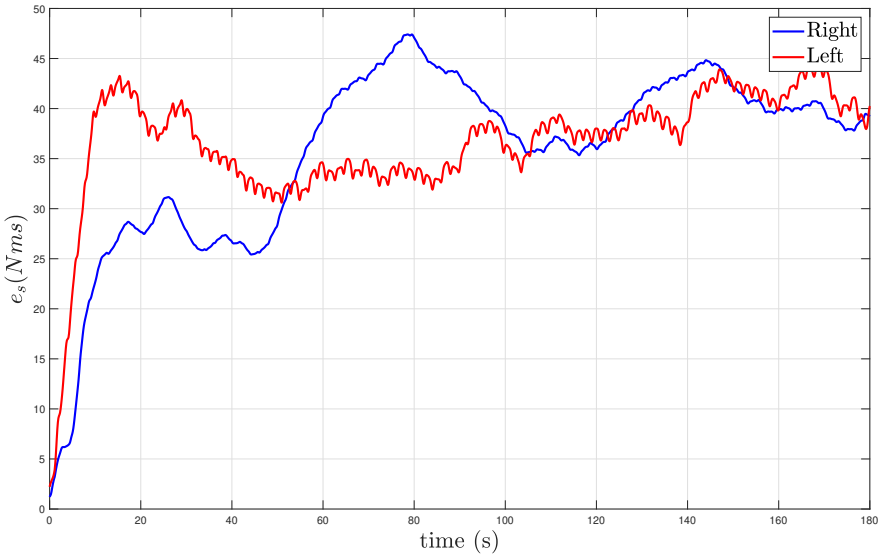

Figure 4.6: Stiffness tracking performance during treadmill walking at high gait speed (0.8 mph) for Subject 1 (S1). The stiffness tracking performance is depicted in blue and red for the right and left knee joints, respectively. The data is presented with a moving time interval window of 1.99 seconds, which is the time in seconds to complete a gait cycle.

cles and electric motors to cooperate to achieve improved knee joint tracking performance. However, the cooperative control of muscles and motors has to be carefully selected to avoid the exoskeleton dominating the human output and thus resulting in passive walking [1].

Despite the fact that the stability analysis for the kinematic and stiffness controllers yields an exponential tracking result, there are inherent factors in the dynamics that influence the walking performance. Hence, the implementation of the treadmill-based walking experiments experience several challenges. The active torque generated by the muscle contractions is influenced by the electromechanical delay (EMD) inherent in the muscle activation dynamics, which degrades joint tracking performance. As depicted in Figure 4.2 and Figure 4.3, there exists a muscle contraction delay (i.e., a time difference between the onset of the stimulation and the point when the participant's muscle force is effectively evoking active force) that affects the response of the muscle during tracking. In practice, input delay influences not only the muscle generated torque but also the response of the electric motors and cable-driven mechanisms. The muscle stimulation response time is within approximately 100-300 ms [86], which influences the walk-

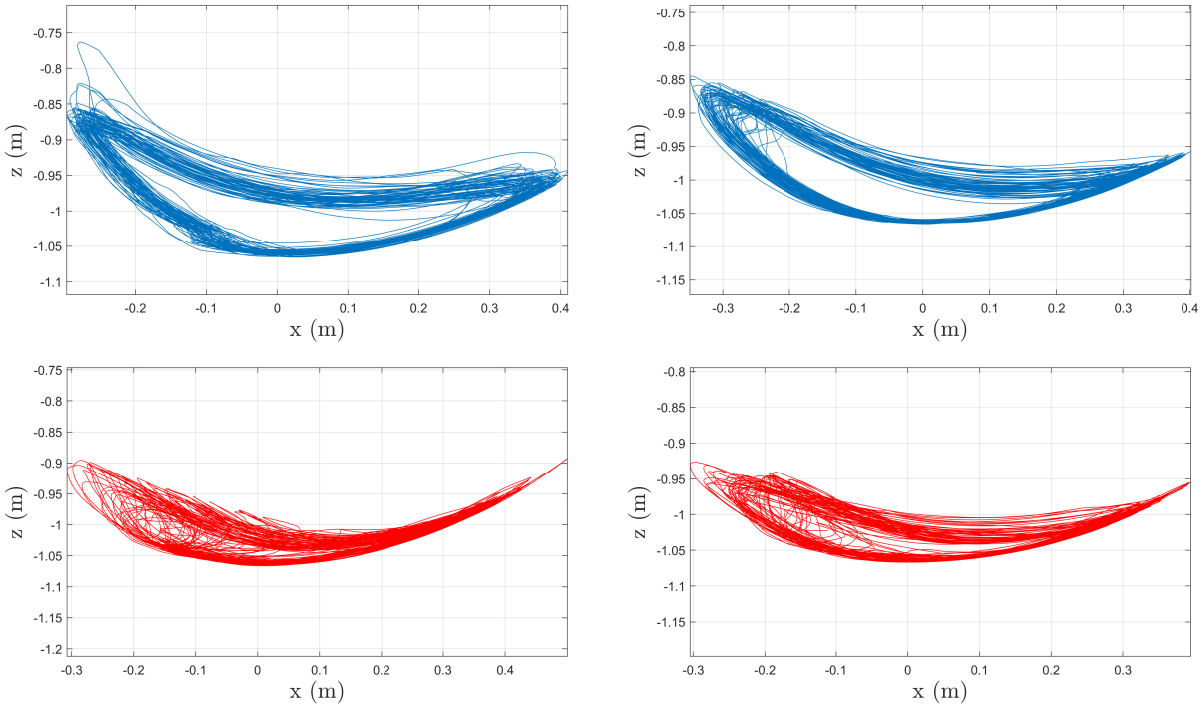

Figure 4.7: Foot trajectories in the sagittal plane (i.e., the foot path in the x-z plane) at high(top) and slow (bottom) speeds for Subject 2 (S2). The plots in the left column correspond to the left leg and plots in the right column correspond to the right leg. The trajectories are computed using collected joint angles, where the origin corresponds to the trunk position.

ing tracking performance especially for faster treadmill speeds. Further in [86], it was concluded for the quadriceps that the EMD increases as the number of muscle contraction increases under isometric conditions. A systematic way to compensate for muscle input delay is to design an input delay compensator to inject a delay-free input in the closed-loop controller, as in previous results [37]. However, a control design to compensate for input delay raises technical challenges to analyze the stability of switched delayed systems, which is a control problem beyond the scope of this dissertation. Moreover, an estimate of the input delay is likely needed for the effective implementation of the delay-free controller. Muscles experience fatigue that can lead to loss of performance. Similarly to compensating for input delay, the control design can be enhanced to cope with fatigue [37]. Muscle fatigue did not play a major role during the obtained three-minute walking experiments in able-bodied individuals. However, muscle fatigue compensation is needed for individuals with movement disorders who need a high dosage of locomotion

training. Asynchronous stimulation patterns such as the ones developed in [87] can be implemented for assisted walking to lessen the effects of fatigue. Hence, muscle fatigue and delay are important factors to consider for the development of rehabilitative strategies using FES. Moreover, the measurement of the torque about the knee joint using load cells can be prone to noise, which directly affects the quality of the torque tracking objective. Subsequent efforts are directed to improve the force signal quality for the designed torque-based controllers.

From a control perspective, technical improvements in the control design for the muscles and electric motors in the hybrid exoskeleton will be explored. The motivation behind the sliding-mode control terms in (4.8) and (4.15) is to compensate for the upper bounds on disturbances and uncertain nonlinearities in the dynamics model and analytically guarantee exponential tracking using a switched system analysis. However, robust control methods exploiting high frequency and high gain can accelerate the onset of muscle fatigue and potentially induce chattering effects. Alternatives to sliding-mode control include using higher-order sliding mode or a continuous version of the sliding-mode controller (e.g., high-slope saturation function using a boundary layer as in [88]). Therefore, adaptive control methods are desirable to cope with uncertainty through estimation of parametric and non-parametric uncertainty and improve tracking performance, while reducing the need for high-frequency content feedback. The design and stability analysis associated with adaptive control strategies are to be examined in subsequent efforts. Motivation also exists to improve the design of torque tracking controllers. The stiffness tracking controller in (4.15) uses an auxiliary integral signal of the torque feedback in (4.13). Thus, the knee stiffness controller acts as an integral controller, which does not responds instantaneously yet remains bounded as depicted in Figure 4.6. Despite the slower response of the stiffness integral controller, higher order derivatives of the torque feedback signal are not required for the control design and stability analysis. In fact, the derivative of the torque signal is usually not available for feedback due to noise. Another important control challenge when developing kinematic and stiffness controllers for muscles and motors is their ongoing dynamic interaction during experiments, which raises the need to guarantee stability of both closed-loop error systems. The ap-

proach in this chapter is to compensate for the interaction terms using a robust approach. Alternatively, exploring passivity methods [88] or energy shaping [89] can lead to novel control designs for assisted walking using hybrid exoskeletons. Finally, the desired joint kinematics in this study were generated by exploiting preliminary data collected for each participant. The study of how to optimize the kinematic gait pattern using trajectory optimization methods as in [90], [91] are to be explored to customize the trajectories for each individual. Moreover, the developed control methods need to be expanded to account for tracking objectives that do not depend on time but rather on gait phase or a phase-dependent variable [89]. Time dependent trajectories might not be suitable for walking training of individuals who can apply volition (e.g., stroke survivors) or for locomotion in unstructured environments outside of the laboratory.

The walking performance obtained for the three able-bodied individuals motivates the evaluation of the developed control approach in individuals with different levels of mobility (i.e., participants who require different assistance levels). The integration of lighter devices that minimize resistance with control technology that promotes user's volition is desired to maximize human effort and intent in individuals with incomplete SCI and stroke survivors. It is expected that individuals with SCI could benefit from continuous stepping training at high intensities for a long duration across multiple gait sessions [1].

4.5 Concluding Remarks

Hybrid exoskeletons combine motorized assistance and FES to exploit the benefits of activating paralyzed muscles and the torque reliability of the machine. Kinematic and stiffness tracking controllers were designed and implemented to actuate electric motors and activate lower-limb muscles to achieve treadmill walking at a constant speed. Two walking trials at different speeds were conducted for each of the three participants. A bipedal walking model for the exoskeleton and human is developed using a switched systems approach that captures the transitions for

stance to swing phase, and vice versa. For the knee joint, the muscles achieved kinematic tracking and the electric motor achieved the stiffness control objective by adjusting the cable tensions. For the hip joint, the electric motors achieve the kinematic tracking objective. A Lyapunov-based stability analysis is developed to yield exponential tracking for both the kinematic and stiffness closed-loop systems. The results obtained in the able-bodied individuals demonstrate the ability of the muscle and exoskeleton controllers to yield predictable, repetitive assisted walking on a treadmill and motivates subsequent evaluation in people with NCs.

4.6 Appendix

Guidelines for Tuning the Control Gains

Hybrid exoskeletons integrate powered mechanisms and FES to provide assistance and activate muscles during rehabilitative walking. Hybrid exoskeletons aim to improve walking ability and build muscle capacity in individuals with movement deficits. However, the human-exoskeleton dynamics are nonlinear, uncertain and time-varying, which pose technical and practical challenges. Closed-loop controllers are designed in (4.8) and (4.15) to overcome these challenges and achieve treadmill walking using the hybrid exoskeleton. To implement the developed controllers in real-time experiments, the practitioner selects control gains that influence the inputs applied to the electric motors and muscles via FES. The goal is to adjust the control gains to achieve satisfactory muscle response despite the nonlinear activation rate and time-varying dynamics. The control gains are adjusted for the electric motors to achieve a fast electro-mechanical response without inducing high transients, which can negatively affect the human-robot interaction in particular for individuals with neurological conditions. The control gains introduced in (4.8) and (4.15) were tuned during a preliminary trial prior to the actual treadmill walking experiment. During the pretrial for gain tuning, the kinematic controller in (4.8) was turned on first, which

activates the electric motors that actuate the hip joints and the quadriceps and hamstrings muscle groups. Once satisfactory performance was obtained for the hip and knee kinematic controllers, then the knee stiffness controller was turned on to adjust the response of the electric motors that actuate the knee joint. Additional tuning steps were conducted when both kinematic and stiffness controllers were activated. The selection of the control gains in (4.4), (4.8), (4.15), (4.17), and (4.18) is described below.

- α: This gain in (4.4) adjusts the kinematic controller proportionally to the hip and knee joint angle error. The gain α influences the response of the electric motors that actuate the hip joint and the muscles that generate torque about the knee joint. The gain α was selected largest among all the control gains to bias the tuning of the control gains towards improving the joint angle kinematic tracking.

- k_1: This gain in (4.8) adjusts the kinematic controller by weighting the joint angular position error e_κ and angular velocity error $\dot{e}_\kappa$. This gain influences the hip joint electric motors and muscles. This gain was tuned to achieve satisfactory response of the derivative term (i.e., angular velocity) to reach the desired kinematic range of motion.

- $k_2 - k_5$: These gains in (4.8) adjust the kinematic controller by weighing the signum function $\text{sgn}(r_\kappa)$. The gain k_2 compensates for the constant upper bound in (4.7), thus acts as an offset that changes sign. The gain k_3 weighs the norm of the composite error vector z_κ, thus acts as a linear term. The gain k_4 weighs the norm squared of z_κ. The gain k_5 weighs the norm of the stiffness input, which acts as a cross-term. These control gains are tuned lower compared to the gains α, k_1 since their values can amplify nonlinearities and yield chattering effects. As a rule of thumb, $k_2 \geq k_3 \geq k_4$ since they act as constant, linear, and quadratic terms.

- k_6: This gain in (4.15) adjusts proportionally the knee stiffness controller by weighing the integral torque error e_s. This gain influences the knee joint electric motors. The gain

is tuned to balance the stiffness response to prevent a bias to overshoot or undershoot the desired stiffness trajectory.

- $k_7 - k_8$: These control gains in (4.15) adjust the knee stiffness controller by weighing the signum function sgn(e_s). The gain k_7 weighs the knee kinematic tracking error, thus acts as a proportional term. The gain k_8 weighs the norm of the knee joint kinematic input, which acts as a cross term. These control gains are tuned to reduce the potential chattering effects using force feedback.

- k_e: This scaling gain in (4.17) adjusts the control command for each electric motor. The gain weighs both the hip kinematic controller and knee stiffness controller.

- k_m: This scaling gain in (4.18) adjusts the control commands for each muscle (i.e., right and left quadriceps and hamstrings). The gain was increased or decreased to compensate for weaker or stronger muscle responses across the three participants to achieve joint kinematic tracking. In addition, stimulation sensitivity or discomfort was a factor in tuning the muscle gains $k_m, \forall \mathcal{M}$.

Chapter 5

Motorized FES-Cycling and Closed-Loop Nonlinear Control for Power Tracking using a Finite-Time Stable Torque Algorithm

In this chapter, cadence and torque controllers are designed for power tracking using the motorized FES-cycling system with dynamics introduced in Chapter 2. To capture the time-varying muscle capacity to evoke active torque, a finite-time torque control algorithm is developed to adjust the desired torque in real-time by leveraging estimates of the active torque produced by muscles. The finite-time torque controller leverages input-output data of the active torque produced by muscles due the applied FES input to update the peak torque desired per crank cycle. This torque strategy departs from existing cycling studies that implement predetermined desired torque trajectories that can yield degraded cycling performance as the rider fatigues. A robust sliding mode controller is designed for the electric motor to track a desired constant cadence trajectory. Moreover, an integral torque feedback controller is designed to activate muscle groups to track

the desired torque trajectory computed by the finite-time algorithm. A Lyapunov-based stability analysis is developed to ensure exponential cadence tracking and a global uniformly ultimate bounded (GUUB) result for torque tracking. A discrete-time Lyapunov-based analysis is used to ensure the finite-time torque controller that generates the desired trajectory is Hölder continuous. Experimental results in seven able-bodied individuals are presented to examine the feasibility of the developed control methods. Multiple cycling trials are implemented with different gain parameters of the finite-time torque algorithm to compare tracking performance for all participants.

5.1 Control Development

The control design is segregated into cadence tracking control objective, finite-time control algorithm to generate the desired torque trajectory, and torque tracking control objective. The first objective is to design a cadence controller for the electric motor to track a desired constant cadence trajectory. The second objective is to design a discrete-time finite-time controller that generates the target amplitude for the desired torque trajectory. The last objective is to design a torque controller for the muscles via FES to track the desired torque trajectory.

5.1.1 Cadence Tracking Control

The measurable angular position tracking error $e : \mathbb{R}_{\geq t_0} \to \mathbb{R}$ and filtered tracking error $r : \mathbb{R}_{\geq t_0} \to \mathbb{R}$ are defined as

$$e(t) \triangleq q_d(t) - q(t), \tag{5.1}$$

$$r(t) \triangleq \dot{e}(t) + \alpha e(t), \tag{5.2}$$

where $\alpha \in \mathbb{R}_{>0}$ is a selectable positive control gain and $q_d, \dot{q}_d, \ddot{q}_d : \mathbb{R}_{\geq t_0} \to \mathbb{R}$ are bounded desired crank trajectories. For simplicity of notation, the explicit dependence of time, t, is hereafter suppressed unless required for clarity of exposition. After taking the time derivative of (5.2), pre-multiplying by M, substituting for (2.6), (2.11) and (5.1), and performing some algebraic manipulation yields

$$M\dot{r} = \chi - B_e u_e - \tau_m - e - Cr, \tag{5.3}$$

where the auxiliary signal $\chi : \mathbb{R}_{\geq t_0} \to \mathbb{R}$ is defined as

$$\chi \triangleq M(\ddot{q}_d + \alpha\dot{e}) + C(\dot{q}_d + \alpha e) + G + P + d + e. \tag{5.4}$$

The upper bound for the auxiliary signal in (5.4) can be obtained by using Properties 9-12, Assumption 8 as

$$\chi \leq c_1 + c_2 \|z\| + c_3 \|z\|^2, \tag{5.5}$$

where $c_1, c_2, c_3 \in \mathbb{R}_{>0}$ are positive constants and the composite error signal $z : \mathbb{R}_{\geq t_0} \to \mathbb{R}^2$ is defined as

$$z \triangleq \begin{bmatrix} e & r \end{bmatrix}^T. \tag{5.6}$$

Given the open-loop error system in (5.3), the cadence control input for the electric motor u_e can be designed as

$$u_e = k_1 r + \left(k_2 + k_3 \|z\| + k_4 \|z\|^2 + k_5 |u_m|\right) \text{sgn}(r), \tag{5.7}$$

where $k_1, k_2, k_3, k_4, k_5 \in \mathbb{R}_{>0}$ are positive control gains, and the signum function is $\text{sgn}(\cdot) : \mathbb{R} \to [-1, 1]$. The cadence control input in (5.7) includes a feedback term and robust control terms to reject the auxiliary signal in (5.4) and compensate for the muscle torque cross-term. The closed-loop error system can be obtained by substituting the control input (5.7) into the open-loop error system in (5.3) as

$$M\dot{r} = \chi - e - Cr - \tau_m - B_e \left(k_1 r + \left(k_2 + k_3 \|z\| + k_4 \|z\|^2 + k_5 |u_m|\right) \text{sgn}(r)\right). \tag{5.8}$$

5.1.2 Finite-time Control

The purpose of the finite-time controller is to compute the target amplitude of the desired torque trajectory. The implementation of arbitrary or predetermined torque trajectories is susceptible to yield suboptimal cycling performance since the rider's capacity is uncertain and time-varying (e.g., after a neurological disorder, people retain different levels of residual function). In addition due to the FES-induced muscle fatigue, motivation exists to update the desired torque amplitude each cycle and eliminate the need to perform manual adjustments. The discrete finite-time controller is designed as follows.

The desired torque trajectory $\tau_d : \mathbb{R}_{\geq t_0} \times \mathbb{R} \to \mathbb{R}$ is designed as

$$\tau_d(t, q) = A(t_i) f(q), \tag{5.9}$$

where $t_i \in \mathbb{R}_{\geq t_0}, i \in \mathbb{N}$ denotes the i^{th} time the crank passes $q = 0°$ (i.e., crank cycle index), $A : \mathbb{R}_{\geq t_0} \to \mathbb{R}$ denotes the amplitude of the desired torque trajectory, and $f : \mathcal{Q} \to \mathbb{R}$ is a normalized bounded profile of the desired torque that depends on the crank angle. The initial amplitude $A(t_0)$ for the desired torque is selected as a positive constant, hence τ_d is guaranteed to be bounded during the first cycle. The desired torque estimation error $e_f : \mathbb{R}_{\geq t_0} \to \mathbb{R}$ can be defined as

$$e_f(t_i) \triangleq A(t_i) - \tau_{peak}(t_i), \tag{5.10}$$

where τ_{peak} is the measurable peak active torque generated by muscles during the last crank cycle and defined as

$$\tau_{peak}(t_i) \triangleq \max\left(\hat{\tau}_m(t)\right), \forall t \in [t_{i-1}, t_i), \tag{5.11}$$

where the estimate of the active torque $\hat{\tau}_m$ is obtained using (2.9).

Taking the forward difference of (5.10) (i.e., $\Delta\Omega(t_i) \triangleq \Omega(t_{i+1}) - \Omega(t_i)$) yields

$$\Delta e_f(t_i) = \Delta A(t_i) - \Delta\tau_{peak}(t_i). \tag{5.12}$$

Based on the stability analysis in Section 5.2.2, the update law to generate the torque amplitude is designed as

$$\Delta A(t_i) = \left(\mathcal{D}\left(e_f(t_i)\right) - 1\right) e_f(t_i) + \Delta\tau_{peak}(t_i), \tag{5.13}$$

where $\mathcal{D} : \mathbb{R}_{\geq t_0} \to \mathbb{R}$ is defined as in [74]

$$\mathcal{D}\left(e_f(t_i)\right) = \frac{\left(e_f^2\right)^{\beta} - \lambda}{\left(e_f^2\right)^{\beta} + \lambda}, \tag{5.14}$$

$\beta \in (0, 1)$, and $\lambda \in \mathbb{R}_{>0}$ is a selectable positive constant. Substituting (5.13) and (5.14) into (5.12) and performing some algebraic manipulations yields the closed-loop torque amplitude error system

$$\Delta e_f = \frac{-\lambda\left(\mathcal{D}\left(e_f\right) + 1\right) e_f}{\left(e_f^2\right)^{\beta}}. \tag{5.15}$$

5.1.3 Torque Control Tracking

The purpose of the torque controller is to track the desired torque trajectory in the FES-regions as depicted in Figure 2.4. To quantify the torque control objective, an integral-like error signal $e_\tau : \mathbb{R}_{\geq t_0} \to \mathbb{R}$ can be defined as

$$e_\tau(t) = \int_{t_0}^{t} \left(\tau_d(\phi) - \hat{\tau}_m(\phi)\right) d\phi, \tag{5.16}$$

where τ_d is the desired torque trajectory defined in (5.9). Taking the time derivative of (5.16), setting the initial conditions to zero, and substituting for (2.7) and (2.10) yields

$$\dot{e}_\tau = \tau_d - B_m u_m + \epsilon. \tag{5.17}$$

The muscle control input can be designed as

$$u_m = k_6 e_\tau + k_7 \text{sgn}(e_\tau), \tag{5.18}$$

where $k_6, k_7 \in \mathbb{R}_{>0}$ are selectable positive control gains. The closed-loop torque error system can be obtained by substituting (5.18) into (5.17) as

$$\dot{e}_\tau = \tau_d - B_m \left(k_6 e_\tau + k_7 \text{sgn}(e_\tau)\right) + \epsilon. \tag{5.19}$$

5.2 Stability Analysis

The stability of cadence and torque tracking controllers that activate the electric motor and apply FES to muscles, respectively, can be examined independently. Theorem 5.2.1 shows that given the closed-loop cadence error system in (5.8), the cadence controller in (5.7) achieves exponential tracking. Theorem 5.2.2 shows that the closed-loop error system in (5.15) using the discrete finite-time controller in (5.13) is stable and Hölder continuous in discrete time. Theorem 5.2.3 shows that given the closed-loop torque error system in (5.19), the torque controller in (5.18) achieves global uniformly ultimate bounded (GUUB) tracking.

5.2.1 Cadence Tracking

Theorem 7. *Given the closed-loop error system in (5.8), the controller in (5.7) ensures exponential tracking in the sense that*

$$\|z(t)\| \leq \sqrt{\frac{\lambda_2}{\lambda_1}} \|z(t_0)\| \exp\left(-\frac{\psi}{2}(t-t_0)\right), \tag{5.20}$$

provided the following sufficient gain conditions are satisfied

$$k_2 \geq \frac{c_1}{\underline{B}_e}, k_3 \geq \frac{c_2}{\underline{B}_e}, k_4 \geq \frac{c_3}{\underline{B}_e}, k_5 \geq \frac{\overline{B}_m}{\underline{B}_e}. \tag{5.21}$$

Proof. Let $V : \mathbb{R} \times \mathbb{R} \times \mathbb{R}_{\geq t_0} \to \mathbb{R}_{\geq 0}$ be a nonnegative, continuously differentiable function defined as

$$V = \frac{1}{2}e^2 + \frac{1}{2}Mr^2, \tag{5.22}$$

which satisfies the following inequalities

$$\lambda_1 \|z\|^2 \leq V(z,t) \leq \lambda_2 \|z\|^2, \tag{5.23}$$

where $\lambda_1, \lambda_2 \in \mathbb{R}_{>0}$ are known positive bounding constants, and z is defined as in (5.6). The control input in (5.7) has the discontinuous signum function (i.e., sliding-mode); hence, the system's trajectories cannot be solved in a classical sense. Let $z(t)$ be a Filippov solution to the differential inclusion $\dot{z} \in \mathcal{K}[h](z)$, where $\mathcal{K}[\cdot]$ is defined as [82] and h is defined using (5.2) and (5.8) as $h \triangleq \begin{bmatrix} h_1 & h_2 \end{bmatrix}$, where $h_1 \triangleq r - \alpha e$ and $h_2 \triangleq \chi - e - Cr - \tau_m - B_e \left(k_1 r + \left(k_2 + k_3 \|z\| + k_4 \|z\|^2 + k_5 |u_m|\right) \mathcal{K}[\text{sgn}(r)]\right)$. Hence, the time derivative of (5.22) exists almost everywhere (a.e.), i.e., for almost all time. Based on [83, Lemma 1], the time derivative of (5.22), $\dot{V}(z,t) \overset{a.e.}{\in} \dot{\tilde{V}}(z,t)$, where $\dot{\tilde{V}}$ is the generalized time derivative of (5.22) along the Filippov trajectories of $\dot{z} = h(z)$ and is defined as in [83] as $\dot{\tilde{V}} \triangleq \bigcap_{\xi \in \partial V} \xi^T K \begin{bmatrix} \dot{e} & \dot{r} & 1 \end{bmatrix}^T (e, r, t)$.

Since $V(z,t)$ is continuously differentiable in z, $\partial V = \{\nabla V\}$, thus $\dot{\tilde{V}} \overset{\text{a.e.}}{\subset} \begin{bmatrix} e & r \end{bmatrix} K \begin{bmatrix} \dot{e} & \dot{r} \end{bmatrix}^T$. Therefore, after taking the time derivative, the generalized time derivative of (5.22) can be expressed as $\dot{\tilde{V}} \overset{a.e.}{\subset} e\dot{e} + Mr\dot{r} + \frac{1}{2}\dot{M}r^2$. After substituting (5.1), (5.2), (5.8), cancelling common terms, and applying Property 13, the generalized time derivative of (5.22) can be expressed as

$$\dot{\tilde{V}} \overset{a.e.}{\subset} -\alpha e^2 + r\chi - r\tau_m - rB_e \left(k_1 r + \left(k_2 + k_3 \|z\| + k_4 \|z\|^2 + k_5 |u_m|\right) \mathcal{K}[\text{sgn}(r)]\right). \quad (5.24)$$

The generalized time derivative of (5.22) can be upper bounded by substituting (2.7), (5.5), and using Properties 14-15 as

$$\dot{\tilde{V}} \overset{a.e.}{\leq} -\alpha e^2 - k_1 \underline{B}_e r^2 + (c_1 - k_2 \underline{B}_e)|r| + (c_2 - k_3 \underline{B}_e)|r|\|z\| + (c_3 - k_4 \underline{B}_e)|r|\|z\|^2 + \left(\overline{B}_m - k_5 \underline{B}_e\right)|r||u_m|. \quad (5.25)$$

Provided the gain conditions in (5.21) are satisfied, the inequality in (5.25) can be further upper bounded as

$$\dot{\tilde{V}} \overset{a.e.}{\leq} -\alpha e^2 - k_1 \underline{B}_e r^2. \quad (5.26)$$

The upper bound in (5.23) can be substituted into (5.26) to yield

$$\dot{\tilde{V}} \overset{a.e.}{\leq} -\psi \tilde{V}, \quad (5.27)$$

where $\psi \triangleq \frac{1}{\lambda_2} \min(\alpha, k_1 \underline{B}_e)$. Leveraging (5.23) and (5.27), the result in (5.20) can be obtained. Using (5.22) and (5.27), $V \in \mathcal{L}_\infty$, hence, $e, r \in \mathcal{L}_\infty$, which implies that $z \in \mathcal{L}_\infty$, and thus $q, \dot{q} \in \mathcal{L}_\infty$. ■

5.2.2 Finite-time Control

Theorem 8. *Given the closed-loop error system in (5.15), the update law in (5.13) ensures (5.15) is Hölder continuous in discrete time with exponent* $\frac{1}{1-\delta}$ *in the sense that*

$$V_f(t_{i+1}) \leq (v - (i+1)\eta)^{\frac{1}{1-\delta}}, \tag{5.28}$$

where $v \in \mathbb{R}_{>0}$ *is defined as*

$$v \triangleq \frac{V_f(t_0)}{\varepsilon}, \tag{5.29}$$

and $\varepsilon, \delta, \eta \in \mathbb{R}_{>0}$ *are positive constants.*

Proof. Let $V_f : \mathbb{R} \times \mathbb{R}_{\geq t_0} \to \mathbb{R}_{\geq 0}$ be a positive definite, decrescent and radially unbounded Lyapunov function defined as

$$V_f(t_i) = \frac{1}{2} e_f^2(t_i). \tag{5.30}$$

Taking the first order forward difference (i.e., $\Delta(ab) = a\Delta b + b\Delta a$) of (5.30) yields

$$\Delta V_f(t_i) = e_f(t_i) \Delta e_f(t_i). \tag{5.31}$$

After substituting the closed-loop error system in (5.15) into (5.31), the following expression is obtained

$$\Delta V_f(t_i) = -\lambda \left(\mathcal{D}\left(e_f(t_i)\right) + 1\right) \left(e_f^2(t_i)\right)^{1-\beta}, \tag{5.32}$$

which can be further expressed as

$$V_f(t_{i+1}) - V_f(t_i) = -\gamma V_f^{\delta}(t_i), \tag{5.33}$$

where $\delta \triangleq 1 - \beta$ and $\gamma : \mathbb{R}_{\geq 0} \to \mathbb{R}_{\geq 0}$ is a positive definite function of $V_f(t_i)$ that satisfies the

condition that there exists an $\varepsilon \in \mathbb{R}_{>0}$ such that

$$\gamma(V_f(t_i)) \triangleq 2\lambda \left(\mathcal{D}\left(e_f(t_i)\right) + 1\right) \geq \eta \triangleq \varepsilon^{1-\delta}, \forall V_f(t_i) \geq \varepsilon. \tag{5.34}$$

Leveraging the result in [74] and the fact that $V_f(t_{i+1}) \leq V_f(t_i)$ from (5.33), the following inequality can be obtained to provide an upper bound for all cycles.

$$V_f(t_{i+1}) - V_f(t_0) = V_f(t_{i+1}) - V_f(t_i) + V_f(t_i) - V_f(t_{i-1}) + \cdots + V_f(t_1) - V_f(t_0) \tag{5.35}$$

$$\leq -\eta \left(V_f^{\delta}(t_i) + \cdots + V_f^{\delta}(t_0)\right) \tag{5.36}$$

$$\leq -(i+1)\eta V_f^{\delta}(t_{i+1}). \tag{5.37}$$

Re-arranging the previous inequality yields

$$V_f(t_{i+1}) \leq \left(\frac{V_f(t_0)}{V_f^{\delta}(t_{i+1})} - (i+1)\eta\right)^{\frac{1}{1-\delta}} \tag{5.38}$$

$$\leq \left(v - (i+1)\eta\right)^{\frac{1}{1-\delta}}. \tag{5.39}$$

Since $V_f \in \mathcal{L}_\infty$, $e_f \in \mathcal{L}_\infty$. Since an initial bounded desired torque amplitude $A(t_0)$ is assigned to the torque controller for the first cycle and $u_m \in \mathcal{L}_\infty$ from Theorem 5.2.3, then $\tau_{peak}, A \in \mathcal{L}_\infty$. Further, $\Delta\tau_{peak}, \Delta A \in \mathcal{L}_\infty$. ■

5.2.3 Torque Tracking

Theorem 9. *Given the closed-loop error system in (5.19), the controller in (5.18) ensures global uniformly ultimate bounded (GUUB) tracking in the sense that*

$$e_\tau(t) \leq \sqrt{e_\tau^2(t_0)e^{-\psi_\tau(t-t_0)} + \frac{2E}{\psi_\tau}\left(1 - e^{-\psi_\tau(t-t_0)}\right)}, \tag{5.40}$$

provided the following sufficient gain condition is satisfied

$$k_7 \geq \frac{\bar{\tau}_d}{\underline{B}_m}. \tag{5.41}$$

Proof. Let $V_\tau : \mathbb{R} \times \mathbb{R}_{\geq t_0} \to \mathbb{R}_{\geq 0}$ be a nonnegative, continuously differentiable function defined as

$$V_\tau = \frac{1}{2} e_\tau^2. \tag{5.42}$$

Let $e_\tau(t)$ be a Filippov solution to the differential inclusion $\dot{e}_\tau \in \mathcal{K}[h](e_\tau)$, where $\mathcal{K}[\cdot]$ is defined as [82] and $h \triangleq h_3$ is defined by using (5.19) as $h_3 \triangleq \tau_d - \mathcal{K}[B_m]\left(k_6 e_\tau + k_7 \mathcal{K}[\text{sgn}(e_\tau)]\right) + \epsilon$. The control input in (5.18) includes the discontinuous signum function and the closed-loop error system in (5.19) has the lumped switched stiffness control effectiveness. Hence, the time derivative of (5.42) exists almost everywhere (a.e.), i.e., for almost all time. After substituting for (5.19) and using similar arguments as in the proof of Theorem 5.2.1, the generalized time derivative of (5.42) can be expressed as

$$\dot{\tilde{V}}_\tau \overset{a.e.}{\subset} e_\tau \Big(\tau_d - \mathcal{K}[B_m]\left(k_6 e_\tau + k_7 \mathcal{K}[\text{sgn}(e_\tau)]\right) + \epsilon \Big). \tag{5.43}$$

An upper bound for the previous expression can be obtained by using Property 14 and substituting the upper bound of τ_d to yield

$$\dot{\tilde{V}}_s \overset{a.e.}{\leq} -\underline{B}_m k_6 e_\tau^2 + \left(\bar{\tau}_d - \underline{B}_m k_7\right)|e_\tau| + e_\tau |\epsilon|. \tag{5.44}$$

Provided the gain condition in (5.41) is satisfied, the inequality in (5.44) can be further upper bounded as

$$\dot{\tilde{V}}_\tau \overset{a.e.}{\leq} -\psi_\tau \tilde{V}_\tau + E, \tag{5.45}$$

where $\psi_\tau \triangleq \underline{B}_m k_6$ and $E \triangleq e_\tau |\epsilon|$. Using (5.42) and (5.45), $V_\tau \in \mathcal{L}_\infty$, hence, $e_\tau \in \mathcal{L}_\infty$. Thus, $u_m \in \mathcal{L}_\infty$ implies $u_e \in \mathcal{L}_\infty$. ■

5.3 Experiment Results

Experiments are provided to demonstrate the performance of the designed controllers developed in (5.7), (5.13), and (5.18). Seven able-bodied individuals (six males aged 19-29 years and one female aged 19 years) participated in the FES-cycling protocol at Syracuse University. Written informed consent was obtained from each participant, as approved by the Institutional Review Board (IRB) at Syracuse University. The participants were instructed and reminded through the cycling protocol to avoid voluntarily contributing to the pedaling task. Individuals were not informed of the desired cadence or torque trajectories. Measurements of the participant's legs were recorded to compute the switching signals for each muscle group based on the rider's kinematic effectiveness (i.e., to define the FES regions in Figure 2.4 as in [58]). The experiment setup is described in Section 2.3.2.

A pretrial was performed at the same constant cadence as in the cycling experiments to record passive torque data $\tau_{passive}$ used in (2.9) for each participant without applying FES. The desired cadence trajectory $\dot{q}_d$ smoothly approached a steady speed during a time interval of 15 seconds, $t \in [0, T_1], T_1 = 15$. During this interval, the electric motor brought the rider to the desired speed and FES was not applied to muscles. A transition time interval of 10 seconds, $t \in [T_1, T_2], T_2 = T_1 + 10$ is used to gradually integrate FES in the experiment until reaching the steady state FES regions. Within this transition interval, the FES inputs were set to $u_m = 40\mu s$ to familiarize the rider with applied FES. Finally after the transition period, the designed controllers were activated and remained active until the end of the experiment, i.e., for $t > T_2$ and $t \triangleq 180$ seconds. All cycling experiments were implemented for 3 minutes. Each participant completed 4 cycling trials to implement different combinations of the gain parameters in (5.14) and determine feasibility of the finite-time torque algorithm. The order of the cycling trials was randomized. As described in the IRB protocol, rest breaks of 10 minutes were provided in between cycling trials. The control gains introduced in (5.7), (5.13), and (5.18) were selected as follows: $k_1 = 3.5, k_2 = 0.5, k_3 = 0.01, k_4 = 0.001, k_5 = 0.01, \alpha = 0.1, \beta = \{0.1, 0.3, 0.5\}, \lambda = \{0.1, 0.3\}, k_6 \in [0.2, 0.3], k_7 \in$

$[5, 15]$. The desired torque profile $f(q)$ in (5.9) is defined as $f(q) = \frac{1}{2}\left(\sin\left(2q - \frac{\pi}{2}\right) + 1\right)$ and the initial value of the desired torque amplitude is set at $A(t_0) = 8$ Nm.

Table 5.1 summarizes the root-mean-squared (RMS) cadence error, average of the instantaneous cadence error, and average of the integral torque errors for all subjects and their corresponding gain parameters implemented in (5.14). The experimental results were analyzed starting at $t = T_2$, which is the time the system reached the desired steady-state cadence and the closed-loop muscle and motor controllers were activated. The kinematic tracking performance for participant S1 is illustrated in Figure 5.1, where the desired cadence is depicted in blue and the actual cadence is depicted in red. The torque tracking error e_τ is presented in Figure 5.2, which remains bounded during the experiment. The torque tracking performance is illustrated in Figure 5.3, where the desired torque is depicted in light blue, the estimated active torque is depicted in red, and the average estimated active torque with a moving window of 5 seconds is depicted in solid blue. The average estimated active torque illustrates the evolution of the torque produced by muscles during the experiment, which is an indirect measure of muscle fatigue (i.e., naturally the torque produced by muscles decay due to FES-induced fatigue). Figure 5.4 shows the desired torque estimation error e_f (also referred as the finite-time tracking error) across each crank cycle for different combinations of the gain parameters in (5.14). Figure 5.5 shows the electric motor input command u_e and the muscle stimulation inputs u_m for both legs in during the last 5 seconds of a cycling trial.

Friedman tests were performed at a significance level of $\alpha = 0.05$ to test for statistically significant differences in tracking performance between the four cycling trials (i.e., 4 groups) each with different gain parameters as reported in Table 5.1. The Friedman tests on the response of the four cycling trials indicated that there were no statistically significant differences in the RMS cadence error (p-value $= 0.1053$) and mean cadence tracking error (p-value $= 0.9043$). Alternatively, a Friedman test indicated that there was a statistically significant difference between the four cycling trials in the mean torque tracking error (p-value $= 0.0134$).

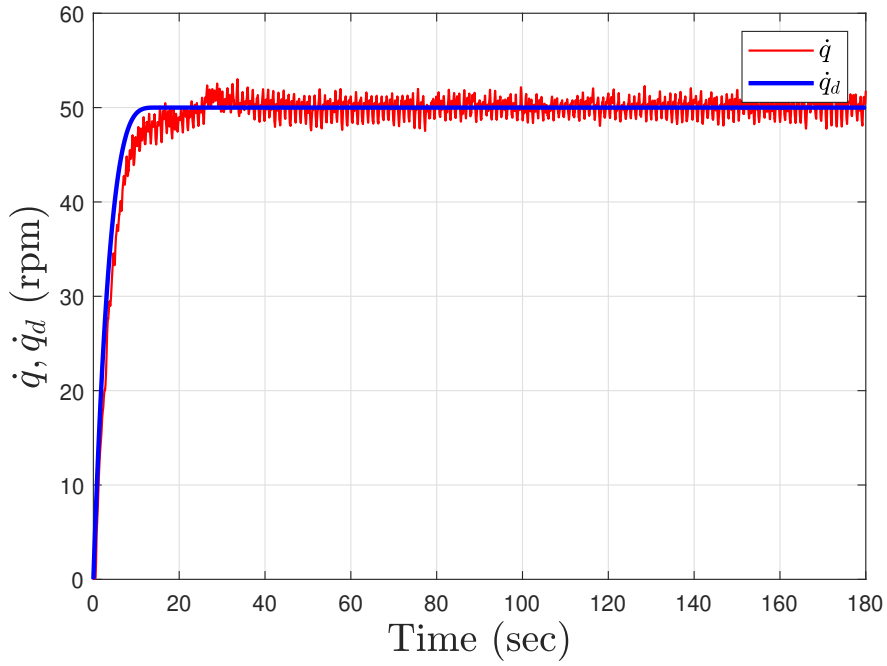

Figure 5.1: Cadence tracking performance depicted for Subject 1 (S1). The cadence trajectory smoothly approached a steady speed (50 RPM) until $t = 15$ with motor only. Then, within the interval $t = [15, 25]$, FES was integrated and set to $u_m = 40\mu s$. The closed-loop finite-time and muscle torque controllers were activated at $t = 25$ and remained active until the end of the experiment $t = 180$. The blue curve illustrates the desired cadence and the red curve shows the actual cadence. The gain parameters in (5.14) are selected as $\beta = 0.3$ and $\lambda = 0.3$.

5.4 Discussion

The experimental results demonstrate the feasibility of the developed controllers in (5.7) and (5.18) to track the desired cadence with an electric motor and torque trajectory by applying FES to activate lower limb muscles. The finite-time control algorithm developed in (5.13) and (5.14) adjusts the torque demand in real-time to cope and capture the rider's time-varying ability to generate active torque. As depicted in Figure 5.1, the developed motor cadence controller is able to maintain the rider's speed within a range of less than ± 1 RPM. In figure 5.2, the integral torque tracking error remains bounded during the cycling trial showing a feasible interaction between the desired torque demand (computed by the finite-time torque algorithm) and the active torque produced by muscles, which depicted in Figure 5.3. The developed cadence controller yields an average cadence tracking error of -0.03 ± 1.58 RPM across all participants. Cadence tracking

performance is influenced by the interaction with the muscle torque controller. Thus, the motor cadence (presented in Figure 5.5) compensates for the active torque generated by muscles, which act as a disturbance in the cadence control loop. The influence of the muscle torque into the cadence tracking objective can be quantified by the RMS cadence error included in Table 5.1.

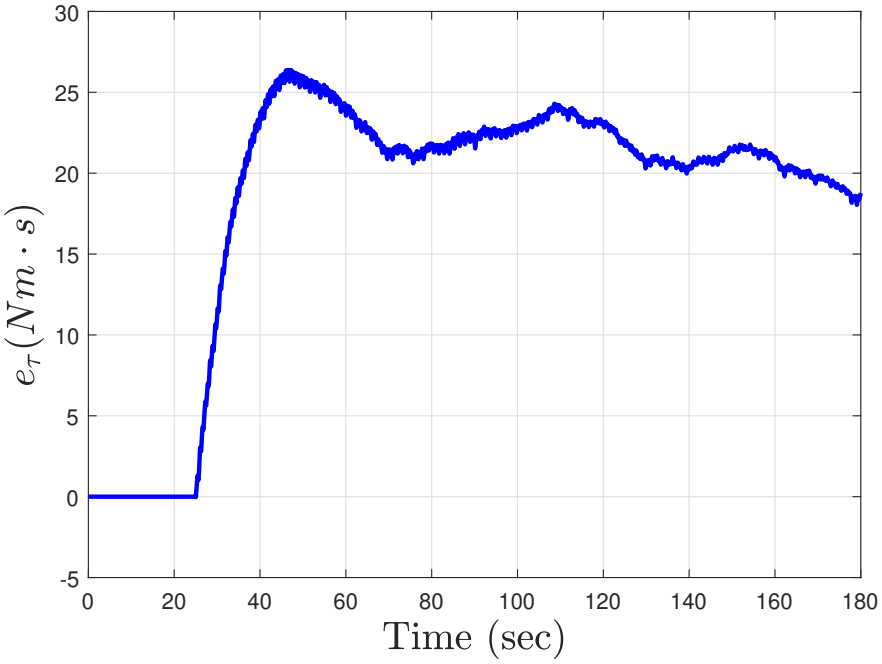

Figure 5.2: The integral-like torque tracking error e_τ in (5.16) is depicted for Subject 4 (S4) during the cycling trial with gain parameters in (5.14) selected as $\beta = 0.3$ and $\lambda = 0.1$. The tracking error starts to be computed and integrated at $t = 25$.

The developed torque tracking controller achieves an average torque tracking error of 32.82 ± 19.50 Nms across all participants. As depicted in Figure 5.2, the integral-like torque tracking signal e_τ started to integrate the error at $t = T_2 = 25$, when the torque tracking controller is activated. The torque tracking error started to build up at the beginning (e.g., up to approximately 45 seconds) since the finite-time controller was adjusting the desired torque to capture the rider's ability to generate active torque (i.e., the finite-time controller leverages estimates of the active muscle torque $\hat{\tau}_m$). The integral torque tracking error decreased for periods during the cycling trial (e.g., around 45-70 seconds) and overall remain bounded. The estimation of the active torque and the desired torque trajectory are shown in Figure 5.3. The rider showed signs of muscle fatigue throughout the experiment, evidenced by decay in the active torque generated,

which may have resulted in increased torque tracking error (e.g., during 80-100 seconds in Figure 5.2. However, the developed finite-time controller kept adjusting the desired torque trajectory based on the rider's torque input data to cope with muscle fatigue. The ability to adapt the desired torque trajectory is an important contribution in the present cycling study because the implementation of predetermined desired torque trajectories as in ([40]) would likely yield increased tracking errors and induce overstimulation of already fatiguing muscles. Figure 5.5 shows the FES inputs applied to the muscles ensuring consistent torque output while preventing high stimulation values that are typical for power tracking experiments implementing predefined torque trajectories ([40]). Thus, cycling trials with predetermined trajectories will require manual adjustments of the torque demand to cope with the muscle fatigue. In addition, incorporating the ability to adapt the desired torque trajectory in real-time holds the potential to extend the duration of the cycling trial.

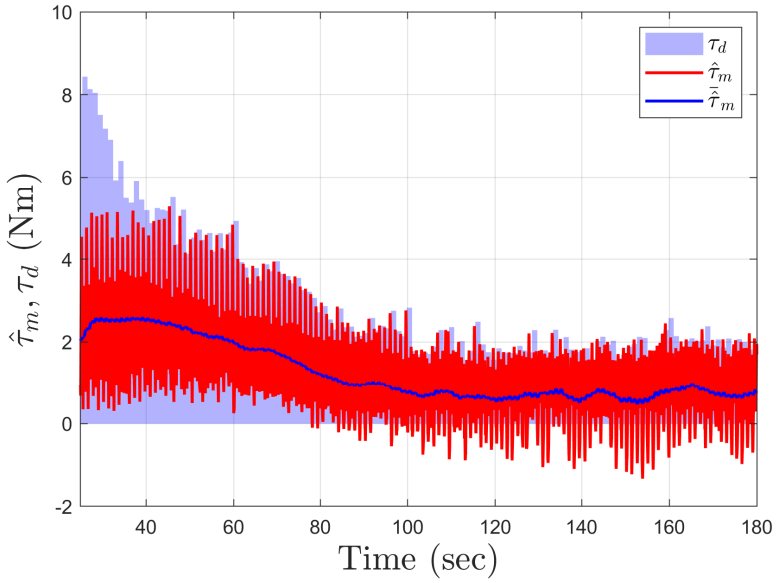

Figure 5.3: Torque tracking performance for Subject 4 (S4) during the cycling trial with gain parameters in (5.14) selected as $\beta = 0.1$ and $\lambda = 0.1$. The light blue curve illustrates the desired torque τ_d and the red curve shows the estimated active torque $\hat{\tau}_m$. The mean of the estimated active torque $\bar{\hat{\tau}}_m$ is computed using a 5 seconds moving window and depicted in solid blue. The mean of the estimated active torque illustrates the time-varying trend of the torque produced by muscles and captures the influence of muscle fatigue.

Stability is guaranteed by the developed stability analyses and illustrated during the cycling trials despite muscle input switching and the nonlinear cycle-rider dynamics. A challenge for the implementation of FES-cycling experiments is related to the muscle activation dynamics. The active torque generated by FES-induced muscle contractions is influenced by the inherent muscle electromechanical delay (EMD). The time-varying EMD is approximately 100–300 ms [86] and degrades the muscle torque tracking performance. A recent study has developed an input delay compensator to inject a delay-free input in the closed-loop error system to compensate for the muscle input delay [37]. However, constructive delayed control compensation requires additional control design and stability analysis, which is beyond the scope of this dissertation. In this chapter, the motivation was to adjust the desired torque trajectory using the finite-time controller leveraging estimates of muscle active torque (thus capturing the muscle activation dynamics) to improve the cycling tracking performance.

The finite-time control technique enables the tuning of the desired torque trajectory (i.e., the torque peak amplitude) by selecting the gain parameters β, λ in (5.14) to tune the controller's rate of convergence and the range of the update law in (5.13). Figure 5.4 presents the performance of the finite-time controller during the four cycling trials for participant S4. The rate of convergence in experiments can be tuned by tuning the control gains in (5.14) as proven in the stability analysis in Theorem 5.2.2. In Figure 5.4, the number of crank cycles needed to reduce the initial peak error and drive error e_f to reach a steady error are around 30, 40, and 55 for $\beta = 0.1, 0.3, 0.5$, respectively with a fixed $\lambda = 0.1$ (as depicted in the top left, bottom left, and top right figures, respectively). For a fixed value of $\beta = 0.3$, it takes around 30 crank cycles to reach a steady error with $\lambda = 0.3$ (bottom right figure) and around 40 crank cycles to reach a steady error with $\lambda = 0.1$ (bottom left figure). The experimental results demonstrate that the developed finite-time controller has the ability to adjust the rate of convergence of desired torque trajectory, which validates the result in the stability analysis during real-time cycling experiments.

The obtained cycling performance in four able-able-bodied individuals shows the feasibility of

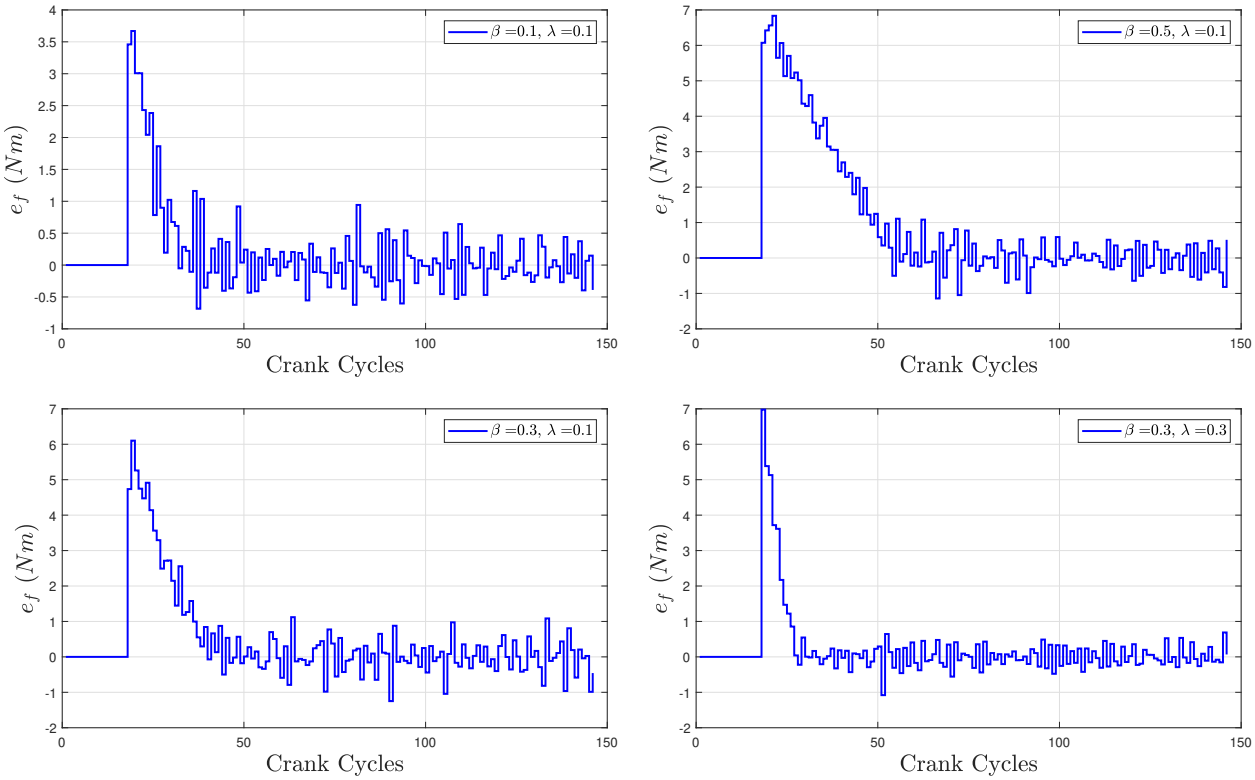

Figure 5.4: The desired torque estimation error e_f, i.e., the discrete finite-time tracking error, is depicted for Subject 4 (S4) using four different gain parameter combinations in (5.14) corresponding to the four cycling trials. Top left, bottom left, and top right figures implement $\lambda = 0.1$ with $\beta = 0.1, 0.3, 0.5$, respectively, depicting the differences in decay rate after the initial peak. Bottom left and bottom right figures also provide a basis for comparison between for $\lambda = 0.1$ and $\lambda = 0.3$ for $\beta = 0.3$ for illustrating the differences in decay rate following the initial peak.

the developed cadence and torque tracking controllers to account for the differences in leg function (e.g., muscle strength, muscle mass, etc.) and achieve satisfactory pedaling rates. The control strategy holds the potential to improve rehabilitative cycling in individuals with different levels of lower-limb function and mobility since each individual will inherently need a different level of assistance. In particular, the controller exploits estimates of the active muscle torque to capture the rider's time-varying ability for power tracking. This control feature is beneficial for FES-cycling and rehabilitation applications to customize the desired trajectories in real-time. Future work includes the implementation of the developed cycling strategy in individuals with movement disorders such as people with chronic SCI who could benefit from the lower-limb exercise. Since the control method is able to adapt the torque demand in real-time, it is envisioned

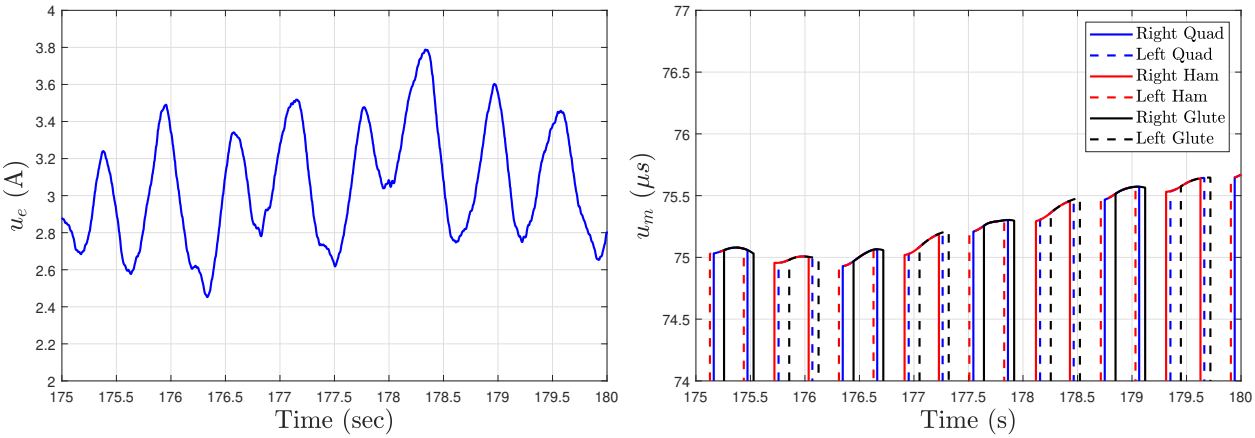

Figure 5.5: Electric motor and muscle stimulation inputs for Subject 1 (S1) during a 5-second window in the cycling trial with gain parameters in (5.14) selected as $\beta = 0.5$ and $\lambda = 0.1$. The left figure shows the motor current computed by u_e. The right figure depicts the pulse widths generated by u_m and applied to the quadriceps, hamstrings, and gluteus muscle groups for the left and right legs.

that long-duration cycling trials could be implemented without the need to manually adjust the torque demand and prevent early termination of the cycling experiment.

The statistical analysis indicates that the tuning of finite-time control parameters in (5.14) yields a statistically significant difference in torque tracking, but not in cadence tracking. This is an expected result since the electric motor is controlled to independently regulate the cadence performance with fixed control gains in (5.7) across cycling trials for all participants. Alternatively, the finite-time controller exploits the rider's torque data and generates the desired active torque trajectory. Thus, changing the control parameters β, λ in (5.14) across the cycling trials yields significant differences in the torque tracking performance quantified by the mean torque tracking error $\overline{e_\tau}$. This implies that the developed finite-time approach is able to customize the desired active torque for the participants in real-time. The sliding-mode control term in (5.7) compensates for the muscle torque input τ_m that appears in the closed-loop cadence error dynamics in (5.8) (i.e., mitigates the influence of torque tracking in the cadence loop). Therefore, the tuning of finite-time control gains that directly influence the closed-loop torque error dynamics does not yield a statistically significant difference in cadence tracking performance. Future work involves

determining how to optimize the selection of the torque control parameters based on a target cycling duration or comfort.

5.5 Concluding Remarks

Motorized FES-cycling combines the benefits of FES and the assistance provided by an electrical motor to achieve consistent, stable lower-limb motion. This chapter developed and implemented power tracking controllers and demonstrated their feasibility in cycling experiments. A cadence controller is designed for the motor to track a desired constant cadence. FES is applied to the lower-limb muscle groups using an integral-like torque tracking error signal. A discrete finite-time algorithm is developed to generate the desired torque trajectory based on input-output data leveraging estimates of the rider's active muscle torque. Thus, the finite-time control method capture the rider's ability to produce active torque in real time cycling experiments. Lyapunov-based stability analyses are presented to guarantee an exponential cadence tracking and a global uniform ultimate bounded (GUUB) torque tracking results. A discrete-time Lyapunov-based stability analysis is used to ensure the finite-time algorithm that generates the desired torque trajectory is Hölder continuous and convergence is obtained in a finite number of crank cycles. Experimental results in seven able-bodied individuals are obtained during four cycling trials. Each cycling trial implemented a different combination of the gain parameters of the finite-time torque algorithm. As shown in the stability analysis, tuning the gain parameters in the finite-time algorithm resulted in changes in the rate of convergence quantified in the number of crank cycles.

Table 5.1: Tracking results for each participant[1]: RMS cadence tracking error, average of cadence tracking error $\bar{\dot{e}}$, and average of torque tracking error $\overline{e_\tau}$.

β	λ	Subject	RMS Cadence Error (rpm)	$\bar{\dot{e}}$ (rpm)	$\overline{e_\tau}$ (Nms)
0.1	0.1	S1	0.88±0.53	0.00±0.88	12.01±5.38
		S2	2.15±1.22	-0.16±2.14	12.23±11.79
		S3	1.76±0.99	-0.07±1.75	22.28±12.79
		S4	1.93±1.02	0.10±1.93	12.18±7.80
		S5	1.31±1.00	0.03±1.65	7.98±3.81
		S6	1.58±0.78	-0.03±1.58	33.33±20.63
		S7	2.05±1.22	-0.11±2.05	43.54±26.87
0.3	0.1	S1	1.21±0.67	-0.13±1.20	39.26±20.30
		S2	1.26±0.76	-0.14±1.26	24.40±11.29
		S3	1.62±0.93	-0.09±1.62	30.06±14.90
		S4	1.93±1.10	0.00±1.93	18.23±8.22
		S5	1.72±1.01	0.12±1.71	33.09±21.07
		S6	1.91±1.14	-0.07±1.91	68.47±46.68
		S7	2.40±1.30	0.08±2.40	106.33±70.57
0.3	0.3	S1	0.88±0.51	-0.02±0.88	12.38±5.85
		S2	1.21±0.74	-0.17±1.19	33.69±25.25
		S3	1.54±0.88	-0.01±1.54	11.28±6.97
		S4	1.80±0.97	-0.03±1.80	18.72±8.99
		S5	1.39±0.90	0.06±1.39	9.34±6.26
		S6	0.95±0.53	0.03±0.95	14.53±11.18
		S7	1.17±0.73	-0.07±1.16	31.05±21.01
0.5	0.1	S1	0.87±0.51	-0.05±0.87	46.81±25.41
		S2	1.63±1.00	-0.24±1.61	66.39±36.29
		S3	1.23±0.67	0.03±1.23	38.69±18.96
		S4	2.06±1.18	-0.09±2.06	39.09±18.54
		S5	1.74±0.94	0.07±1.74	25.92±14.51
		S6	2.13±1.25	0.01±2.13	75.79±49.15
		S7	1.57±1.05	-0.02±1.57	31.79±15.53
Mean(S1-S7)			1.48	-0.03	32.82
STD[2](S1-S7)			0.91	1.58	19.50

[1] Reported as mean ± standard deviation (STD).

[2] Reports the mean over the standard deviations.

Chapter 6

Conclusions

6.1 Contributions and conclusions

This dissertation focuses on developing controllers that leverage kinematic and force/torque feedback for powered lower-limb machines modeled as nonlinear, time-varying, and uncertain switched systems with disturbances. To achieve the desired tracking performance, closed-loop controllers are developed to comply with the human dynamics while coping with the inherent uncertainties in the human-robot parameters and rejecting disturbances that degrade performance. The dissertation focuses on the design of switching nonlinear controllers and their stability through Lyapunov-based methods. The design, analysis and implementation of controllers that activate muscles and motors for assisted cycling and walking have implications for advancing lower-limb rehabilitation and gait training. Ultimately, the benefits of hybrid exoskeletons and motorized cycles have to be examined in clinical studies with people with NCs.

In Chapter 3, a hierarchical strategy was developed to segregate the control design into high- and low-level layers for cable-driven exoskeletons. Cable-driven exoskeletons are powerful tools to provide assistance during walking due to their light-weight components. However, coordinating

the control between the pair of electric motors that actuate each joint requires stable switching to achieve suitable leg flexion and extension. In addition, a constructive and systematic control design is needed to mitigate cable slackness and prevent antagonistic activation of the cable-pulley system that actuate the powered exoskeleton. The design and analysis of nonlinear robust switching controllers were developed for the knee joint, leveraging switched systems theory and a Lyapunov-based stability analysis. The developed controllers ensure exponential tracking for both the kinematic joint tracking error (high-level) and motor tracking (low-level) objectives. The experimental result for controlling the knee joint to ensure leg flexion and extension demonstrates the feasibility of the developed controllers. The hierarchical structure is extended to actuate knee and hip joints bilaterally during treadmill walking in Chapter 4.

In Chapter 4, the dual control objective of kinematic and stiffness tracking are accomplished by designing controllers for the knee and hip joints. The stiffness controller is motivated for human-robot interaction applications for its ability to absorb shock, robustness to perturbations, and safety. Chapter 4 developed a novel control design to adjust the knee joint stiffness and guide the joint kinematics through the collaboration of muscles and motors in the powered exoskeleton. The analysis of the closed-loop kinematic and stiffness error systems provide stability guarantees and boundedness of all the input signals. Subsequent work will focus on how to generate and adapt the desired stiffness parameters in real-time to improve the leg interaction during walking. The kinematic and stiffness controllers ensure exponential tracking despite the switching effects and additive disturbances included in the model. The developed controllers were implemented in three able-individuals during walking trials on a treadmill at two constant speeds. It is notable in the experimental results that EMD is an important factor that negatively influences walking performance using the hybrid exoskeleton as has been also reported in [16], [37]. Control design innovations are necessary to compensate for the muscle input delay in the context of switched systems during assisted walking with hybrid exoskeleton. Developing input-delay compensators impose additional challenges in the design and analysis since the EMD is time-varying and unknown for each muscle [86]. Moreover, the development of novel control methods that comply

and promote human voluntary effort are desired during gait rehabilitation to achieve a more natural gait pattern in individuals with neurological conditions. Advances in control methods and wearable devices are needed to advance the utility of hybrid exoskeleton to improve the participant's gait speed and endurance toward achieving community ambulation after an injury.

In Chapter 5, a power tracking objective was implemented for motorized FES-cycling in which the muscles evoke active torque to track the desired torque trajectory and the motor keeps the rider at a constant speed. A novel feature in the developed control methods is the inclusion of a finite-time stable torque algorithm to adapt the desired peak torque demand for the muscles. The motivation is for the finite-time controller to capture the rider's muscle ability to produce active torque in real-time using collected rider's torque data due to the applied FES input. The finite-time torque algorithm leverages estimates of the active torque using the feedback provided by the powermeter in the cycle. A future research direction is to combine finite-time and adaptive control techniques to adjust the rate of convergence of adaptive estimates of parametric uncertainty in the cycle-rider system, which can lead to improved tracking performance. Another way to capture the muscle dynamics in real-time is using an ultrasound imaging approach [92]. This approach enables the estimation of the muscle dynamics and can provide surrogate signals to explicitly quantify muscle fatigue, which can be exploited as a feedforward control term or to modify the electric motor assistance (e.g., to compensate for the time-varying muscle fatigue). The approach in Chapter 5 is motivated by the need to adapt the tracking controllers leveraging non-invasive estimates of the human contribution during cycling. Chapter 5 leverages the lumped active torque produced by the stimulated muscle groups in real-time, which exploits the state-dependent stimulation pattern used in [9]. Exponential cadence tracking, globally uniform ultimate bounded (GUUB) torque tracking, and Hölder continuous and convergence properties of the finite-time controller are obtained. Experiments with different control gains in the finite-time algorithm have been implemented to demonstrate the impact on convergence. The cycling tracking performance and convergence of the finite-time algorithm were examined in multiple trials in seven able-bodied individuals.

6.2 Research directions

The experiments conducted in this dissertation involved able-bodied individuals to test the control techniques and demonstrate their feasibility before recruiting people with movement disorders. Validation of the developed control methods in individuals with movement deficits will be conducted as part of future work. The reduced muscle mass and strength due to atrophy in people with NCs will likely present additional control challenges such as requiring increased robotic and FES assistance and experiencing faster rates of muscle fatigue that can lead to shorter experiment duration (e.g., low repetition or dosage), thus reducing the rehabilitation benefits. Moreover, participants with SCI are likely going to require increased trunk support for treadmill walking and the use of a walker for overground gait training. Furthermore, hypersensitivity to FES (i.e., degraded sensory feedback) may result in limited neuromuscular benefits. A potential direction is to develop a procedure to personalize the control gains to balance the need to yield suitable tracking performance and the sensory challenges that may limit the FES control authority in people with NCs. Thus, the design of novel adaptive control techniques is motivated to identify critical parameters of the dynamic system and improve how the control is shared to enhance the user assistance as muscle fatigues.

The robust controllers developed in this dissertation leveraged a sliding-mode control technique to compensate for the uncertainty in the human-robot models and disturbances to guarantee exponential tracking results, which are needed to obtain necessary rates of convergence for the switched systems [57]. A drawback of sliding-mode control is the potential chattering effects that may degrade tracking performance during experiments. High frequency control inputs can accelerate muscle fatigue. Future research directions include the design of adaptive-based learning controllers that seek to estimate uncertain parameters in the model to minimize the need to compensate for uncertainties via sliding modes. Examples of such adaptive methods include repetitive learning [10], concurrent learning [61], model free control [74], and neural networks. These learning controllers add a feedforward inputs into the controller to rely less on high frequency

feedback and still guarantee stability. However, adaptive switched controllers pose additional challenges to guarantee exponential convergence since traditional adaptive methods only yield asymptotic tracking results [88].

The dynamic model for the powered lower-limb exoskeleton with FES have limitations and exploit assumptions as described in Chapter 2. Future work seeks to develop gait models that capture foot impact effects (i.e., impact forces when the heel strikes the ground) to yield a hybrid gait system model [93]. An open challenge is to integrate the hybrid gait model with the switching effects ubiquitous to control concurrently the exoskeleton and FES. New control formulations are required to design human-robot controllers and analyze the stability of the hybrid gait system. In this dissertation, the double support phase is assumed to be instantaneous during treadmill walking; however, the double support phase accounts for approximately 20% of the gait cycle [93] during overground. The double support phase yields the 4-link lower-limb model a closed kinematic chain, which corresponds to an over-actuated system motivating optimal-based control techniques [94]. Further modeling refinements for the present work include advancing the foot segment model (beyond the single point ground contact used in this dissertation) and considering the ground contact interaction (e.g., slip conditions and foot rotation). The desired kinematic trajectories in this dissertation were recorded during walking trials in able-bodied individuals, which may not be suitable for people with NCs. Optimization methods to generate kinematic trajectories suitable for the human interfacing the powered exoskeleton and FES will be explored [95]. Phase-based controllers that exploit gait detection algorithms are also motivated to generate state-based trajectories rather than time-fixed gait patterns. The design, analysis and implementation of the developed controllers in this dissertation for assisted walking and cycling are developed to provide contributions and motivate new future research directions at the intersection of rehabilitation engineering, control systems and robotics toward enhancing the quality of life of people with NCs.

References

[1] T. G. Hornby, D. S. Reisman, I. G. Ward, *et al.*, "Clinical Practice Guideline to Improve Locomotor Function Following Chronic Stroke, Incomplete Spinal Cord Injury, and Brain Injury," *J. Neurol. Phys. Ther.*, vol. 44, no. 1, pp. 49–100, 2020.

[2] B. M. Doucet, A. Lam, and L. Griffin, "Neuromuscular Electrical Stimulation for Skeletal Muscle Function," *Yale J. Biol. Med.*, vol. 85, no. 2, pp. 201–215, 2012.

[3] J. McCabe, M. Monkiewicz, J. Holcomb, *et al.*, "Comparison of robotics, functional electrical stimulation, and motor learning methods for treatment of persistent upper extremity dysfunction after stroke: A randomized controlled trial," *Arch. Phys. Med. Rehabil.*, vol. 96, no. 6, pp. 981–990, 2015.

[4] C. A. Rouse, A. Parikh, V. Duenas, *et al.*, "A switched systems approach based on changing muscle geometry of the biceps brachii during functional electrical stimulation," *IEEE Control Syst. Lett.*, vol. 2, no. 1, pp. 73–78, 2018.

[5] N. Alibeji, N. Kirsch, and N. Sharma, "An adaptive low-dimensional control to compensate for actuator redundancy and FES-induced muscle fatigue in a hybrid neuroprosthesis," *Control Eng. Pract.*, vol. 59, pp. 204–219, 2017.

[6] N. A. Kirsch, X. Bao, N. A. Alibeji, *et al.*, "Model-Based Dynamic Control Allocation in a Hybrid Neuroprosthesis," *IEEE Trans. Neural Syst. Rehabil. Eng.*, vol. 26, no. 1, pp. 224–232, 2018.

[7] R. Kobetic, C. S. To, J. R. Schnellenberger, *et al.*, "Development of hybrid orthosis for standing, walking, and stair climbing after spinal cord injury," *J. Rehabil. Res. \& Dev.*, vol. 46, no. 3, 2009.

[8] R. Nataraj, M. L. Audu, and R. J. Triolo, "Restoring standing capabilities with feedback control of functional neuromuscular stimulation following spinal cord injury," *Med. Eng. Phys.*, vol. 42, pp. 13–25, 2017.

[9] M. J. Bellman, R. J. Downey, A. Parikh, *et al.*, "Automatic Control of Cycling Induced by Functional Electrical Stimulation With Electric Motor Assistance," *IEEE Trans. Autom. Sci. Eng.*, vol. 14, no. 2, pp. 1225–1234, 2017.

[10] V. H. Duenas, C. A. Cousin, A. Parikh, *et al.*, "Motorized and Functional Electrical Stimulation Induced Cycling via Switched Repetitive Learning Control," *IEEE Trans. Control Syst. Technol.*, vol. 27, no. 4, pp. 1468–1479, 2019.

[11] V. H. Duenas, C. A. Cousin, V. Ghanbari, *et al.*, "Passivity based learning control for torque and cadence tracking in functional electrical stimulation (FES) induced cycling," *2018 Annu. Am. Control Conf.*, pp. 3726–3731, 2018.

[12] C. A. Cousin, V. H. Duenas, C. A. Rouse, *et al.*, "Motorized functional electrical stimulation for torque and cadence tracking: A switched Lyapunov approach," *2017 IEEE 56th Annu. Conf. Decis. Control*, pp. 5900–5905, 2017.

[13] V. Ghanbari, V. H. Duenas, P. J. Antsaklis, *et al.*, "Passivity-Based Iterative Learning Control for Cycling Induced by Functional Electrical Stimulation With Electric Motor Assistance," *IEEE Trans. Control Syst. Technol.*, vol. 27, no. 5, pp. 2287–2294, 2019.

[14] C. L. Lynch and M. R. Popovic, "Functional Electrical Stimulation," *IEEE Control Syst. Mag.*, vol. 28, pp. 40–50, 2008.

[15] K. H. Ha, S. A. Murray, and M. Goldfarb, "An Approach for the Cooperative Control of FES with a Powered Exoskeleton during Level Walking for Persons with Paraplegia," *IEEE Trans. Neural Syst. Rehabil. Eng.*, vol. 24, no. 4, pp. 455–466, 2016.

[16] N. A. Alibeji, V. Molazadeh, B. E. Dicianno, *et al.*, "A control scheme that uses dynamic postural synergies to coordinate a hybrid walking neuroprosthesis: Theory and experiments," *Front. Neurosci.*, vol. 12, p. 159, 2018.

[17] S. R. Chang, M. J. Nandor, L. Li, *et al.*, "A muscle-driven approach to restore stepping with an exoskeleton for individuals with paraplegia," *J. Neuroeng. Rehabil.*, vol. 14, no. 1, pp. 1–12, 2017.

[18] M. Nandor, R. Kobetic, M. Audu, *et al.*, "A Muscle-First, Electromechanical Hybrid Gait Restoration System in People With Spinal Cord Injury," *Front. Robot. AI*, vol. 8, no. April, pp. 1–11, 2021.

[19] N. A. Alibeji, N. A. Kirsch, and N. Sharma, "A Muscle Synergy-Inspired Adaptive Control Scheme for a Hybrid Walking Neuroprosthesis," *Front. Bioeng. Biotechnol.*, vol. 3, no. December, pp. 1–13, 2015.

[20] S. R. Chang, R. Kobetic, and R. J. Triolo, *Hybrid exoskeletons to restore gait in individuals with paralysis from spinal cord injury*. INC, 2020, pp. 335–346.

[21] K. A. Witte, J. Zhang, R. W. Jackson, *et al.*, "Design of two lightweight, high-bandwidth torque-controlled ankle exoskeletons," *Proc. - IEEE Int. Conf. Robot. Autom.*, pp. 1223–1228, 2015.

[22] K. A. Witte, A. M. Fatschel, and S. H. Collins, "Design of a lightweight, tethered, torque-controlled knee exoskeleton," *IEEE Int. Conf. Rehabil. Robot.*, pp. 1646–1653, 2017.

[23] S. H. Collins, M. Bruce Wiggin, and G. S. Sawicki, "Reducing the energy cost of human walking using an unpowered exoskeleton," *Nature*, vol. 522, no. 7555, pp. 212–215, 2015.

[24] A. T. Asbeck, S. M. M. D. Rossi, I. Galiana, *et al.*, "Stronger, Smarter, Softer: Next-Generation Wearable Robots," *IEEE Robot. \& Autom. Mag.*, vol. 21, pp. 22–33, 2014.

[25] E. J. Park, T. Akbas, A. Eckert-Erdheim, *et al.*, "A Hinge-Free, Non-Restrictive, Lightweight Tethered Exosuit for Knee Extension Assistance during Walking," *IEEE Trans. Med. Robot. Bionics*, vol. 2, no. 2, pp. 165–175, 2020.

[26] A. Di Lallo, S. Yu, T.-H. Huang, *et al.*, "High-performance soft wearable robots for human augmentation and gait rehabilitation," *Soft Robot. Rehabil.*, pp. 1–38, 2021.

[27] G. M. Bryan, P. W. Franks, S. C. Klein, *et al.*, "A hip–knee–ankle exoskeleton emulator for studying gait assistance," *Int. J. Rob. Res.*, 2020.

[28] A. T. Asbeck, K. Schmidt, I. Galiana, *et al.*, "Multi-joint soft exosuit for gait assistance," *Proc. - IEEE Int. Conf. Robot. Autom.*, vol. 2015-June, no. June, pp. 6197–6204, 2015.

[29] T. Noda, T. Teramae, B. Ugurlu, *et al.*, "Development of an upper limb exoskeleton powered via pneumatic electric hybrid actuators with bowden cable," *IEEE Int. Conf. Intell. Robot. Syst.*, pp. 3573–3578, 2014.

[30] T. Lenzi, N. Vitiello, S. M. M. De Rossi, *et al.*, "NEUROExos: A variable impedance powered elbow exoskeleton," *Proc. - IEEE Int. Conf. Robot. Autom.*, pp. 1419–1426, 2011.

[31] J. M. Caputo and S. H. Collins, "A universal ankle-foot prosthesis emulator for human locomotion experiments," *J. Biomech. Eng.*, vol. 136, no. 3, pp. 1–10, 2014.

[32] S. R. Chang, R. Kobetic, and R. J. Triolo, "Effect of exoskeletal joint constraint and passive resistance on metabolic energy expenditure: Implications for walking in paraplegia," *PLoS One*, vol. 12, no. 8, pp. 1–12, 2017.

[33] J. Zhang, P. Fiers, K. A. Witte, *et al.*, "Human-in-the-loop optimization of exoskeleton assistance during walking," *Science (80-.).*, vol. 356, no. 6344, pp. 1280–1284, 2017.

[34] Y. Ding, M. Kim, S. Kuindersma, *et al.*, "Human-in-the-loop optimization of hip assistance with a soft exosuit during walking," *Sci. Robot.*, vol. 3, no. 15, pp. 1–9, 2018.

[35] K. A. Witte, P. Fiers, A. L. Sheets-Singer, *et al.*, "Improving the energy economy of human running with powered and unpowered ankle exoskeleton assistance," *Sci. Robot.*, vol. 5, no. 40, pp. 1–9, 2020.

[36] C. Siviy, J. Bae, L. Baker, *et al.*, "Offline Assistance Optimization of a Soft Exosuit for Augmenting Ankle Power of Stroke Survivors during Walking," *IEEE Robot. Autom. Lett.*, vol. 5, no. 2, pp. 828–835, 2020.

[37] N. A. Alibeji, V. Molazadeh, F. Moore-Clingenpeel, *et al.*, "A muscle synergy-inspired control design to coordinate functional electrical stimulation and a powered exoskeleton: Artificial generation of synergies to reduce input dimensionality," *IEEE Control Syst. Mag.*, vol. 38, no. 6, pp. 35–60, 2018.

[38] C. Cousin, V. Duenas, and W. Dixon, "Fes cycling and closed-loop feedback control for rehabilitative human–robot interaction," *Robotics*, vol. 10, no. 2, pp. 1–23, 2021.

[39] C. H. Chang and V. H. Duenas, "Switched Motorized and Functional Electrical Stimulation Cycling Controllers for Power Tracking," *2019 IEEE 58th Conf. Decis. Control*, pp. 1436–1441, 2019.

[40] V. H. Duenas, C. A. Cousin, V. Ghanbari, *et al.*, "Torque and cadence tracking in functional electrical stimulation induced cycling using passivity-based spatial repetitive learning control," *Automatica*, vol. 115, p. 108 852, 2020.

[41] C. A. Cousin, V. H. Duenas, C. A. Rouse, *et al.*, "Closed-Loop Cadence and Instantaneous Power Control on a Motorized Functional Electrical Stimulation Cycle," *IEEE Trans. Control Syst. Technol.*, vol. 28, no. 6, pp. 2276–2291, 2020.

[42] J. Duysens, F. Clarac, and H. Cruse, "Load-regulating mechanisms in gait and posture: Comparative aspects," *Physiol. Rev.*, vol. 80, no. 1, pp. 83–133, 2000.

[43] T. R. Nichols, "The contributions of muscles and reflexes to the regulation of joint and limb mechanics," *Clin. Orthop. Relat. Res.*, vol. 403, pp. 43–50, 2002.

[44] A. Q. Keemink, H. van der Kooij, and A. H. Stienen, "Admittance control for physical human–robot interaction," *Int. J. Rob. Res.*, vol. 37, no. 11, pp. 1421–1444, 2018.

[45] B. Vanderborght, A. Albu-Schaeffer, A. Bicchi, *et al.*, "Variable impedance actuators: A review," *Rob. Auton. Syst.*, vol. 61, no. 12, pp. 1601–1614, 2013.

[46] G. Grioli, S. Wolf, M. Garabini, *et al.*, "Variable stiffness actuators: The user's point of view," *Int. J. Rob. Res.*, vol. 34, no. 6, pp. 727–743, 2015.

[47] V. R. Garate, M. Pozzi, D. Prattichizzo, *et al.*, "Grasp Stiffness Control in Robotic Hands Through Coordinated Optimization of Pose and Joint Stiffness," *IEEE Robot. Autom. Lett.*, vol. 3, no. 4, pp. 3952–3959, 2018.

[48] Z. Li, B. Huang, Z. Ye, *et al.*, "Physical human-robot interaction of a robotic exoskeleton by admittance control," *IEEE Trans. Ind. Electron.*, vol. 65, no. 12, pp. 9614–9624, 2018.

[49] M. Moltedo, G. Cavallo, T. Baček, *et al.*, "Variable stiffness ankle actuator for use in robotic-assisted walking: Control strategy and experimental characterization," *Mech. Mach. Theory*, vol. 134, pp. 604–624, 2019.

[50] M. Mahvash and P. E. Dupont, "Stiffness control of surgical continuum manipulators," *IEEE Trans. Robot.*, vol. 27, no. 2, pp. 334–345, 2011.

[51] J. Meuleman, E. Van Asseldonk, G. Van Oort, *et al.*, "LOPES II - Design and Evaluation of an Admittance Controlled Gait Training Robot with Shadow-Leg Approach," *IEEE Trans. Neural Syst. Rehabil. Eng.*, vol. 24, no. 3, pp. 352–363, 2016.

[52] A. J. Del-Ama, Á. Gil-Agudo, J. L. Pons, *et al.*, "Hybrid FES-robot cooperative control of ambulatory gait rehabilitation exoskeleton," *J. Neuroeng. Rehabil.*, vol. 11, no. 1, pp. 1–15, 2014.

[53] J. Zhang and S. H. Collins, "The Iterative Learning Gain That Optimizes Real-Time Torque Tracking for Ankle Exoskeletons in Human Walking Under Gait Variations," *Front. Neurorobot.*, vol. 15, no. May, pp. 1–11, 2021.

[54] Y. Mao and S. K. Agrawal, "A cable driven upper arm exoskeleton for upper extremity rehabilitation," *Proc. - IEEE Int. Conf. Robot. Autom.*, pp. 4163–4168, 2011.

[55] R. Verhoeven, "Analysis of the Workspace of Tendon-Based," *Duisbg. Gerhard Mercat. Univ.*, 2003.

[56] V. Potkonjak, B. Svetozarevic, K. Jovanovic, *et al.*, "The puller-follower control of compliant and noncompliant antagonistic tendon drives in robotic systems," *Int. J. Adv. Robot. Syst.*, vol. 8, no. 5, pp. 143–155, 2011.

[57] D. Liberzon, *Switching in systems and control*. Birkhauser, 2003.

[58] M. J. Bellman, T. H. Cheng, R. J. Downey, *et al.*, "Switched Control of Cadence during Stationary Cycling Induced by Functional Electrical Stimulation," *IEEE Trans. Neural Syst. Rehabil. Eng.*, vol. 24, no. 12, pp. 1373–1383, 2016.

[59] H. Kawai, M. J. Bellman, R. J. Downey, *et al.*, "Closed-Loop Position and Cadence Tracking Control for FES-Cycling Exploiting Pedal Force Direction with Antagonistic Biarticular Muscles," *IEEE Trans. Control Syst. Technol.*, vol. 27, no. 2, pp. 730–742, 2019.

[60] A. Farhoud and A. Erfanian, "Fully automatic control of paraplegic FES pedaling using higher-order sliding mode and fuzzy logic control," *IEEE Trans. Neural Syst. Rehabil. Eng.*, vol. 22, no. 3, pp. 533–542, 2014.

[61] J. Casas, C.-H. Chang, and V. H. Duenas, "Motorized and Functional Electrical Stimulation Induced Cycling via Switched Adaptive Concurrent Learning Control," *Proc. ASME 2020 Dyn. Syst. Control Conf.*, vol. 1, 2020.

[62] C.-H. Chang, J. Casas, S. W. Brose, *et al.*, "Closed-Loop Torque and Kinematic Control of a Hybrid Lower-Limb Exoskeleton for Treadmill Walking," *Front. Robot. AI*, vol. 8, no. January, pp. 1–19, 2022.

[63] C. A. Cousin, V. H. Duenas, C. A. Rouse, *et al.*, "Admittance Control of Motorized Functional Electrical Stimulation Cycle," *IFAC-PapersOnLine*, vol. 51, no. 34, pp. 272–277, 2019.

[64] K. J. Hunt, B. Stone, N. O. Negård, *et al.*, "Control Strategies for Integration of Electric Motor Assist and Functional Electrical Stimulation in Paraplegic Cycling: Utility for Exercise Testing and Mobile Cycling," *IEEE Trans. Neural Syst. Rehabil. Eng.*, vol. 12, no. 1, pp. 89–101, 2004.

[65] S. P. Bhat and D. S. Bernstein, "Finite-time stability of continuous autonomous systems," *SIAM J. Control Optim.*, vol. 38, no. 3, pp. 751–766, 2000.

[66] O. Romero and M. Benosman, "Time-varying continuous-time optimisation with pre-defined finite-time stability," *Int. J. Control*, vol. 94, no. 12, pp. 3237–3254, 2021.

[67] W. M. Haddad, S. G. Nersesov, and L. Du, "Finite-time stability for time-varying nonlinear dynamical systems," *Proc. Am. Control Conf.*, pp. 4135–4139, 2008.

[68] K. Garg and D. Panagou, "Finite-time stability of switched and hybrid systems," *arXiv Prepr. arXiv1901.08513*, 2019. arXiv: 1901.08513.

[69] K. Garg, P. Bobade, and D. Panagou, "Finite-Time Stability of Adaptive Parameter Estimation and Control," *arXiv Prepr. arXiv1811.11151*, 2018. arXiv: 1811.11151.

[70] Q. Hui, W. M. Haddad, and S. P. Bhat, "Semistability, finite-time stability, differential inclusions, and discontinuous dynamical systems having a continuum of equilibria," *IEEE Trans. Automat. Contr.*, vol. 54, no. 10, pp. 2465–2470, 2009.

[71] S. G. Nersesov and W. M. Haddad, "Finite-time stabilization of nonlinear impulsive dynamical systems," *Nonlinear Anal. Hybrid Syst.*, vol. 2, pp. 832–845, 2008.

[72] J. I. Poveda and M. Krstic, "Fixed-Time Extremum Seeking," *2020 Am. Control Conf.*, no. 1, pp. 2838–2843, 2020. arXiv: 1912.06999.

[73] M. Guay and M. Benosman, "Finite-time extremum seeking control for a class of unknown static maps," *Int. J. Adapt. Control Signal Process.*, vol. 35, no. 7, pp. 1188–1201, 2021.

[74] A. K. Sanyal, "Discrete-time data-driven control with Hölder-continuous real-time learning," *Int. J. Control*, 2021.

[75] D. A. Winter, *Biomechanics and motor control of human movement*. Wiley, 2009.

[76] F. L.Lewis, D. M.Dawson, and C. T.Abdallah, *Robot Manipulator Control Theory and Practice*. Marcel Dekker, 2004.

[77] M. Ferrarin and A. Pedotti, "The relationship between electrical stimulus and joint torque: A dynamic model," *IEEE Trans. Rehabil. Eng.*, vol. 8, no. 3, pp. 342–352, 2000.

[78] N. Sharma, K. Stegath, C. M. Gregory, *et al.*, "Nonlinear neuromuscular electrical stimulation tracking control of a human limb," *IEEE Trans. Neural Syst. Rehabil. Eng.*, vol. 17, no. 6, pp. 576–584, 2009.

[79] T. Schauer, N. O. Negård, F. Previdi, *et al.*, "Online identification and nonlinear control of the electrically stimulated quadriceps muscle," *Control Eng. Pract.*, vol. 13, no. 9, pp. 1207–1219, 2005.

[80] M. J. Bellman, T. H. Cheng, R. J. Downey, *et al.*, "Cadence control of stationary cycling induced by switched functional electrical stimulation control," *Proc. IEEE Conf. Decis. Control*, pp. 6260–6265, 2014.

[81] C. Chang, J. Casas, and V. H. Duenas, "A Switched Systems Approach for Closed-loop Control of a Lower-Limb Cable-Driven Exoskeleton," *Proc. Am. Control Conf.*, to appear, 2022.

[82] B. E. Paden and S. S. Sastry, "A Calculus for Computing Filippov's Differential Inclusion with Application to the Variable Structure Control of Robot Manipulators," *IEEE Trans. Circuits Syst.*, vol. 34, no. 1, pp. 73–82, 1987.

[83] N. Fischer, R. Kamalapurkar, and W. E. Dixon, "LaSalle-Yoshizawa corollaries for nonsmooth systems," *IEEE Trans. Automat. Contr.*, vol. 58, no. 9, pp. 2333–2338, 2013.

[84] R. R. Neptune, K. Sasaki, and S. A. Kautz, "The effect of walking speed on muscle function and mechanical energetics," *Gait Posture*, vol. 28, no. 1, pp. 135–143, 2008.

[85] J. Perry, *Gait Analysis-normal And Pathological Function*. Slack, 1992.

[86] R. J. Downey, M. Merad, E. J. Gonzalez, *et al.*, "The Time-Varying Nature of Electromechanical Delay and Muscle Control Effectiveness in Response to Stimulation-Induced Fatigue," *IEEE Trans. Neural Syst. Rehabil. Eng.*, vol. 25, no. 9, pp. 1397–1408, 2017.

[87] R. J. Downey, M. J. Bellman, H. Kawai, *et al.*, "Comparing the Induced Muscle Fatigue Between Asynchronous and Synchronous Electrical Stimulation in Able-Bodied and Spinal Cord Injured Populations," *IEEE Trans. Neural Syst. Rehabil. Eng.*, vol. 23, no. 6, pp. 964–972, 2015.

[88] J. W. Khalil, Hassan K and Grizzle, *Nonlinear systems*. Prentice hall Upper Saddle River, NJ, 2002.

[89] G. Lv, H. Zhu, and R. D. Gregg, "On the design and control of highly backdrivable lower-limb exoskeletons: A discussion of past and ongoing work," *IEEE Control Syst. Mag.*, vol. 38, no. 6, pp. 88–113, 2018.

[90] A. Hereid, C. M. Hubicki, E. A. Cousineau, *et al.*, "Dynamic Humanoid Locomotion: A Scalable Formulation for HZD Gait Optimization," *IEEE Trans. Robot.*, vol. 34, no. 2, pp. 370–387, 2018.

[91] T. Gurriet, S. Finet, G. Boeris, *et al.*, "Towards Restoring Locomotion for Paraplegics: Realizing Dynamically Stable Walking on Exoskeletons," *Proc. - IEEE Int. Conf. Robot. Autom.*, pp. 2804–2811, 2018.

[92] Z. Sheng, N. Sharma, and K. Kim, "Quantitative Assessment of Changes in Muscle Contractility Due to Fatigue during NMES: An Ultrasound Imaging Approach," *IEEE Trans. Biomed. Eng.*, vol. 67, no. 3, pp. 832–841, 2020.

[93] J. W. Grizzle, C. Chevallereau, R. W. Sinnet, *et al.*, "Models, feedback control, and open problems of 3D bipedal robotic walking," *Automatica*, vol. 50, no. 8, pp. 1955–1988, 2014.

[94] F. Farzadpour, M. Danesh, and S. M. Torklarki, "Development of multi-phase dynamic equations for a seven-link biped robot with improved foot rotation in the double support phase," *Proc. Inst. Mech. Eng. Part C J. Mech. Eng. Sci.*, vol. 229, no. 1, pp. 3–17, 2015.

[95] O. Harib, A. Hereid, A. Agrawal, *et al.*, "Feedback control of an exoskeleton for paraplegics: Toward robustly stable, hands-free dynamic walking," *IEEE Control Syst. Mag.*, vol. 38, no. 6, pp. 61–87, 2018.

Chapter 7

Vita

Chen-Hao Chang received the bachelor's degree in Aeronautics and Astronautics Engineering from National Cheng Kung University in 2014, and received his master degree in Aerospace Engineering from University of Florida in 2018. He joined the Bionics Systems Control Lab (BSC) research group at Syracuse University to pursue his doctoral degree under the supervision of Dr. Victor H. Duenas in 2018. His research interests include force and kinematic nonlinear control for rehabilitation robotics, neuromuscular control, and switched systems.